(18) AFOSR-TR-81-0612

JUL 20 1981

AD A102446 LEVEL II

BS

Systems, Science and Software

(14) SSS-R-81-5081
W/O 11127
work order

(6) SIMULATION OF SHORT PERIOD Lg, EXPANSION OF THREE-DIMENSIONAL SOURCE SIMULATION CAPABILITIES AND SIMULATION OF NEAR-FIELD GROUND MOTION FROM THE 1971 SAN FERNANDO, CALIFORNIA, EARTHQUAKE.

(10) T. C. Bache
H. J. Swanger
B. Shkoller
S. M. Day

DTIC ELECTE AUG 4 1981 S C

(9) FINAL REPORT.
1 Oct 74 - 30 Nov 80.

Sponsored by

ADVANCED RESEARCH PROJECTS AGENCY

(15) F49620-80-C-0019, (16) 2309
ARPA Order [redacted]-3291-32

(17) A1

(11) Jul[redacted]81 (12) 153

[redacted]

DTIC FILE COPY

P. O. Box 1620
La Jolla, California
92038
(714) 453-0060

Approved for public release;
distribution unlimited.

388507

81 8 04 018

ARPA Order No. 3291-32, Program Code No. 0D60

Contractor: Systems, Science and Software

Effective Date of Contract: 1 October 1979

Contract Expiration Date: 30 September 1980

Amount of Contract: $88,024

Contract No: F49620-80-C-0019

Principal Investigator and Phone No:

Dr. Thomas C. Bache, (714) 453-0060, Ext. 337

Program Manager and Phone No:

Dr. Thomas C. Bache, (714) 453-0060, Ext. 337

Title: Theoretical Basis for Regional Discrimination

This research was supported by the Advanced Research Projects Agency of the Department of Defense and was monitored by the Air Force Office of Scientific Research under Contract No. F49620-80-C-0019.

The views and conclusions contained in this document are those of the authors and should not be interpreted as necessarily representing the official policies, either expressed or implied, of the Advanced Research Projects Agency or the U. S. Government.

Unclassified

SECURITY CLASSIFICATION OF THIS PAGE (When Data Entered)

REPORT DOCUMENTATION PAGE

READ INSTRUCTIONS BEFORE COMPLETING FORM

1. REPORT NUMBER: AFOSR-TR- 81-0612

2. GOVT ACCESSION NO.: AD-A102446

3. RECIPIENT'S CATALOG NUMBER:

4. TITLE (and Subtitle): Simulation of Short Period Lg, Expansion of Three-Dimensional Source Simulation Capabilities and Simulation of Near-Field Ground Motion from the 1971 San Fernando, California, Earthquake

5. TYPE OF REPORT & PERIOD COVERED: Final, Oct. 1, 1979-Nov. 30, 1980

6. PERFORMING ORG. REPORT NUMBER: SSS-R-81-5081

7. AUTHOR(s): T. C. Bache, H. J. Swanger, B. Skholler and S. M. Day

8. CONTRACT OR GRANT NUMBER(s): F49620-80-C-0019

9. PERFORMING ORGANIZATION NAME AND ADDRESS: Systems, Science and Software, P.O. Box 1620, La Jolla, California 92038

10. PROGRAM ELEMENT, PROJECT, TASK AREA & WORK UNIT NUMBERS: 61101E 0D60, AO 3990 2309/A1

11. CONTROLLING OFFICE NAME AND ADDRESS: Advanced Research Projects Agency, 1400 Wilson Boulevard, Arlington, Virginia 22209

12. REPORT DATE: July 1981

13. NUMBER OF PAGES: 152

14. MONITORING AGENCY NAME & ADDRESS (if different from Controlling Office): Air Force Office of Scientific Research, Building 410, Bolling AFB, 20332

15. SECURITY CLASS. (of this report): [illegible]

15a. DECLASSIFICATION DOWNGRADING SCHEDULE

16. DISTRIBUTION STATEMENT (of this Report): Approved for public release; distribution unlimited.

17. DISTRIBUTION STATEMENT (of the abstract entered in Block 20, if different from Report):

18. SUPPLEMENTARY NOTES:

19. KEY WORDS (Continue on reverse side if necessary and identify by block number): Lg, synthetic seismograms, nuclear explosion detection, earthquake simulation

20. ABSTRACT (Continue on reverse side if necessary and identify by block number):

This report summarizes three research efforts performed during the past fiscal year. The first of these efforts is a study of the theoretical behavior of the regional seismic phase Lg in various tectonic provinces. Synthetic seismograms are used to determine the sensitivity of Lg to source and medium properties. The primary issues addressed concern the relationship of regional Lg characteristics to the crustal attenuation properties, the comparison of Lg in many crustal structures and the source depth dependence of Lg.

DD FORM 1 JAN 73 1473 EDITION OF 1 NOV 65 IS OBSOLETE

Unclassified

SECURITY CLASSIFICATION OF THIS PAGE (When Data Entered)

unclassified

SECURITY CLASSIFICATION OF THIS PAGE(When Data Entered)

cont. The second effort described is an expansion of the capabilities of the three-dimensional finite difference code TRES. The present capabilities are outlined with comparisons of the performance of the code on three computer systems.

The last effort described is the development of an algorithm for simulation of the near-field ground motions from the 1971 San Fernando, California, earthquake. A computer code implementing this algorithm has been provided to the Mission Research Corporation for simulation of the acoustic disturbances from such an earthquake.

unclassified

SECURITY CLASSIFICATION OF THIS PAGE(When Data Entered)

TABLE OF CONTENTS

Section		Page
I.	INTRODUCTION	1
II.	COMPARISON OF MODAL AND TOTAL SOLUTIONS	4
	2.1 INTRODUCTION.	4
	2.2 COMPARISON WITH PROSE.	4
	2.3 COMPARISON WITH S^3'S DIRECT WAVE NUMBER INTEGRATION PROGRAM	6
III.	SYNTHESIS OF Lg WITH FREQUENCY-DEPENDENT Q	16
	3.1 INTRODUCTION.	16
	3.2 SYNTHETIC SEISMOGRAMS WITH THE MITCHELL (1980) VARIABLE Q MODEL	17
	3.3 SYNTHETIC Lg SEISMOGRAMS WITH MODIFIED VERSION OF MITCHELL'S (1980) FREQUENCY-DEPENDENT Q MODEL	27
	3.3.1 Introduction.	27
	3.3.2 Variations in the Q Near the Surface.	28
	3.3.3 A Modified Velocity Model	32
	3.4 CONCLUSIONS	32
IV.	SYNTHETIC Lg SEISMOGRAMS IN DIFFERENT TECTONIC PROVINCES	35
	4.1 INTRODUCTION.	35
	4.2 Lg IN AN OCEANIC CRUST	36
	4.3 Lg IN THE TIBETAN PLATEAU	39
	4.4 Lg IN A MODEL FOR THE CENTRAL U.S.	42
	4.4.1 Introduction.	42
	4.4.2 Effect of Crustal Thickness.	45
	4.4.3 Effect of the Shear Velocity at the Base of the Crust	49
	4.4.4 Lg in a Central U.S. Model Derived from Body Wave Refraction Data	52
	4.4.5 Amplitudes of the Synthetic Lg in the Central and Eastern U.S..	52
	4.5 COMPARISON OF SYNTHETIC Lg SEISMOGRAMS IN DIFFERENT CRUSTAL STRUCTURES	52

AIR FORCE OFFICE OF SCIENTIFIC RESEARCH (AFSC)
NOTICE OF TRANSMITTAL TO DDC
This technical report has been reviewed and is
approved for public release IAW AFR 190-12 (7b).
Distribution is unlimited.
D
Chief, Technical Information Division

TABLE OF CONTENTS (continued)

Section		Page
V.	DEPENDENCE OF Lg ON SOURCE DEPTH.	64
VI.	THREE-DIMENSIONAL SOURCE-SIMULATION CAPABILITIES	74
6.1	SUMMARY OF TASK 1	75
6.2	SUMMARY OF TASK 2	79
6.2.1	ILLIAC Computing Time.	80
6.2.2	CRAY Computing Time	82
6.2.3	UNIVAC Computing Time.	83
6.2.4	Summary	33
VII.	SIMULATION OF THE VERTICAL GROUND ACCELERATIONS IN THE 1971 SAN FERNANDO, CALIFORNIA, EARTHQUAKE	86
7.1	INTRODUCTION.	86
7.2	PAST STUDIES OF THE SAN FERNANDO FAULTING MECHANISM.	86
7.3	REPRESENTATION OF DISCRETE SOURCES OF RADIATION.	91
7.4	FREE SURFACE CORRECTION	100
7.5	DISCRIPTION OF ROUTINES	105
7.6	COMPARISON WITH NEAR-FIELD OBSERVATIONS.	108
REFERENCES.		112
APPENDIX A:	RUPTURE MODEL FOR MULTI-MATERIALS VERSION OF 14TRES.	116
APPENDIX B:	14TRES TEST PROBLEMS	126
APPENDIX C:	CONVERSION OF TRES TO THE CRAY I, AND PARTIAL VECTORIZATION	142

Accession For
NTIS GRA&I ☑
DTIC TAB ☐
Unannounced ☐
Justification
By
Distribution/
Availability Codes
Avail and/or
Dist Special
A

AIR FORCE OFFICE OF SCIENTIFIC RESEARCH (AFSC)
NOTICE OF TRANSMITTAL TO DDC
This technical report has been reviewed and is
approved for public release IAW AFR 190-12 (7b).
Distribution is unlimited.
A. D. BLOSE
Technical Information Officer

LIST OF ILLUSTRATIONS

Figure		Page
1.	Phase and group velocity dispersion for the model of Table 1	7
2.	Synthetic seismograms computed with modal superposition are compared with those computed with PROSE	8
3.	The modal solution at R = 50 kilometers is compared to the complete solution computed with the S-Cubed Direct wave-number integration program.	9
4.	The comparison of Figure 3 is repeated, except that Q is included in the calculations	11
5.	The comparison in Figure 4 is repeated without the seismometer response.	12
6.	The comparison of Figure 4 is repeated, except that the source depth is 3.0 kilometers	13
7.	Seismograms like those in Figure 6 are compared. The differences are that the Q is infinite and that the calculations are carried out to 5 Hz	14
8.	Synthetic seismograms for SALMON are plotted for two crustal models at two ranges	19
9.	Observed short period recordings of SALMON are shown from eight LRSM stations	20
10.	Amplitude data are plotted for SALMON and the synthetic Lg seismograms in Figure 8.	24
11.	Synthetic seismograms are plotted for two crustal models and a point double-couple source representing strike-slip earthquake faulting at a depth of 5 km.	25
12.	The SALMON synthetics for Model S12 are shown when computed with just seven modes	26
13.	Synthetic seismograms for the SALMON source and three crustal models.	30
14.	Synthetic seismograms for the model S16 described in the text.	33
15.	Phase and group velocity dispersion for the oceanic crust model of Table 6	38
16.	Synthetic seismograms are shown for several depths and ranges in the oceanic crustal model of Table 6	40
17.	Phase and group velocity dispersion for fifty modes in two Tibetan Plateau crustal models	43

LIST OF ILLUSTRATIONS (continued)

Figure		Page
18.	Synthetic seismograms are shown (R = 100 km) for the Tibetan Plateau crustal models of Table 7.	44
19.	Phase and group velocity dispersion for the central and eastern United States crustal models in Table 8	47
20.	Synthetic seismograms are plotted for three depths in the crustal models of Table 8.	48
21.	Phase and group velocity dispersion for fifty modes in the models M1 and M2.	50
22.	Synthetic seismograms are plotted for the strike-slip double-couple source in the model M2	51
23.	Phase and group velocity dispersion (fifty modes) for the modified central United States model in Table 7	54
24.	Synthetic seismograms are plotted for three strike-slip double-couple in the model C1.	55
25.	Synthetic Lg amplitudes as a function of source depth for the four crustal models considered.	56
26.	Comparison of synthetic seismograms (R = 200 km) for four crustal models	58
27.	Synthetic seismograms are compared at three source depths in a Tibetan Plateau crustal model (TP3) and four models for the central and eastern United States.	60
28.	Synthetic seismograms for three double-couple sources at various depths in the model S1	65
29.	Lg amplitudes as a function of source depth for fixed seismic moment at 1000 km in an EUS crustal model.	69
30.	Lg amplitudes as a function of source depth for fixed "m_b" at 1000 km in an EUS crustal model	72
31.	Free surface displacement waveforms for Test Problem I, computed with 14TRES (the ILLIAC IV version of the TRES code); displacements computed by two alternate methods are shown for comparison.	77
32.	Free surface displacements for 14TRES Test Problem II, compared to a two-dimensional finite element solution.	78
33.	Speed of execution of TRES, in zone-cycles per CPU-second	84
34.	Processed ground velocity observed at Pacoima Dam	89

LIST OF ILLUSTRATIONS (continued)

Figure		Page
35.	Source model for the San Fernando earthquake from Bache and Barker	90
36.	Coordinate system conventions used	93
37.	Typical shape of the Sato and Hirasawa model geometrical far-field acceleration	95
38.	Initiation-phase and stopping-phase amplitude as predicted by the S & H model for a 400 bar stress drop and 5 km fault radius, assuming a Q of 100	97
39.	Processed ground accelerations observed at Pacoima Dam	98
40.	Comparison of typical shapes of far-field acceleration from the Sato and Hirasawa model and the modified model used in this study	101
41.	Location of Pacoima Dam accelerograph site with the epicenters of the three discrete sources	109
42.	Comparison of observed and computed vertical ground velocities at Pacoima Dam	110

LIST OF TABLES

Table		Page
1	CRUSTAL MODEL FOR COMPARING COMPLETE AND MODEL SEISMOGRAMS.	5
2	FREQUENCY-DEPENDENT Q MODELS FOR THE EASTERN U.S.	18
3	THEORETICAL Lg AMPLITUDES FROM FIGURE 8 AND OBSERVED SALMON Lg AMPLITUDES.	23
4	MODIFIED FREQUENCY DEPENDENT Q MODELS FOR THE EASTERN UNITED STATES	29
5	Lg AMPLITUDES FROM SYNTHETIC SEISMOGRAMS	31
6	OCEANIC CRUSTAL MODEL FF2	37
7	TIBETAN PLATEAU MODELS FROM CHUN AND YOSHII	41
8	CENTRAL AND EASTERN UNITED STATES CRUSTAL MODELS	46
9	C1 BASE ON THE MODIFIED CENTRAL U.S. MODEL	53
10	TIMING COMPARISON OF TRES ON UNIVAC 1100/81, ILLIAC IV, AND CRAY I	81
11	SOURCE PARAMETERS.	102

I. INTRODUCTION

This report summarizes three distinct studies performed during the past fiscal year. The first study was the simulation of short period regional phases for the purpose of determining what physical characteristics of such phases might be used as a seismic discriminant. The second study was the expansion of the capabilities of the three-dimensional finite difference code TRES used for three-dimensional earthquake simulation. The last study was to provide an algorithm for simulation of the near-field ground motion from the 1971 San Fernando, California, earthquake which could be used by the Mission Research Corporation (MRC) for the simulation of the acoustic radiation generated by a moderate sized event.

The regional phase synthesis effort is described in Sections II through V. The results reported here are in addition to those reported previously in Bache et al., (1980), and the results of that study are not repeated here. In Section II, comparisons are made between Rayleigh wave multimode synthetic seismograms and those generated by algorithms producing the complete layered media response. The comparisons are quite favorable suggesting that modal solutions are adequate for describing the theoretical characteristics of the phase Lg at considerable savings compared to more robust methods.

In Section III, theoretical Lg codas are synthesized using earth models with frequency independent intrinsic attenuation. In Bache et al., (1980), it was suggested that frequency independent models of attenuation were not adequate for describing many of the characteristics observed in Lg. The proposed frequency dependent models were found to be no better for describing observed behavior of the short period motion. We hypothisize that many of the common features in the data are closely related to effects of scattering due to lateral inhomogenieties present along the propagation paths, and that these effects cannot be approximated by simple models of intrinsic attenuation.

In Section IV, synthetic short-period Lg codas are compared for many different crustal models. Using a published oceanic crustal model, synthetic seismograms do not contain anything resembling the phase Lg. It appears that the substantial velocity gradients present in the oceanic crustal model disperse the energy uniformly over a very wide group velocity interval, and nothing distinctive is seen in the window normally associated with Lg. Using suggested crustal models for the Tibetan Plateau, synthetic seismograms do suggest an Lg type phase. The lack of an efficient wave-guide is not a reasonable explanation as to why Lg is often not seen in that tectonic province. For all of the crustal models considered here, it is found that the Lg onset velocity is a few percent less than the shear velocity at the base of the crust. It appears that the Lg coda begins with the arrival of the shear wave critically reflected off the Moho.

In Section V, the depth dependence of Lg amplitudes on the depth of dislocation sources is examined. For vertical strike-slip and oblique thrust source mechanisms, the amplitudes of theoretical Lg is nearly independent of source depth confined to the crust for fixed m_b. For vertical dip-slip sources, a distinct depth dependence is seen.

Two tasks under this contract, allocated approximately ten man-weeks each, were directed toward development of an improved three-dimensional seismic source modeling capability, and they are described in Section VI. The first of these tasks was to provide support to Technology Development Corporation (TDC) in order to modify the ILLIAC IV version of the TRES finite difference code. The code modifications included the following: 1) a capability to model multiple material types, 2) incorporation of a shear-failure model for earthquake simulation, and 3) a scheme for modeling outcropping thrust faults.

The second of these tasks was to compare the performance of the TRES code on three computers: the ILLIAC IV, S^3's UNIVAC 1100/81, and the CRAY I computer at the National Center for

Atmospheric Research (NCAR). This task required conversion of the UNIVAC version of the TRES to the NCAR CRAY, followed by partial vectorization of the code to exploit the CRAY's vector processing capabilities. We conclude that the TRES code now executes large jobs with speed comparable to that of the ILLIAC, and we estimate that full optimization will lead to further improvement of approximately a factor of four in speed.

Section VII describes an algorithm for simulating the near-field ground acceleration expected in the 1971 San Fernando, California, earthquake. This ground motion is to be used as a driver for simulating the acoustic radiation for that event. The procedures established for the simulation of the atmospheric disturbances require a relatively simple and efficient algorithm for determining the ground response which is reasonably accurate in the intermediate frequency band (.5 to 3 Hz). The source model employed was guided by previous studies of the near-field and teleseismic data. It approximates the rupture process using three distinct sources of radiation. The ground motion is computed using an intuitive approximation for the radiation expected from a localized propagating shear crack. Comparisons are shown between the ground velocity computed using the algorithm and the ground velocity observed at Pacoima Dam.

Sections II through V were prepared by T. C. Bache and H. J. Swanger; Section VI was prepared by S. M. Day and B. Shkoller, and Section VII was prepared by H. J. Swanger.

II COMPARISON OF MODAL AND TOTAL SOLUTIONS

2.1 INTRODUCTION

The normal modes provide a partial solution for the elastic waves in a plane-layered earth model. Our assumption is that this partial solution is a very good approximation to the total solution for many problems in regional seismology, particularly for the synthesis of Lg and late arriving seismic energy. Testing this assumption requires comparison with an "exact" solution.

Detailed studies of the performance of modal approximations of SH-motion have been given by Herrmann (1977) and Swanger and Boore (1978). These studies have demonstrated that Love wave modes make up nearly all SH wave energy at distances beyond a few crustal thickneseses. The performance of Rayleigh modes in P-SV problems has not been thoroughly investigated.

In our last report (Bache et al., 1980) we described a comparison of modal seismograms with seismograms computed with the PROSE program (Apsel, 1979), a direct wave-number integration program that computes the total solution. This comparison resulted in some ambiguous results which turned out to be primarily due to differences in the way the filter representing the seismometer response was specified. Subsequent to the PROSE comparisons, Henry Swanger and Boris Shkoller developed a new wave-number integration program which is similar in many respects to PROSE. This program was used to compute total seismograms for comparison with the modal solution. The comparison confirms that the P-SV modes give an excellent approximation to the total solution for arrivals with group velocities less than the shear velocity of the underlying halfspace.

2.2 COMPARISON WITH PROSE

The PROSE calculations were done by Dr. John Orcutt of the Scripps Institute of Oceanography. The structure is listed in Table 1 and the phase and group velocity dispersion for all the modes (66)

TABLE 1

CRUSTAL MODEL FOR COMPARING COMPLETE AND MODAL SEISMOGRAMS

Depth (km)	Thickness (km)	α (km/sec)	β (km/sec)	ρ (gm/cm^3)	Q
1.5	1.5	3.7	2.16	2.10	35
8.0	6.5	6.1	3.3	2.85	250
34.0	26.0	6.6	3.59	3.05	1800
∞	∞	8.1	4.52	3.35	2000

between 0 and 5 Hz is plotted in Figure 1. The source was a strike-slip double-couple at a depth of 1 km. The azimuth was 45° from the strike and the source time function was a step with a moment of 10^{22} dyne-cm. The WWSSN short period instrument response was included and the spectrum was tapered to zero between 0.5 and 1.0 Hertz with a cosine-squared filter. Thus, the seismograms include no energy above 1 Hertz (only 14 modes contribute to the modal solution).

The comparison of the modal and PROSE seismograms from Bache, et al, (1980) is shown in Figure 2. The waveform agreement is quite good and indicates that most of the important energy is included in the modal solution. The amplitude comparison is not as good. This turned out to be primarily due to a different specification of the WWSSN short period seismometer response. More complete comparisons which are done in an entirely consistent way are described in the next section.

2.3 COMPARISON WITH S^3'S DIRECT WAVE NUMBER INTEGRATION PROGRAM

A new direct wave-number integration program was developed by Henry Swanger and Boris Shkoller of S^3 to compute the complete solution. This program does essentially the same calculation as PROSE, but the formulation and numerical procedures are different in detail.

The first comparison with the results of this new direct wave-number integration program is shown in Figure 3. The seismograms were computed the same as the R = 50 km case in Figure 2, except that the structure (Table 1) was modified to include infinite Q.

The complete solution was done with a Nyquist frequency of 1.0 Hz, hence the time step was 0.5 seconds and the seismograms have a jagged appearance. The time series for the modal calculations was sine interpolated to a time step of 0.1 seconds by filling the spectrum with zeros between 1 Hertz and a 5 Hertz Nyquist frequency.

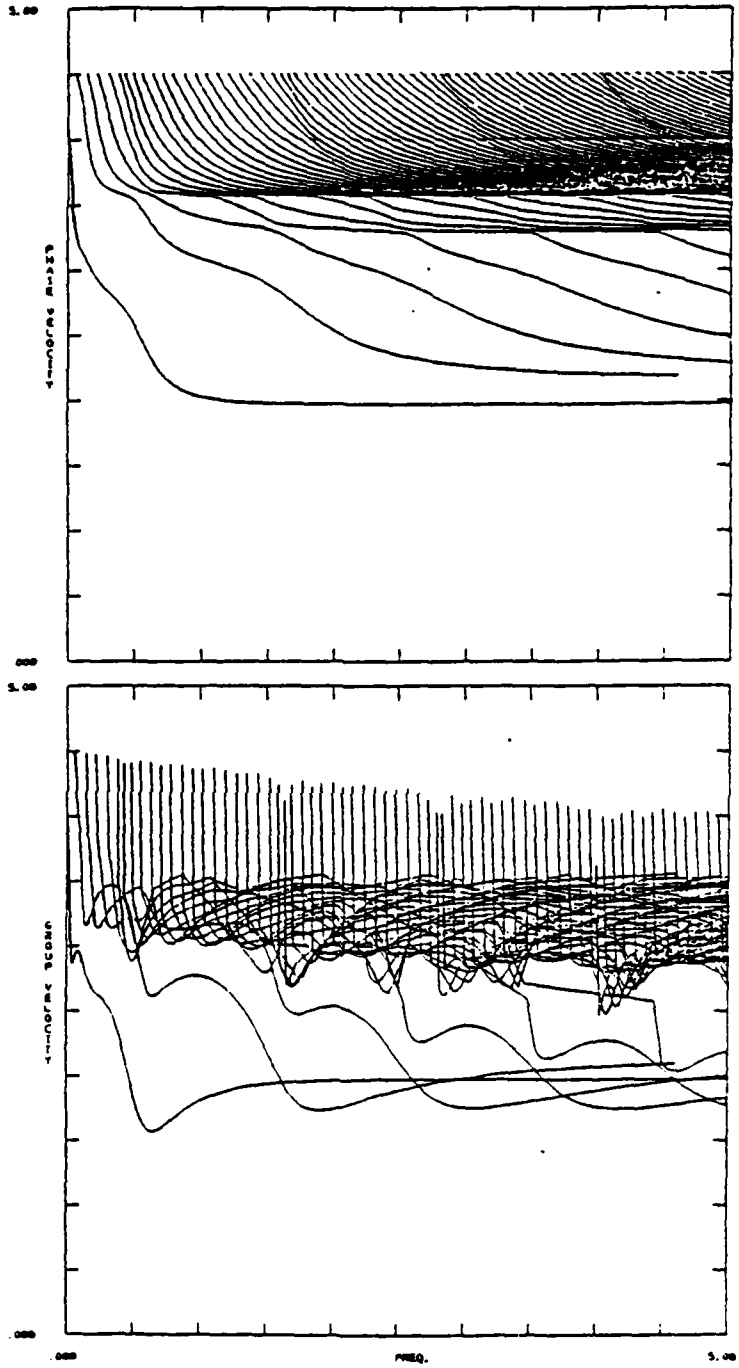

Figure 1. Phase and group velocity dispersion for the model of Table 1.

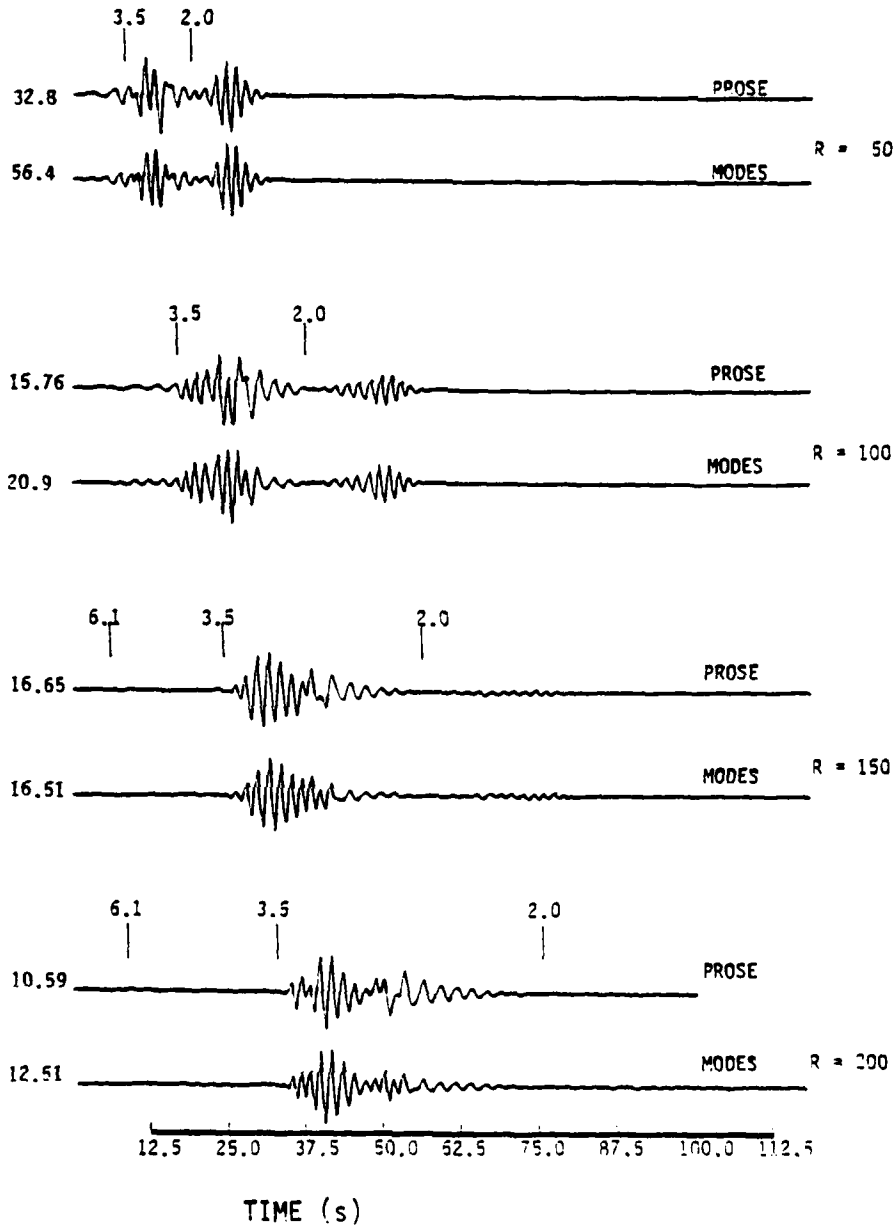

Figure 2. Synthetic seismograms computed with modal superposition are compared with those computed with PROSE. Zero on the time scale of the plots is reduced by R/8.1. The maximum peak-to-peak amplitude in microns is shown at the left and several interesting group velocities are marked in each set.

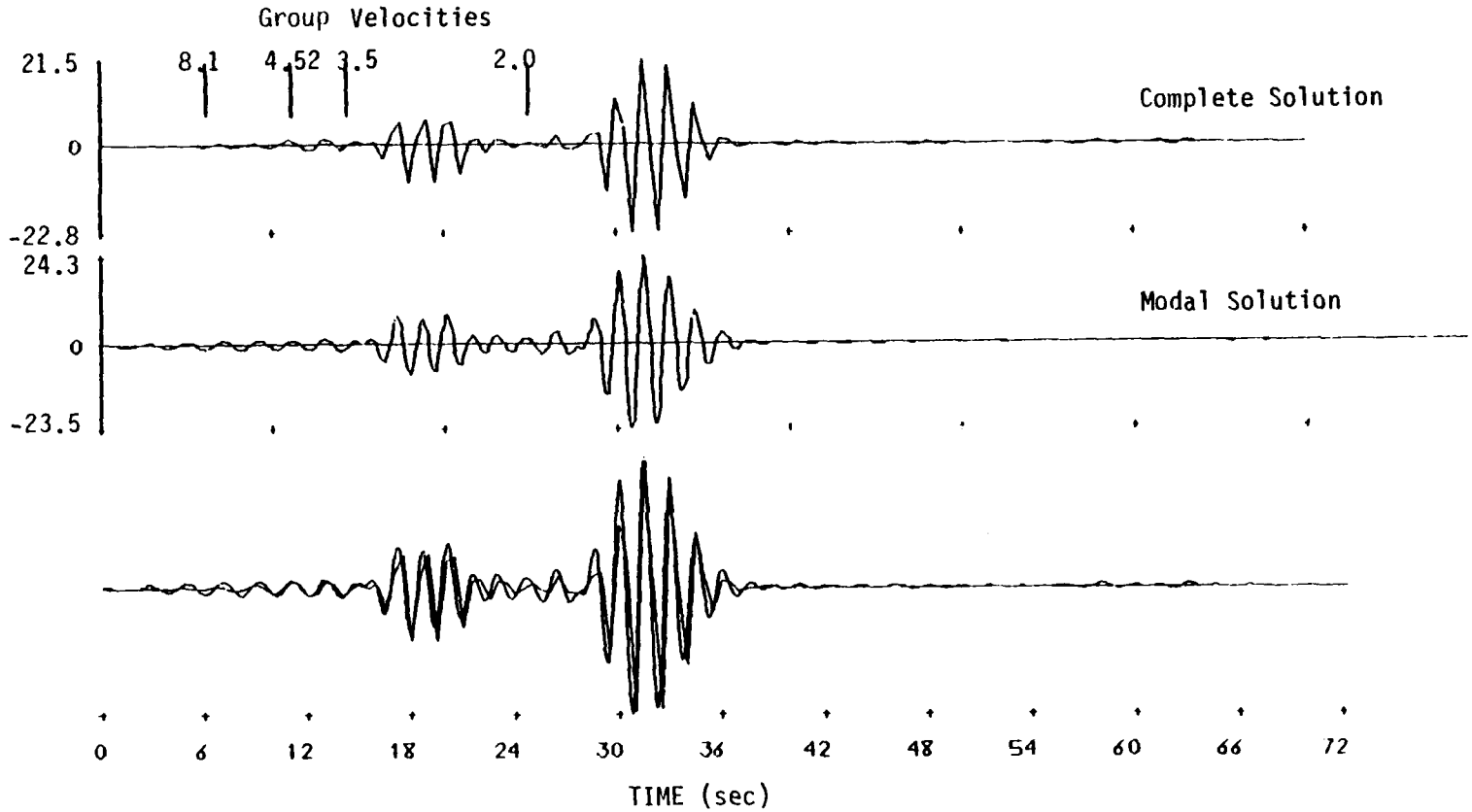

Figure 3. The modal solution at R = 50 kilometers is compared to the complete solution computed with the S-Cubed direct wave-number integration program. The peak amplitudes in microns are shown at the left of the individual seismograms and the two are plotted together at the bottom.

Several more comparisons are shown in Figures 4 to 7. First, in Figure 4 we repeat the comparison of Figure 3, this time including the Q. The same comparison is shown in Figure 5 without the WWSSN short period instrument response. In Figure 6 the seismograms (with Q and the seismometer included) are shown for a source depth of 3.0 km.

The most complete comparison is shown in Figure 7. The source and azimuth are the same as for all comparisons in this section. The depth is 3.0 km and the elastic (infinite Q) version of the structure in Table 1 was used. This time the calculations were done with a Nyquist frequency of 5.0 Hz. The phase and group velocity dispersion for the modes were shown in Figure 1. There are 66 modes from 0 to 5 Hertz. The seismograms in Figure 7 include the WWSSN short period instrument response and the spectra for both cases were tapered between 4.5 and 5.0 Hertz with a cosine-squared filter.

The comparisons in Figure 3 to 7 demonstrate that the modes give a remarkably accurate approximation for the complete ground motion in the group velocity window < 4.5 km/sec. The comparison in Figure 7 is a particularly good demonstration of this point. The complete and modal solutions have almost the same phasing; that is, zero crossings and breaks in the waveform occur at nearly the same time in both. Differences between the two are mainly in the amplitudes of the peaks, but even these differences are, at most, 30 to 40 percent.

Our comparison suggests that Rayleigh modes are adequate for describing the characteristics of Lg. In this study, we will restrict our attention to modal synthesis of Lg even though complete solutions are obtainable. Modal solutions have two major advantages over complete solutions. First, modal solutions are constructed from intermediate results which allow for better interpretation of the final seismograms. As demonstrated in our last report (Bache et al., 1980), the dispersion parameters and modal energies provide a great deal of information lost within the "black-box" of complete seismogram programs. Second, modal

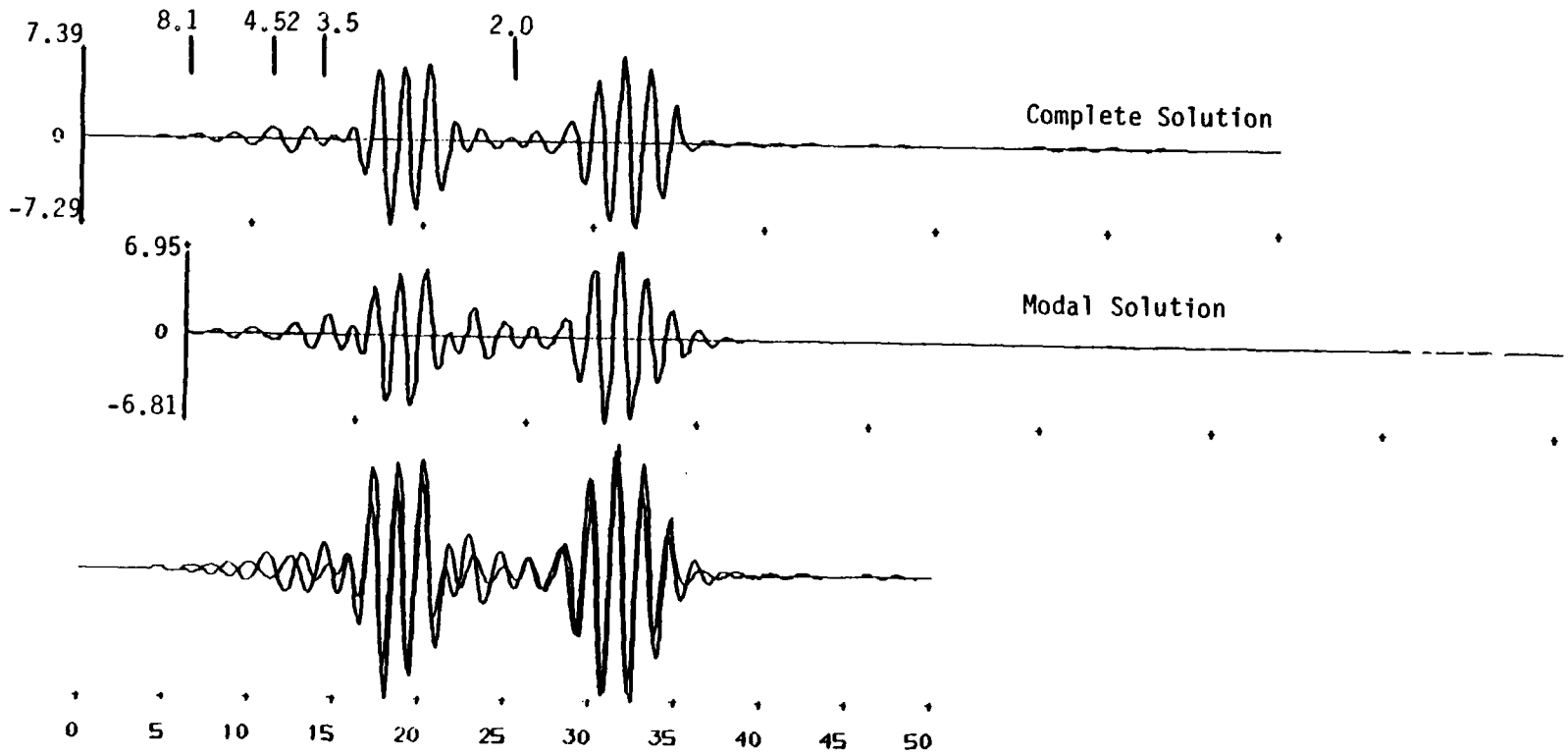

Figure 4. The comparison of Figure 3 is repeated, except that Q is included in the calculations.

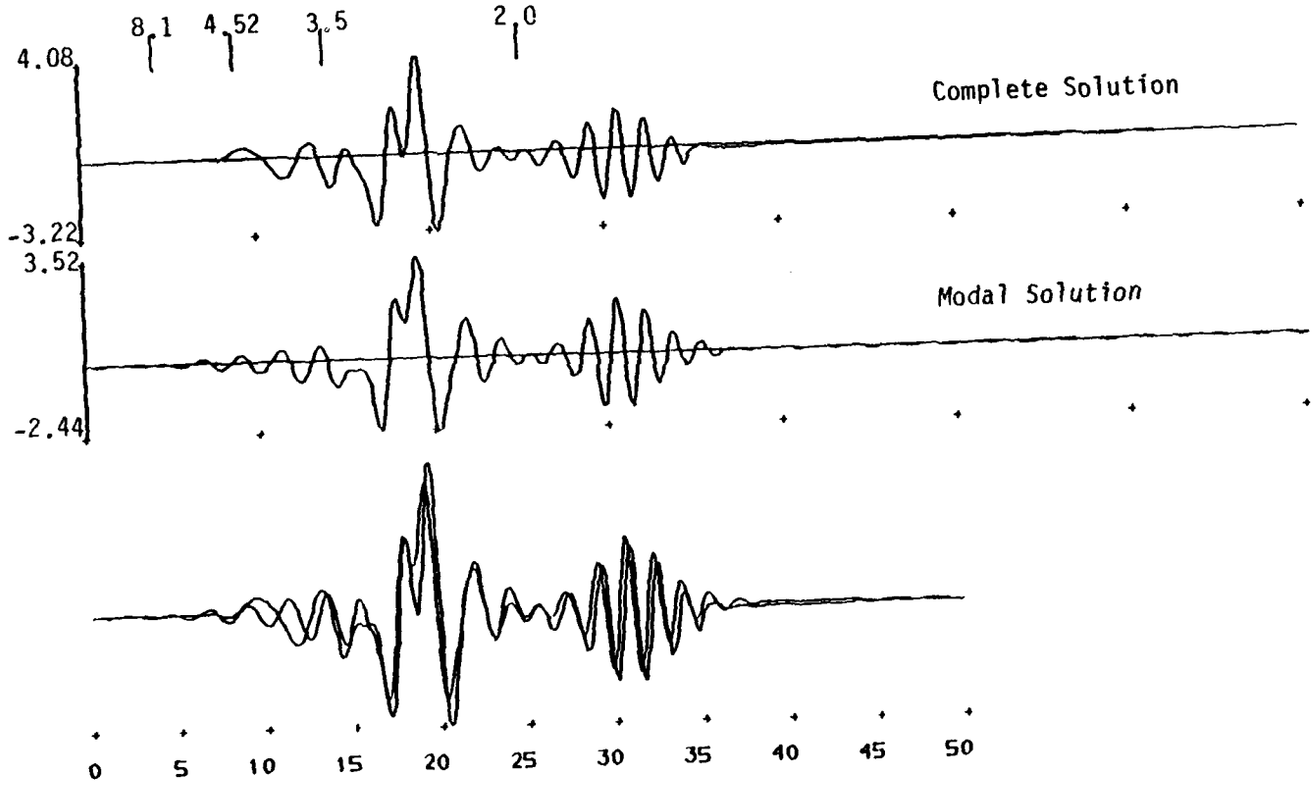

Figure 5. The comparison in Figure 4 is repeated without the seismometer response.

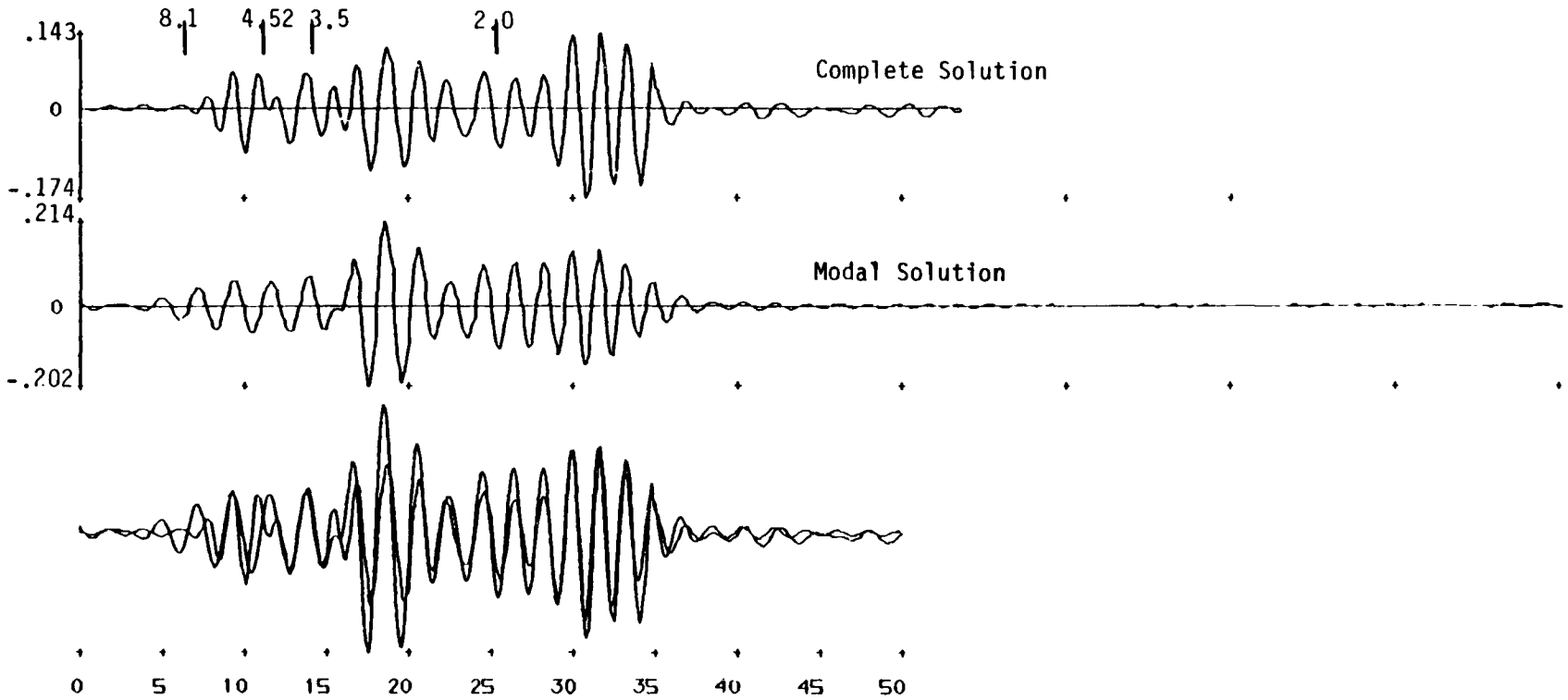

Figure 6. The comparison of Figure 4 is repeated, except that the source depth is 3.0 kilometers.

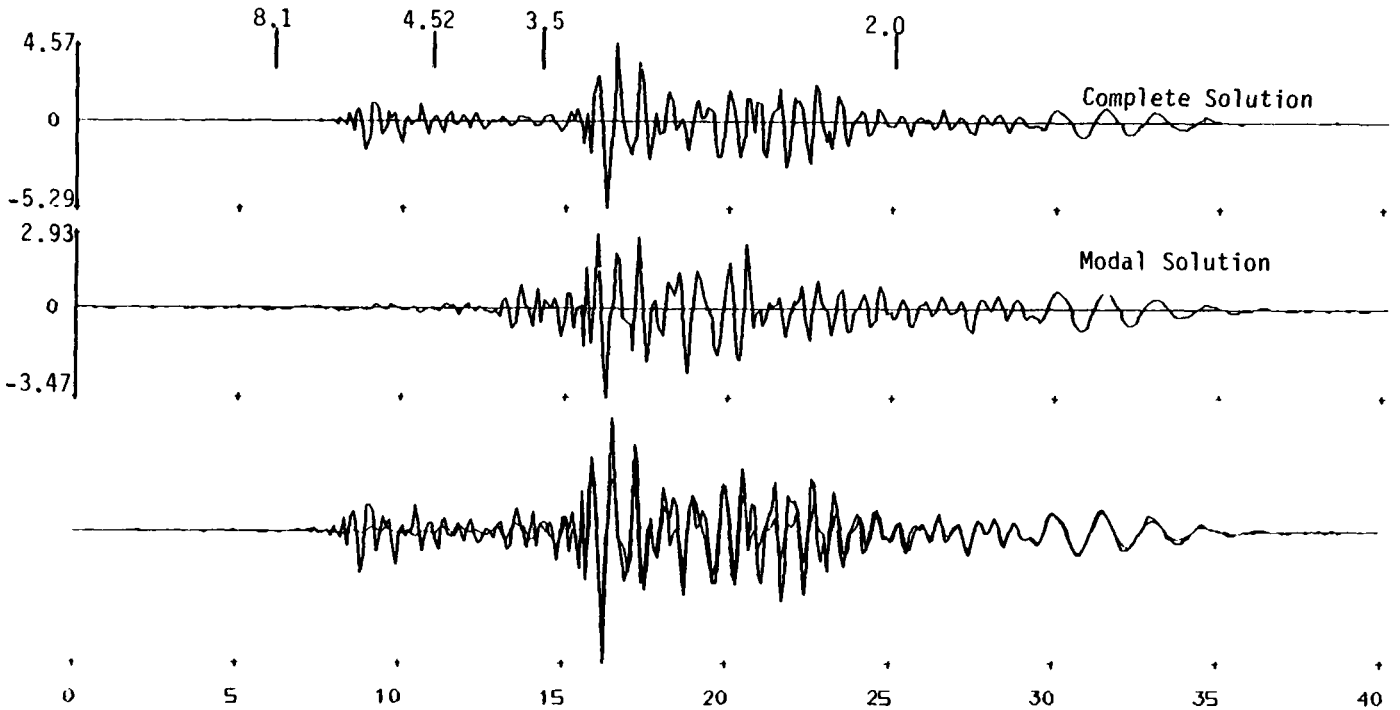

Figure 7. Seismograms like those in Figure 6 are compared. The differences are that the Q is infinite and that the calculations are carried out to 5 Hz.

solutions have significant cost advantages over complete solutions. Our experiences suggest that the cost of obtaining all the needed dispersion parameters for a given earth structure is three or four times less than that needed to compute a single complete regional seismogram. Once the dispersion functions are obtained, a modal seismogram costs about one-hundredth that of a complete seismogram.

III. SYNTHESIS OF Lg WITH FREQUENCY-DEPENDENT Q

3.1 INTRODUCTION

In our semi-annual report (Bache et al., 1980) we focused our attention on the synthesis of Lg using plane-layered, laterally homogeneous earth models with frequency-independent Q. While many of the important qualitative features of observed Lg can be reproduced with such models, we found there were three basic deficiencies that appeared to be impossible to remove, as long as we are confined to this restricted class of earth models. These are:

1. The synthetics do not include the high frequency energy arriving with apparent velocities slower than 2.9 km/sec that is a prominent feature of the observations.

2. The synthetic spectra fall off more rapidly at high frequencies than the observed spectra from the SALMON nuclear explosion.

3. The amplitude attenuation with range is much faster than is observed in the eastern United States for earthquakes or explosions.

To what can we attribute these deficiencies? The failure to include multipathing and scattering by lateral heterogeneities is likely to contribute to the first of them. But the other two (and, perhaps, some of the first) are likely to be caused by the assumption of frequency-independent Q.

In this section we study the effects of allowing the Q to be frequency-dependent. In evaluating the models we are mostly concerned with their ability to replicate the observed amplitude attenuation. This is observed for many events at different depths and locations. The spectral characteristics are also important, but are more difficult to evaluate because of uncertainties about the source.

3.2 SYNTHETIC SEISMOGRAMS WITH THE MITCHELL (1980) VARIABLE Q MODEL

Mitchell (1980) points out that frequency-independent Q models inferred from fundamental mode Rayleigh wave observations in eastern North America are not consistent with the observed attenuation of Lg in this region. This is, of course, one of the points made in our semi-annual report. To resolve this, Mitchell (1980) assumed

$$Q_\beta^{-1}(\omega,z) = C(z)\ \omega^{-\zeta}, \qquad (1)$$

and obtained several $Q_\beta^{-1}(\omega,z)$ models corresponding to different ζ. Observations of the attenuation of Lg between 1 and 10 seconds in eastern North America were then used to select the best values for ζ.

Assuming ζ is frequency-independent, Mitchell (personal communication) finds that the best fit to the data is provided by either of the models S11 or S12 listed in Table 2. The velocity profile is based on the model fit to Rayleigh waves by McEvilly (1964), which has a 38 km crust. This model, which is discussed in more detail in Section 4.4, has been modified by adding some lower velocity material in the top 4.1 kilometers. As was discussed by Bache, et al. (1980), this seems to be necessary to avoid having the short period synthetics be dominated by a pulse-like arrival associated with the fundamental mode trapped in the near-surface layers.

Synthetic seismograms for models S11 and S12 are plotted at two ranges, 500 and 1000 km, in Figure 8. Fifty modes were used for these calculations. The source is a reduced displacement potential for the SALMON explosion given by Murphy (1969) and is at a depth of 0.83 kilometers, which is appropriate for SALMON. The LRSM short period seismometer response is included in the synthetics. The synthetics for the two models are very similar, with the main difference being in the peak amplitudes.

The SALMON observations recorded by LRSM seismometers at ranges near 250 and 1200 km are plotted in Figure 9 at the same time

TABLE 2

FREQUENCY-DEPENDENT Q MODELS FOR THE EASTERN U.S.
(Mitchell, personal communication)

Layer	Depth (km)	Thickness (km)	α (km/sec)	β (km/sec)	ρ (km/sec)	S11 (ζ=0.3) C	S12 (ζ=0.2) C
1	0.6	0.6	3.7	2.16	2.1	245	245
2	1.0	0.4	4.55	2.54	2.2	575	480
3.	2.6	1.5	4.55	2.54	2.2	610	505
4	4.1	1.5	5.60	3.14	2.65	590	510
5	11.0	6.9	6.10	3.50	2.70	500	410
6	16.0	5.0	6.40	3.68	2.90	630	490
7	20.0	4.0	6.40	3.68	2.90	990	750
8	25.0	5.0	6.70	3.67	2.90	1400	1040
9	31.0	6.0	6.70	3.67	2.90	2280	1700
10	38.0	7.0	6.70	3.67	2.90	2780	2160
11	43.0	5.0	8.15	4.67	3.30	3235	2600
12	49.0	6.0	8.15	4.67	3.30	5075	4170
13	∞	∞	8.15	4.67	3.30	6150	5200

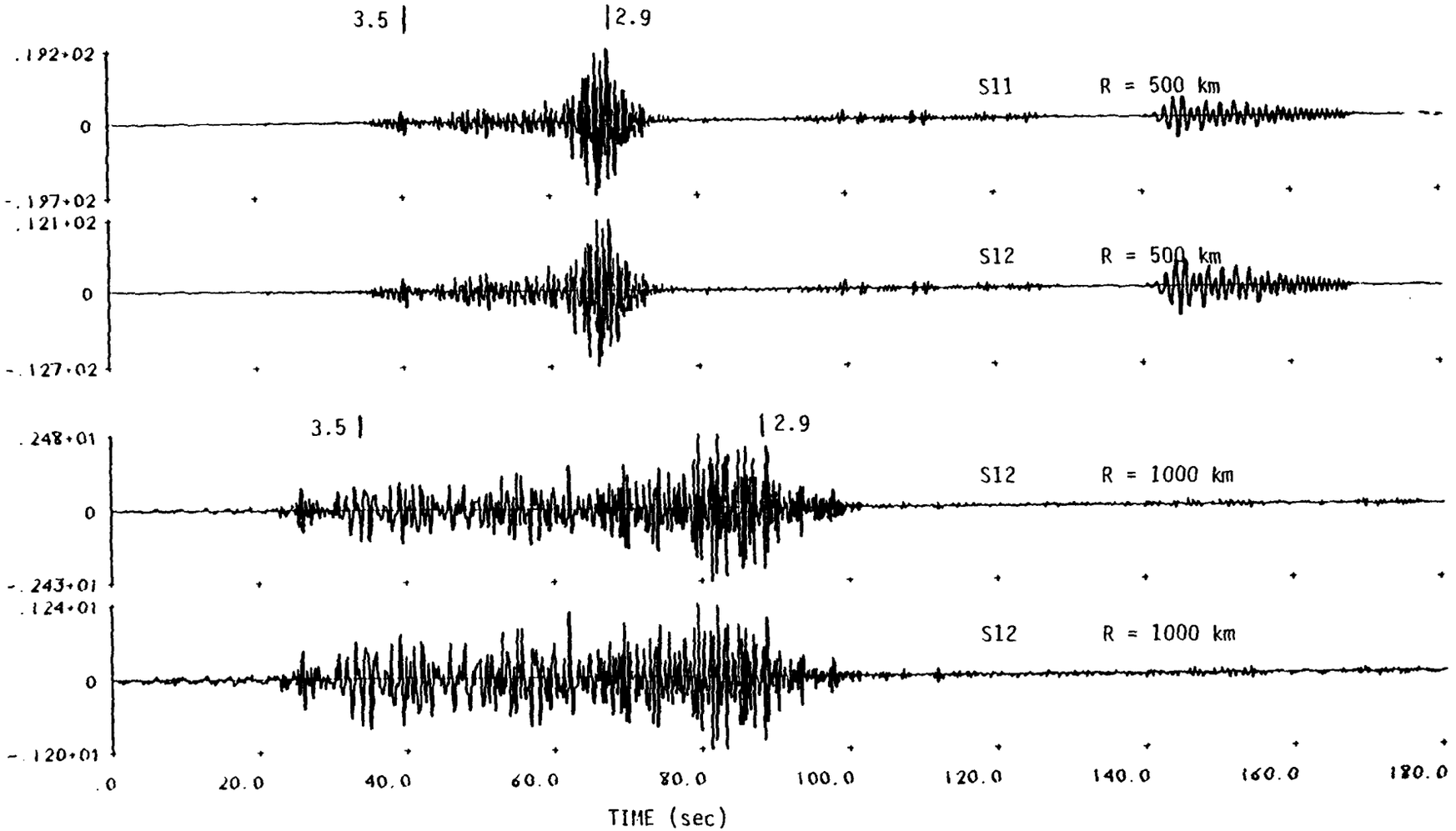

Figure 8. Synthetic seismograms for SALMON are plotted for two crustal models at two ranges. The source is a reduced displacement potential from Murphy (1969) at a depth of 0.83 kilometers. The LRSM short period seismometer response is included.

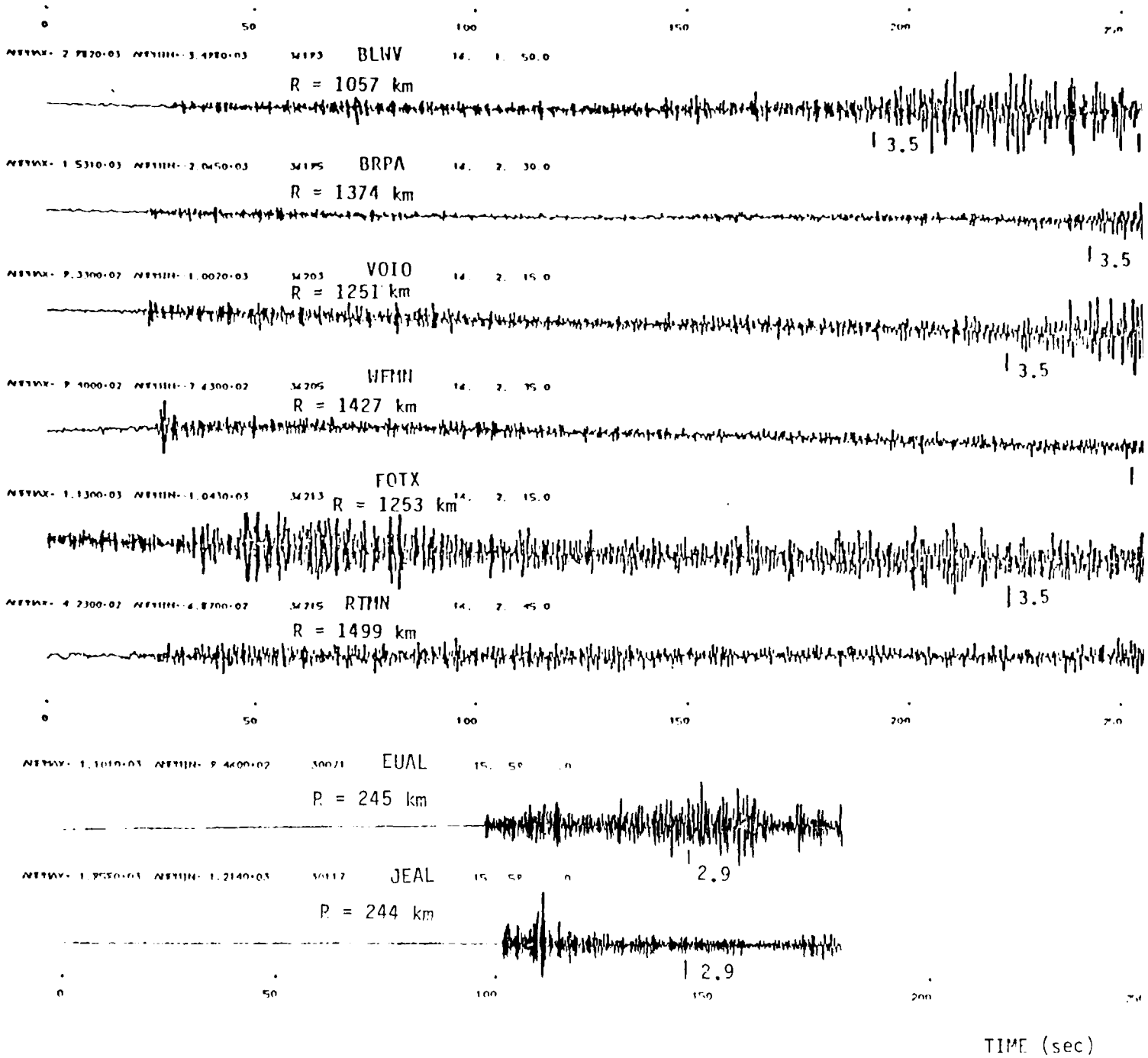

Figure 9. Observed short period recordings of SALM
and minimum amplitudes are indicated alo
event origin time was 16:00.0). The tim
indicated on each record.

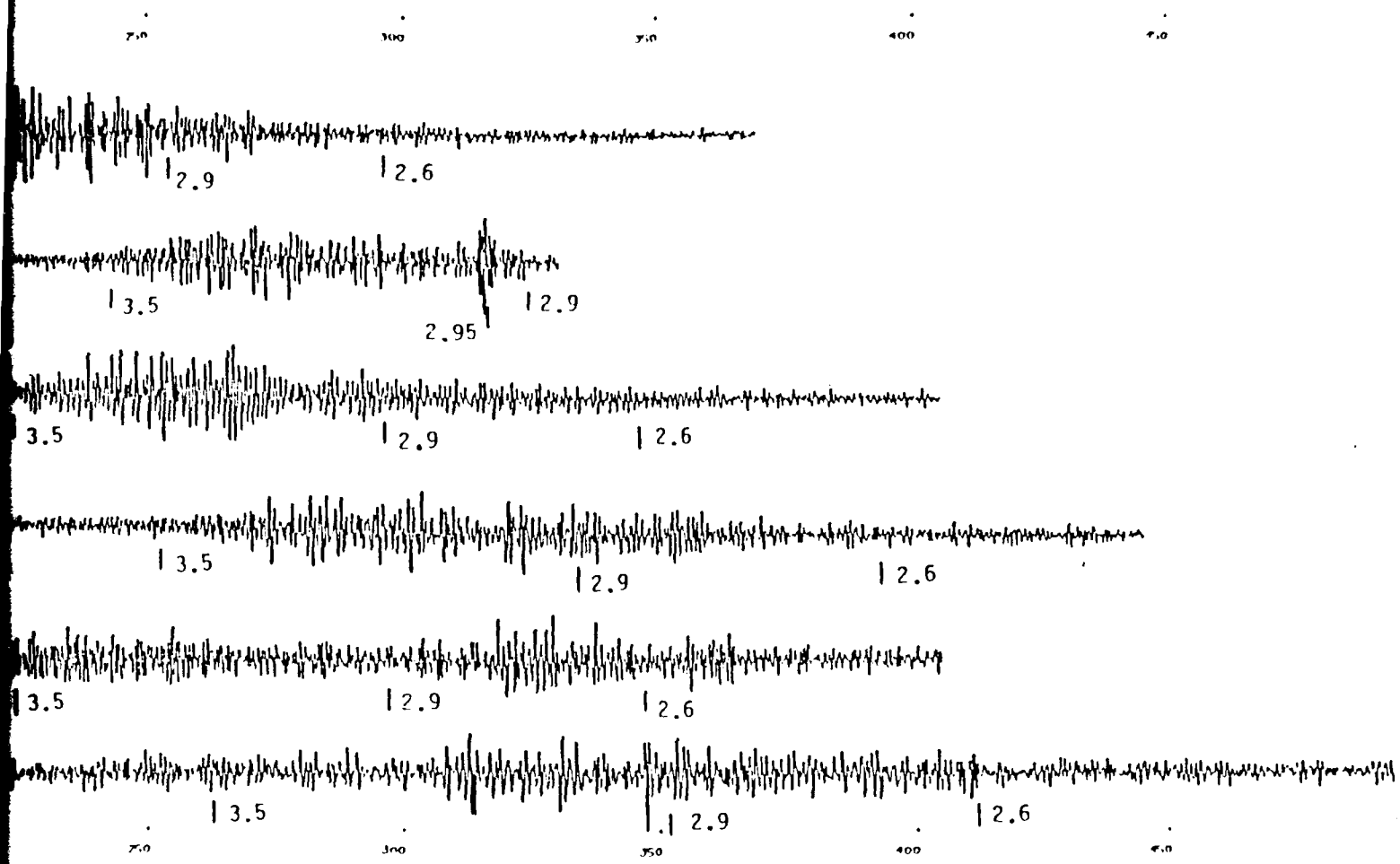

IME (sec)

ings of SALMON are shown from eight LRSM stations. The maximum
ndicated along with the time of zero on the time scale (the
0). The times for several apparent group velocities are

scale as the synthetics in Figure 8. Comparing the two, it appears that the synthetics have too much high frequency energy, especially at the larger range. Also, there is no indication in the data of the large amplitudes that arrive with an apparent velocity of about 3.05 km/sec on the R = 500 km synthetics. This arrival can also be seen at R = 1000 km, though it is less prominent.

For evaluating synthetics like those in Figure 8, we will primarily examine the apparent amplitude attenuation of Lg. This is a concept introduced by Nuttli (1973), who assumed that Lg attenuates with distance as

$$\Delta^{-1/3} \sin\Delta^{-1/2} \exp(-\gamma\Delta), \qquad (2)$$

where the Δ is the range and γ is the apparent attenuation. Plotting Lg amplitude versus range, Nuttli (1973) found the γ providing the best fit to the trend of the data. This technique has been used by several others to fit various sets of Lg amplitudes in eastern North America (e.g., Bollinger, 1973, 1979; Street, 1976). The consensus is that the γ for this region is about 0.07 to 0.11 deg^{-1}. The sparsely sampled Lg amplitudes for the SALMON data in Figure 9 are consistent with these values, though they are probably best fit with slightly larger γ, about 0.12 deg^{-1} or so (see Figure 10).

The convention for the Lg amplitude on the synthetics and SALMON data was to measure the maximum (3 cycles or so) sustained amplitude within about ten seconds of the arrival time associated with a 3.5 km/sec group velocity. The synthetic γ is then computed from (2). That is,

$$\gamma_{syn} = (\Delta_2 - \Delta_1)^{-1} \ln\left[\left(\frac{\Delta_1}{\Delta_2}\right)^{1/3}\left(\frac{\sin\Delta_1}{\sin\Delta_2}\right)^{1/2} \frac{A_1}{A_2}\right] \qquad (3)$$

where A is the Lg amplitude and subscripts 1 and 2 refer to the two ranges.

The Lg amplitudes for the two models are listed in Table 3. Also listed are Lg amplitudes from the SALMON observations in Figure 9. Using (3), the γ_{syn} for both models is 0.18 deg^{-1}, which is larger than the observed γ. Also, the Lg amplitudes are very much larger than the observed values for SALMON. All these amplitude data are plotted in Figure 10.

Do the models give a γ more like the data for deeper earthquake sources? To address this question we computed the synthetics shown in Figure 11. In this case, the source is a strike-slip point double-couple at a depth of 5 km, with a step function time history represented by a moment of 10^{25} dyne-cm. The synthetics are computed at an azimuth 30° from the strike and the WWSSN short period seismometer response is included. As with the explosion source, the two models give nearly the same synthetics except for an amplitude scaling. Measuring the Lg amplitudes on those synthetics and computing γ_{syn} from (3), we find that γ_{syn} = 0.20 deg^{-1} for both models. Thus, we see that the γ_{syn} is not very dependent on the source type.

In his analysis leading to the frequency-dependent Q models in Table 3, Mitchell (1980) considers the excitation functions of the first six higher modes and concludes that the results of his study do not depend critically on the number of modes employed at any period. To check the validity of the assumption, we repeated the SALMON synthetics for model S12 from Figure 8, this time with seven modes (rather than the fifty used before). The resulting synthetic seismograms are shown in Figure 12.

The seven mode synthetic seismograms are not very realistic looking when filtered to emphasize the short periods, as they are in Figure 12. These seismograms are dominated by the fundamental mode. It is yet higher modes, which are associated with propagation at the base of the crust, that are most important for the high frequency energy near 3.5 km/sec. This is discussed in more detail by Bache, et al. (1980).

TABLE 3

THEORETICAL Lg AMPLITUDES FROM FIGURE 8 AND OBSERVED SALMON Lg AMPLITUDES

Model	Range (km)	Lg* (nm)
S11	500	6950
S11	1000	1710
S12	500	5310
S12	1000	1340
	SALMON OBSERVED	
Station		
JELA	244	2746
EUAL	245	2649
BLWV	1057	259
VOIO	1251	279
BRPA	1374	240
WFMN	1427	153

* Uncorrected for frequency-dependent seismometer response.

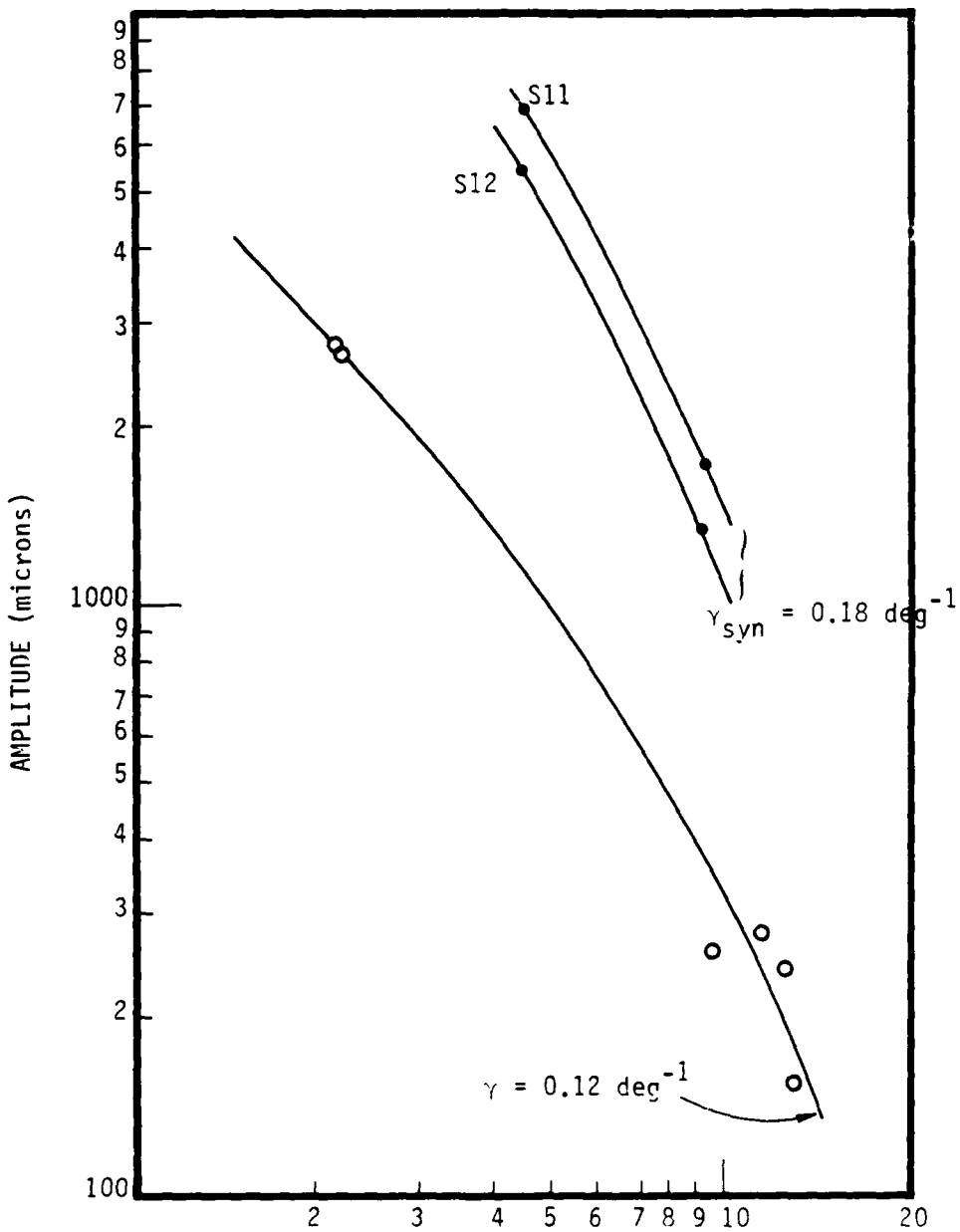

Figure 10. Amplitude data are plotted for SALMON and the synthetic Lg seismograms in Figure 8.

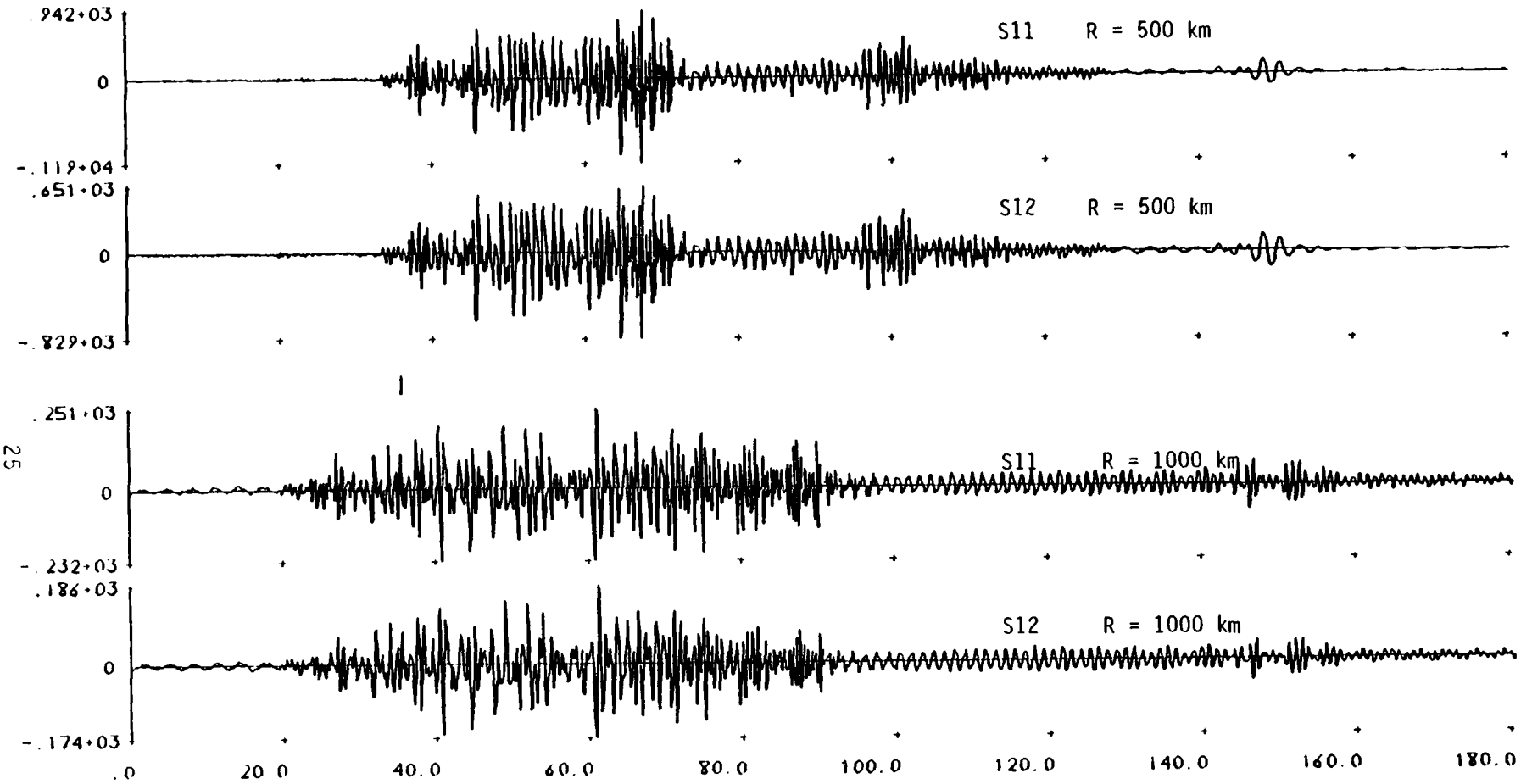

Figure 11. Synthetic seismograms are plotted for two crustal models and a point double-couple source representing strike-slip earthquake faulting at a depth of 5 km. The azimuth is 30 degrees from the strike. The source time function is a step with $M_0 = 10^{25}$ dyne-cm and the WWSSN short period seismometer response is included.

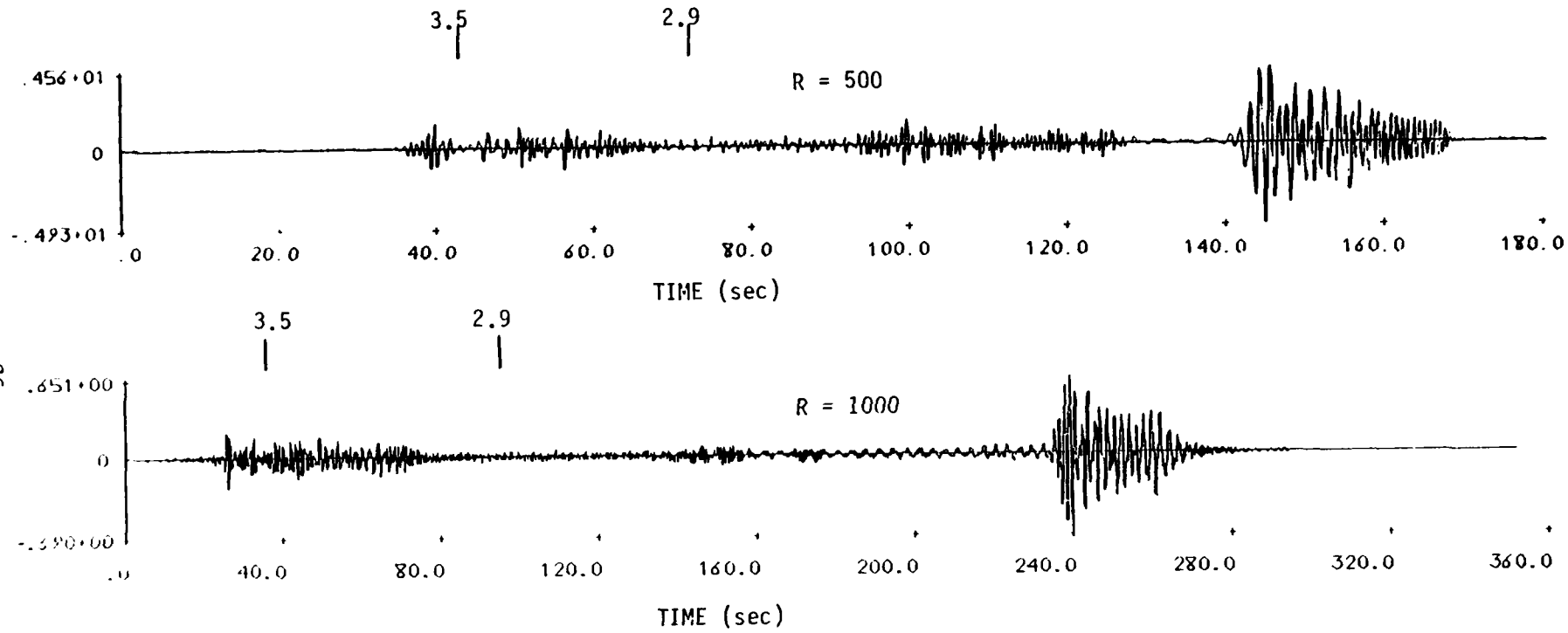

Figure 12. The SALMON synthetics for Model S12 are shown when computed with just seven modes. Note that the time scale is different on the two plots.

The Lg amplitudes for the seismograms in Figure 12 are 1430 nm at 500 km and 240 nm at R = 1000 km. These are much smaller than the amplitudes of 5310 nm and 1340 nm from the fifty mode synthetics in Figure 8 (Table 3). Using (3), the γ_{syn} for the seven mode synthetics is 0.27. This is higher than the γ_{syn} for the 50 mode synthetics because the lower modes are associated with propagation at shallower depths where Q is lower.

We are forced to the conclusion that there is no simple way to characterize the attenuation of Lg using qualitative ideas, as in Mitchell (1980). It is necessary to consider a large number of modes, which is probably only practical by examining synthetic seismograms. From the synthetic Lg seismograms we find that the Lg amplitude attenuation is much greater than that observed. Therefore, the frequency-dependent model proposed by Mitchell (1980) is not consistent with observed Lg amplitude attenuation in Eastern North America, at least in the band passed by the LRSM and WWSSN short period seismometers.

3.3 SYNTHETIC Lg SEISMOGRAMS WITH MODIFIED VERSION OF MITCHELL'S (1980) FREQUENCY-DEPENDENT Q MODEL

3.3.1 Introduction

The frequency-dependent Q models proposed by Mitchell (1980) fail to give Lg seismograms that match essentially the same three data features listed in the introduction (Section 3.1) to this section. That is, the synthetics do not match the duration beyond 2.9 km/sec, the spectral content and the apparent amplitude attenuation. The frequency-dependent Q model has very little effect on the duration. This is an indication that the observed energy arriving later than 2.9 km/sec is probably more strongly associated with multi-pathing and scattering by lateral heterogeneities than with Q.

The frequency-dependent Q model does allow much more high frequency energy into the Lg spectrum. In fact, it changes the spectral content too far in this direction; the synthetics now appear to have too much high frequency energy. Finally, we have apparent amplitude attenuation (γ_{syn}), the observed data feature that we are most concerned with reproducing in this section. The frequency-dependent models S11 and S12 have too large a γ_{syn}. At the same time, the absolute amplitudes are much larger than those observed for SALMON, assuming the SALMON source is reasonably well known. Thus, the model we are seeking must have more attenuation to reduce the absolute amplitudes and the high frequency content of the synthetic Lg phases. At the same time it must have a lower γ_{syn}, which suggests higher Q. These requirements appear to be contradictory, and so will be very difficult to fulfill. In this section we describe some experiments to see just how difficult.

3.3.2 Variations in the Q Near the Surface

The first experiment is to change the Q in the top layers. The Q in these layers is not very well resolved by Mitchell's procedure, so we should have some flexibility. The first three models are called S13, S14 and S15. The Q for these models, and for S11 and S12 from Table 2, are listed in Table 4. Only the Q in top 4.1 kilometers is altered.

Synthetic seismograms like those in Figure 8 are plotted for models S13, S14 and S15 in Figure 13. The source is that for SALMON. The waveforms are little different from those in Figure 8. The Lg amplitudes are summarized in Table 5 (the model S16 will be discussed later), together with the γ_{syn} computed from (3). We see that lowering the Q near the surface has had the effect of increasing the effective attenuation of the entire Lg phase. The amplitudes are smaller and the γ_{syn} is larger. We conclude that no minor fixes, like those represented by the models in Table 5, will make these frequency-dependent Q models compatible with the three important characteristics of the data that we have been discussing.

TABLE 4

MODIFIED FREQUENCY DEPENDENT Q MODELS
FOR THE EASTERN UNITED STATES

Layer	Depth (km)	β (km/sec)	S12 (ζ=0.2)	S13 (ζ=0.2)	S11 (ζ=0.3)	S14 (ζ=0.3)	S15 (ζ=0.3)
1	0.6	2.16	245	50	245	50	25
2	1.0	2.54	480	100	575	250	125
3	2.6	2.54	505	505	610	300	150
4	4.1	3.14	510	510	590	300	150
			S12 Model		S11 Model		

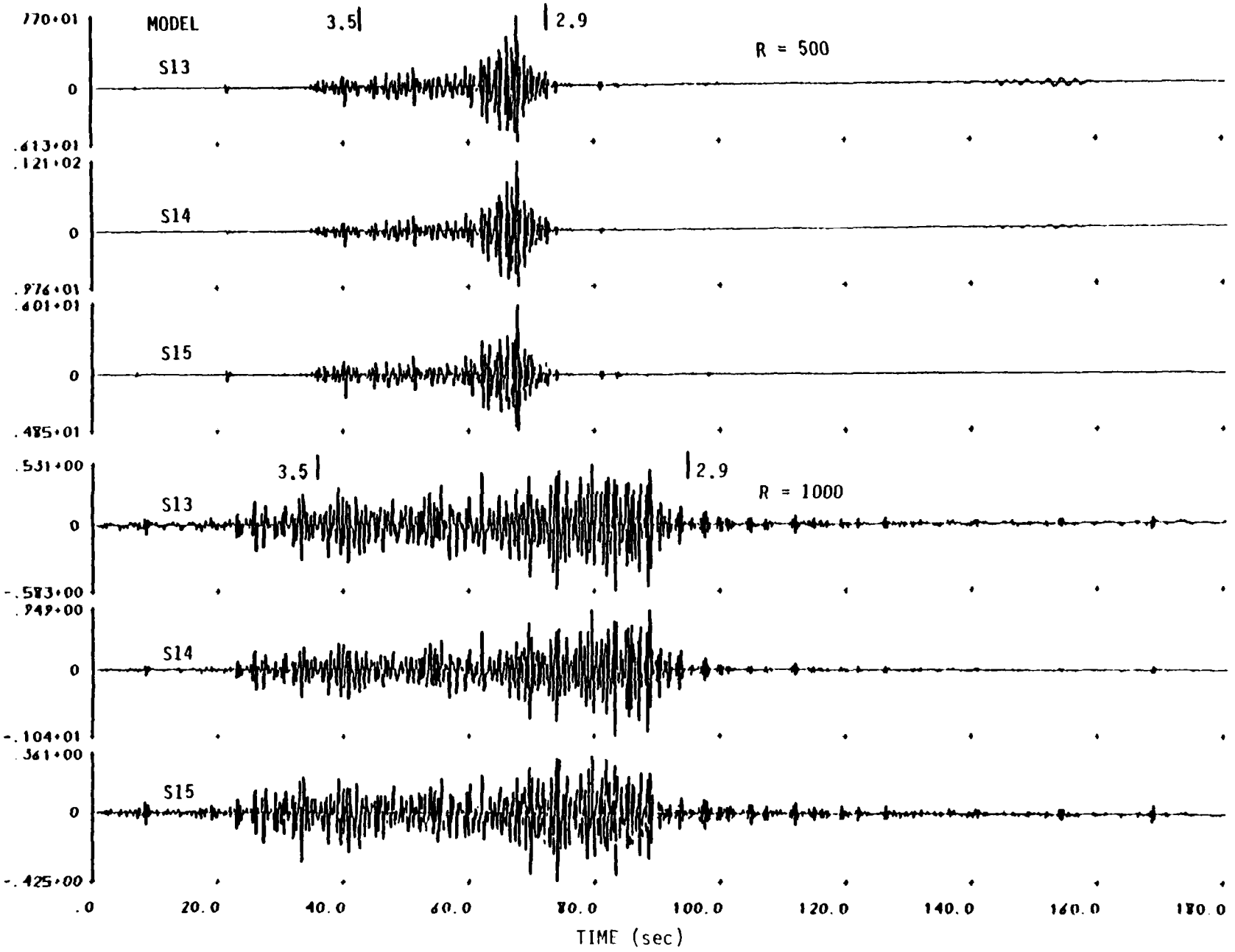

Figure 13. Synthetic seismograms for the SALMON source and three crustal models.

TABLE 5

Lg AMPLITUDES FROM SYNTHETIC SEISMOGRAMS

Model	R=500 Lg (nm)	R=1000 Lg (nm)	γ_{syn}
S11	6950	1710	0.18
S12	5310	1340	0.18
S13	3070	570	0.25
S14	3730	790	0.22
S15	2460	343	0.31
S16	3480	833	0.19

3.3.3 A Modified Velocity Model

The Q inversions described by Mitchell (1980) were done with the McEvilly (1964) model which best fit his Rayleigh wave data. We have modified this model by lowering the velocities in the top 4.1 kilometers, but this is a region that is poorly resolved. McEvilly (1964) also gives a model which gives the best simultaneous fit to both Rayleigh and Love wave data. This model differs from that in Table 3 (except for the top 4 layers that we have introduced) by having the shear velocity at the base of the crust be 3.94 km/sec, rather than 3.67 km/sec. This has the effect of introducing some gradient at the base of the crust, rather than having a 27 km section of nearly constant shear velocity.

A crustal model with the frequency-dependent Q of S14 and β = 3.94 km/sec between 20 and 38 km depths, is called S16. Seismograms for this model are plotted in Figure 14 and the amplitudes are listed in Table 5.

The seismograms for this model have the energy more evenly spread through the Lg time window, especially at R = 500 km. They also have a γ more like that of S11 and S12, while the amplitudes are much smaller.

3.4 CONCLUSIONS

In our previous report (Bache *et al.*, 1980), it was suggested that frequency independent Q models are not sufficient to describe the attenuation characteristics of the observed Lg from SALMON. In this section we have examined the characteristics of synthetic Lg in EUS models with frequency dependent Q. Mitchell (1980) has suggested intrinsic attenuation with frequency power laws. For models suggested from inversion studies, synthetic Lg were found to have the same deficiencies as those with frequency independent Q. Modifying the properties of the near surface layering gave some improvement, but the result synthetic seismograms are not more realistic than those found for frequency independent Q models.

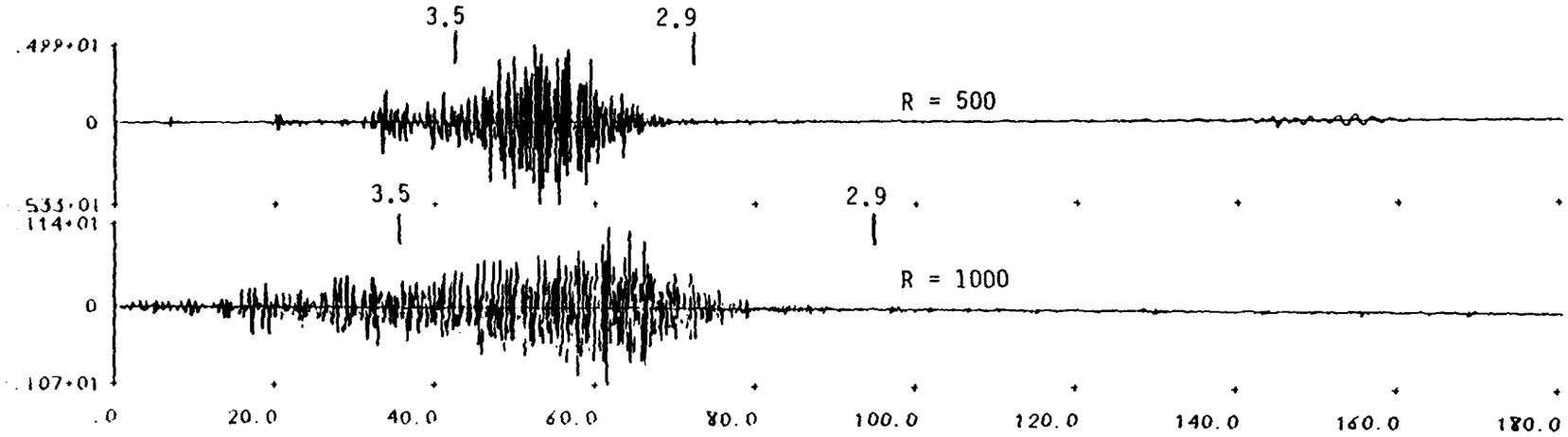

Figure 14. Synthetic seismograms for the model S16 described in the text. The source is that for SALMON.

The major deficiencies in the synthetic Lg - 1) too little late arriving energy, 2) wrong spectra above 3 Hz, and 3) wrong attenuation rate of peak amplitudes with distance - suggest that simple attenuation mechanisms in plane layered earth models is not realistic for the high frequencies and large distances considered here. The presence of late arriving energy and lack of a fundamental mode in the short period data suggests that scattering is probably an important contribution to the attenuation process. Frequency dependent Q models do not appear to approximate the effects of such mechanisms very well. Several models for the scattering of high frequencies have been suggested (Chernov, 1960; Aki 1969; Dainty and Toksoz, 1977) and these models are being applied to the study of near-regional seismic codas (Aki and Chouet, 1975, for example). Such models of scattered wave propagation might be useful to regional studies, but at this time it is not clear just now they may be applied to synthetic seismogram computations.

IV. SYNTHETIC Lg SEISMOGRAMS IN DIFFERENT TECTONIC PROVINCES

4.1 INTRODUCTION

An important feature of Lg is that its characteristics are observed to vary widely from one tectonic province to another. The fact that Lg does not propagate on paths that cross the deep ocean was noted in the earliest papers describing this phase (Press and Ewing, 1952). Recent work has concluded that the Lg phase is also absent for paths crossing the Tibetan Plateau (Ruzaiken, et al., 1977), and the Black Sea (Antonova, et al., 1978).

Several explanations for the relative efficiency of propagation of Lg in different tectonic provinces have been proposed. There are basically three reasons why the Lg may be absent. These are:

1. The waveguide for Lg is absent.
2. The phase is disrupted by passage across a sharp lateral discontinuity.
3. The phase is strongly attenuated.

In this section we study the relative excitation of Lg in three different tectonic regions using a straightforward technique. The regions are the deep ocean, the Tibetan Plateau and the stable platform area of the central and eastern United States. The technique is to compute Lg seismograms in standard models for each region and compare them. By standard models we mean laterally homogeneous, plane-layered crustal models with frequency-independent Q. We found in Section III that the introduction of frequency-dependent Q did not change the basic character of the synthetic Lg seismograms in terms of the time of Lg onset or its duration.

With the straightforward technique we are using we can investigate the first and third listed reasons for the failure of Lg to propagate in certain regions. An analysis of the effect of lateral boundaries would require techniques like Gregerson and Alsop (1974) developed for propagating the Lg phase across such boundaries.

Synthetic seismograms for the oceanic, Tibetan Plateau, and central and eastern United States models are presented in Sections 4.2, 4.3 and 4.4, respectively. These seismograms are compared in Section 4.5 where our conclusions are summarized.

4.2 Lg IN AN OCEANIC CRUST

An often mentioned characteristic of Lg is that it is not observed when the travel path includes a section that crosses a deep ocean basin (Press and Ewing, 1952). Several reasons have been proposed to explain the disappearance of Lg on such paths. Some have suggested that the crustal waveguide in which the Lg energy is trapped is disrupted by the ocean-continent margin (Ewing, Jardetzky and Press, 1957). Knopoff, et al. (1979) suggest that Lg is scattered by strong lateral variations in the relatively thick low velocity sediments at the ocean bottom or is rapidly attenuated by the low Q which is characteristic of the oceanic crust.

In this section we look at the propagation of Lg in oceanic structures in a straightforward way. We simply compute multimode seismograms for a good model for the oceanic crust and see if Lg is present. The model is plane-layered and laterally homogeneous and has a frequency-independent Q. Models of this kind for the continental crust lead to seismograms with an obvious Lg phase, as is demonstrated elsewhere in this report.

The oceanic crustal model is listed in Table 6. This model is a smoothed version of the model FF2 obtained by Spudich and Orcutt (1980) by fitting synthetic seismograms to the data from a refraction line east of Guadaloupe Island off the coast of Baja California. We also modified the model by adding a higher velocity layer for the halfspace below a depth of 19 km.

There are 46 modes for this model between 1 and 5 Hertz. They are plotted in Figure 15. The first thing to be noticed is that there is no clustering of group velocity stationary phases near 3.5 km/sec, as is prominently seen on similar plots for continental crustal structures. The only prominent group velocity plateaus are near 1.0 km/sec and 0.25 km/sec.

TABLE 6

OCEANIC CRUSTAL MODEL FF2 (SPUDICH AND ORCUTT, 1980)

Depth (km)	Thickness (km)	α (km/sec)	β (km/sec)	ρ (km/sec)	Q_α	Q_β
3.40	3.40	1.463	0	1.0	∞	0
3.57	0.17	1.58	0.25	1.5	200	100
4.00	0.43	4.8	2.45	2.07	450	100
4.54	0.54	6.0	3.25	2.53	450	100
5.12	0.58	6.3	3.76	2.64	450	225
8.64	3.52	6.95	3.74	2.89	450	225
9.33	0.69	7.38	4.3	3.05	450	225
19.0	9.67	7.80	4.5	3.20	450	225
		8.20	4.62	3.35	450	225

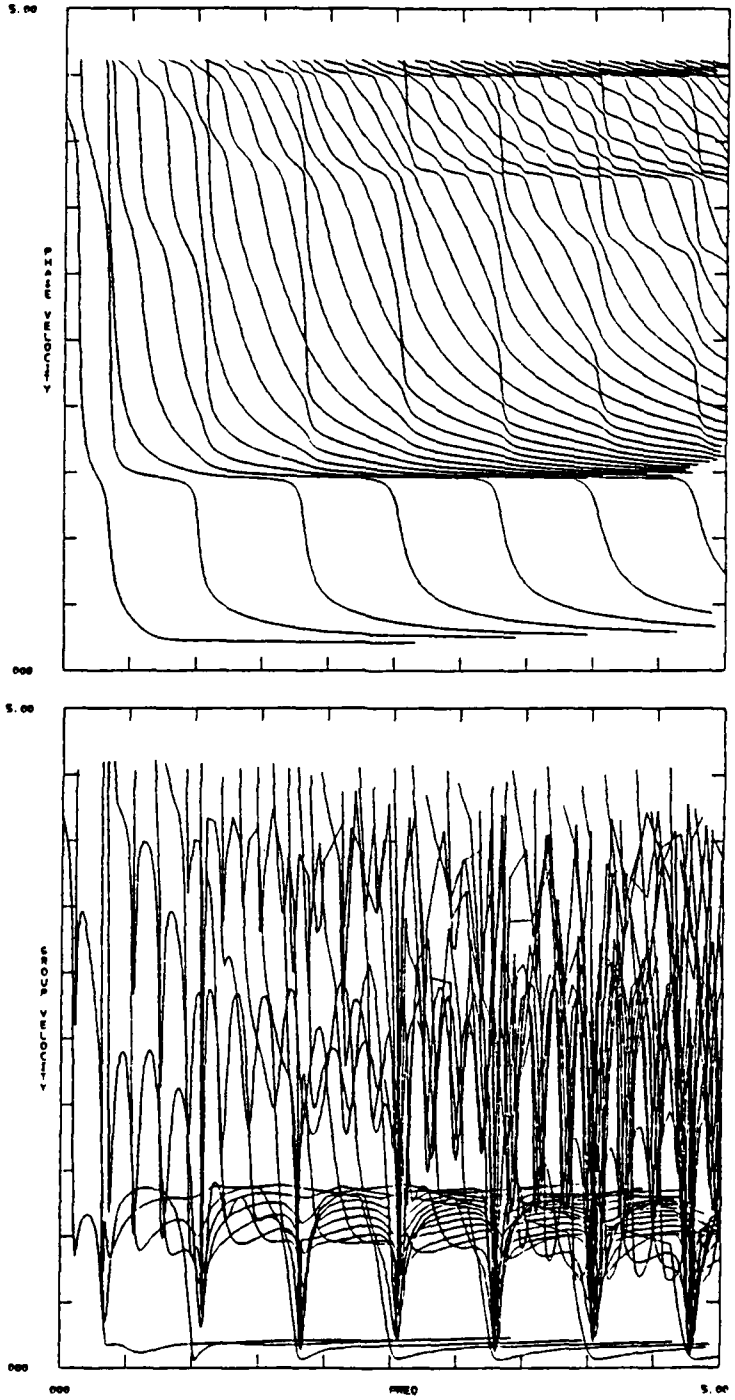

Figure 15. Phase and group velocity dispersion for the oceanic crust model of Table 6.

Synthetic seismograms were computed in the oceanic model for a strike-slip double-couple source. The source time history was a step with a moment of 10^{25} dyne-cm. The synthetics were computed for depths of 8.4 km (5 km below the ocean bottom), 10.9 km and 12.4 km. The range was 200 km. We also computed a synthetic at R = 100 km for the shallowest source. These synthetic seismograms are shown in Figure 16.

The seismograms in Figure 16 have the energy distributed rather evenly over the entire group velocity interval from 4.62 km/sec (the cutoff velocity) to less than 2.0 km/sec. There is no sharp arrival of energy near 3.5 km/sec which characterizes Lg. We will have more to say about these seismograms in Section 4.5 where we compare synthetics from several crustal models.

4.3 Lg IN THE TIBETAN PLATEAU

The Tibetan Plateau is an especially interesting tectonic region for many reasons, but the one that concerns us is that Lg is not observed for paths crossing this region. This is pointed out by Ruzaikin, et al. (1977), who also summarize several arguments for why the Lg is absent.

These fall into two classes:

1. The waveguide for Lg is disrupted at the margins of the Plateau, or does not exist there at all.

2. The attenuation in the crust is very high beneath Tibet.

To investigate Lg propagation in this region, we compute theoretical seismograms for two models for the Tibetan Plateau. Both are taken from Chun and Yoshii (1977) and are listed in Table 7. The first model (TP1) has been slightly modified by adding 1 km of lower velocity material at the surface.

The two Tibetan Plateau models in Table 7 both have a 68 km crust and the same halfspace representing the upper mantle. The

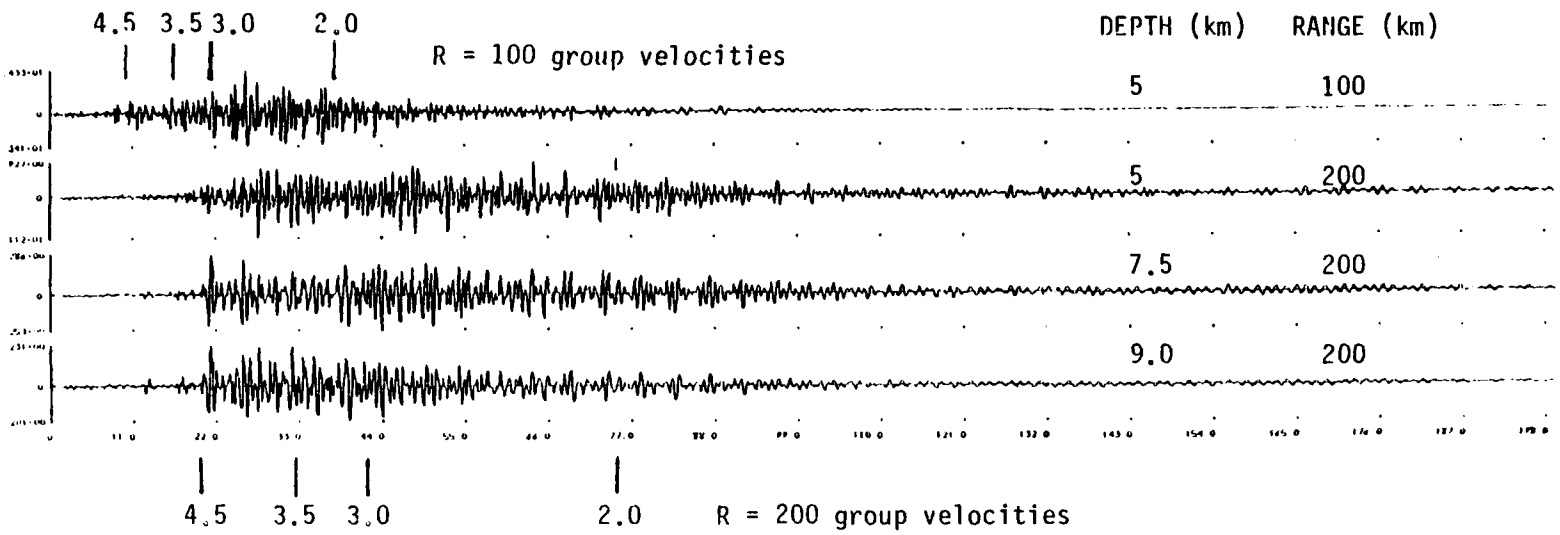

Figure 16. Synthetic seismograms are shown for several depths and ranges in the oceanic crustal model of Table 6. The source is a strike-slip double-couple with a step function time history with $M_0 = 10^{25}$ dyne-cm. The WWSSN short period seismometer response is included. The source depth is measured from the ocean bottom.

TABLE 7

TIBETAN PLATEAU MODELS FROM CHUN AND YOSHII (1977)

Layer	Depth (km)	Thickness (km)	α (km/sec)	β (km/sec)	ρ (gm/cm^3)	Q
			Tibetan Plateau Model TP1			
1	1.0	1.0	3.70	2.16	2.10	50
2	3.5	2.5	4.50	2.60	2.40	100
3	13.5	10.0	5.98	3.45	2.80	250
4	38.0	24.5	5.98	3.45	2.80	1200
5	68.0	30.0	6.30	3.64	2.90	2000
6			7.70	4.45	3.30	3000
			Tibetan Plateau Model TP3			
1	1.0	1.0	4.50	2.60	2.40	40
2	3.5	2.50	4.50	2.60	2.40	150
3	28.0	24.50	5.98	3.42	2.80	200
4	38.0	10.0	5.80	3.35	2.75	200
5	68.0	30.0	6.30	3.64	2.90	1000
6			7.70	4.45	3.30	2000

main difference is that TP3 has a low velocity layer in the mid-crust. Chun and Yoshii (1977) prefer models with this feature. The TP3 model also has much lower Q than TP1.

The phase and group velocity dispersion for the two models are plotted in Figure 17. The number of modes required to span a particular frequency range is roughly proportional to the travel time from the surface to the top of the halfspace. For these models we computed 50 modes, which is a complete set for 0 to 2 Hertz. Recall that the oceanic crust required only 46 modes for 0 to 5 Hertz.

Both models have a prominent band of group velocity minima between 2.9 and 3.5 km/sec. This is precisely the characteristic that we associate with a prominent Lg phase.

Synthetic seismograms for the two models are shown in Figure 18. The same source used for the oceanic model synthetics in Section 3.2 was used. This is a strike-slip double-couple with a step function time history with a moment of 10^{25} dyne-cm. The seismograms for the two models are quite similar. The main difference is in the amplitude, with the lower Q TP3 having amplitudes that are about a factor of 5 larger than those for TP1, and a corresponding shift to lower frequencies.

The synthetic seismograms have an Lg arrival that becomes more prominent with increasing depth. The best Lg is for the 50 km source depth. At the shallower depths, the Lg is rather emergent, but reaches its largest amplitude before 3.4 km/sec. Seismograms in these models will be compared to those from other models in Section 4.5

4.4 Lg IN A MODEL FOR THE CENTRAL U.S.

4.4.1 Introduction

In our semi-annual report (Bache et al., 1980) we were concerned with parametric variations of a model intended to represent the eastern U.S. The variations were primarily in the Q

Model TP1 Model TP3

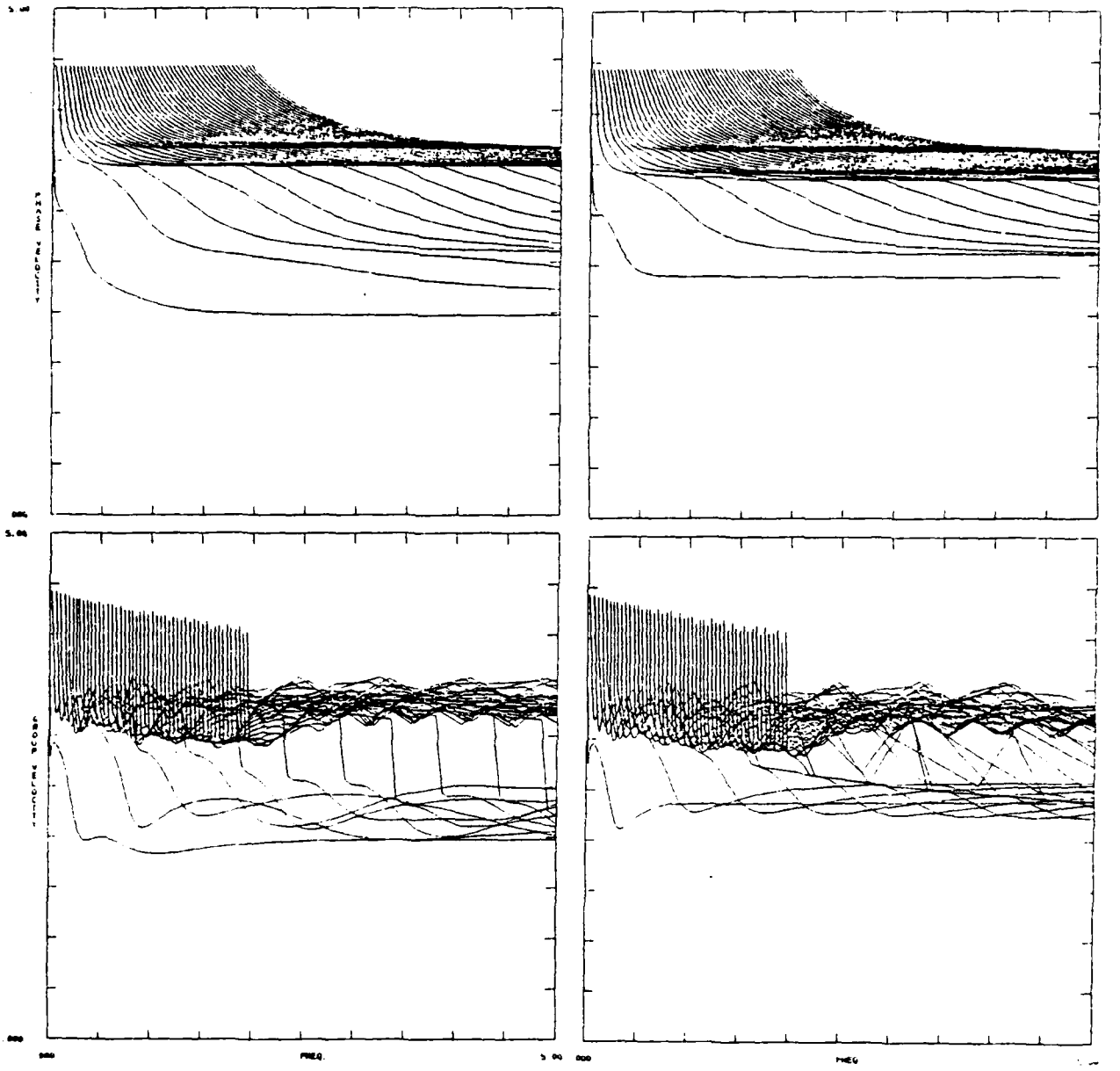

Figure 17. Phase and group velocity dispersion for fifty modes in two Tibetan Plateau crustal models.

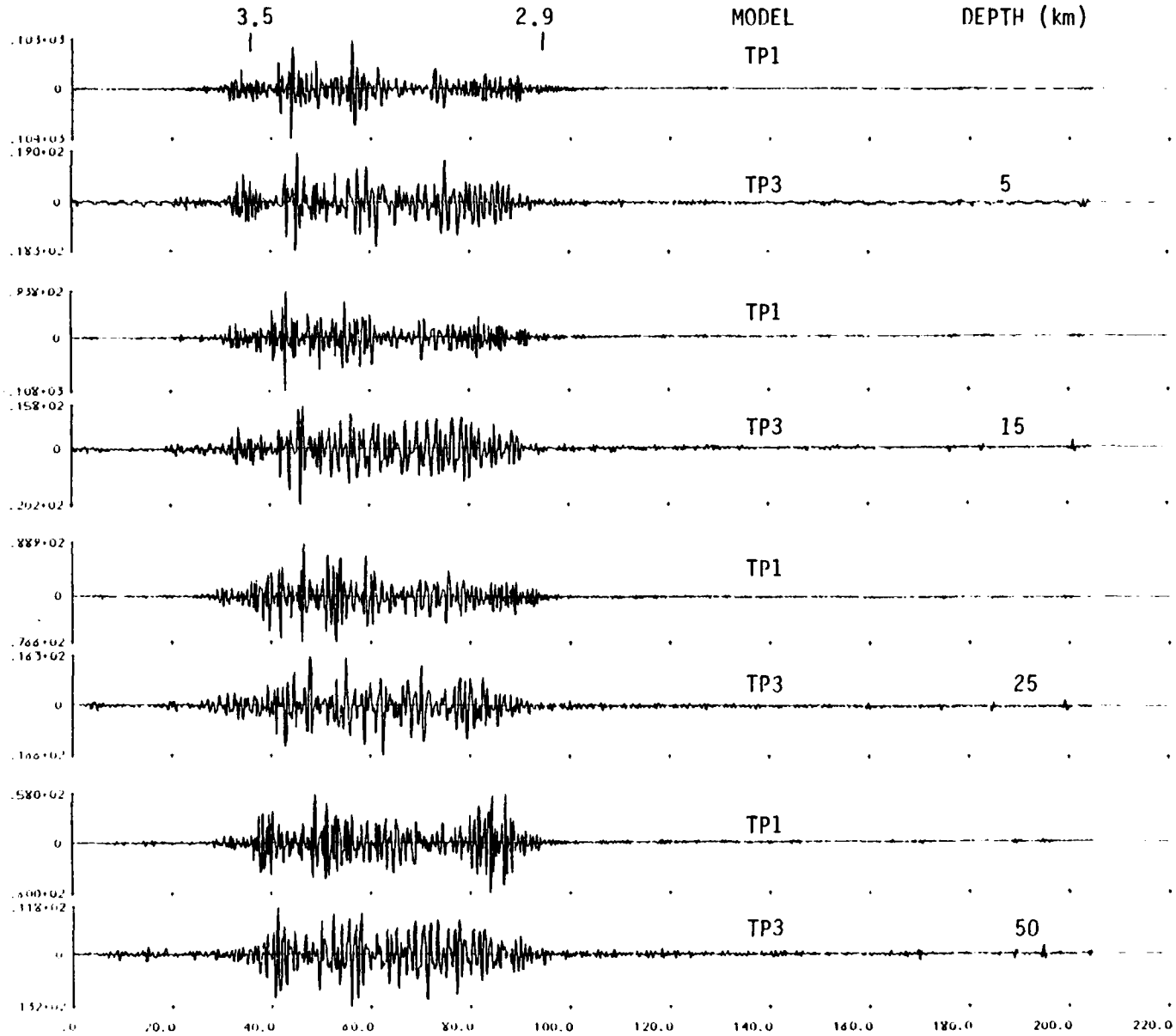

Figure 18. Synthetic seismograms are shown (R = 100 km) for the two Tibetan Plateau crustal models of Table 7. The source is a strike-slip double-couple ($M_0 = 10^{25}$ dyne-cm).

structure (only frequency-independent Q was considered), but some velocity structure variations were also considered. However, all the models studied had the same crustal thickness (34 km) and halfspace representing the upper mantle. There are other velocity models that may be more appropriate for the eastern and central U.S., and in this section we will examine the Lg predicted for such a model. Comparing among different crustal models also gives some idea of the dependence of Lg on the details of the velocity structure.

4.4.2 Effect of Crustal Thickness

The central U.S. crustal models to be considered are listed in Table 8. First we have the model S1 from our semi-annual report. It has a 34 km crustal thickness. The second model is the model fit to Rayleigh waves by McEvilly (1964). This model has a 38 km crust and has been modified by adding some lower velocity layers in the top 4.1 km. The Q model is nearly the same as that for S1. We will call this model M1. The velocity structure is that used in our discussion of frequency-dependent Q models in Section III.

The phase and group velocity dispersion for these two models are plotted in Figure 19. They are very similar, with the main difference being that the stationary portions of the group velocity curves are at somewhat higher velocities for the McEvilly model than for S1. The band of stationary phases near 3.5 km/sec is associated with Lg. For S1 this band is between 2.75 and 3.5 km/sec. The comparable band for M1 is between 2.9 and 3.6 km/sec. This leads us to expect the Lg to have an earlier arrival time for the latter model.

Synthetic seismograms are compared for the two models in Figure 20. As expected, the M1 model seismograms have an "Lg" arrival at an earlier time than the seismograms for S1. The amplitudes are also interesting. At 5 and 25 km depths the S1 and M1 seismograms have nearly the same maximum amplitudes. However, at the 15 km depth the maximum M1 amplitude is only half that for S1. We will plot the "Lg" amplitudes for these seismograms and two other

TABLE 8

CENTRAL AND EASTERN UNITED STATES CRUSTAL MODELS

Layer	Depth (km)	Thickness (km)	α (km/sec)	β (km/sec)	ρ (gm/cm^3)	Q
(Model S1 Bache, Swanger and Shkoller, 1980)						
1	0.6	0.6	3.70	2.16	2.10	20
2	2.6	2.0	4.55	2.54	2.20	50
3	4.1	1.5	5.6	3.14	2.65	250
4	6.2	2.1	6.1	3.30	2.85	400
5	13.2	7.0	6.3	3.41	2.94	1200
6	19.0	5.8	6.4	3.46	3.00	1500
7	34.0	15.0	6.6	3.59	3.05	2000
8			8.1	4.52	3.35	2000
Anisotropic Central United States Model (McEvilly, 1964)						
1	0.6	0.6	3.70	2.16	2.10	20
2	2.6	2.0	4.55	2.54	2.20	50
3	4.1	1.5	5.60	3.14	2.65	250
4	11.0	6.9	6.10	3.50	2.70	400
5	20.0	9.0	6.40	3.68	2.90	1400
6	38.0	18.0	6.70	3.67	2.90	2000
7	∞	∞	8.15	4.67	3.30	2000

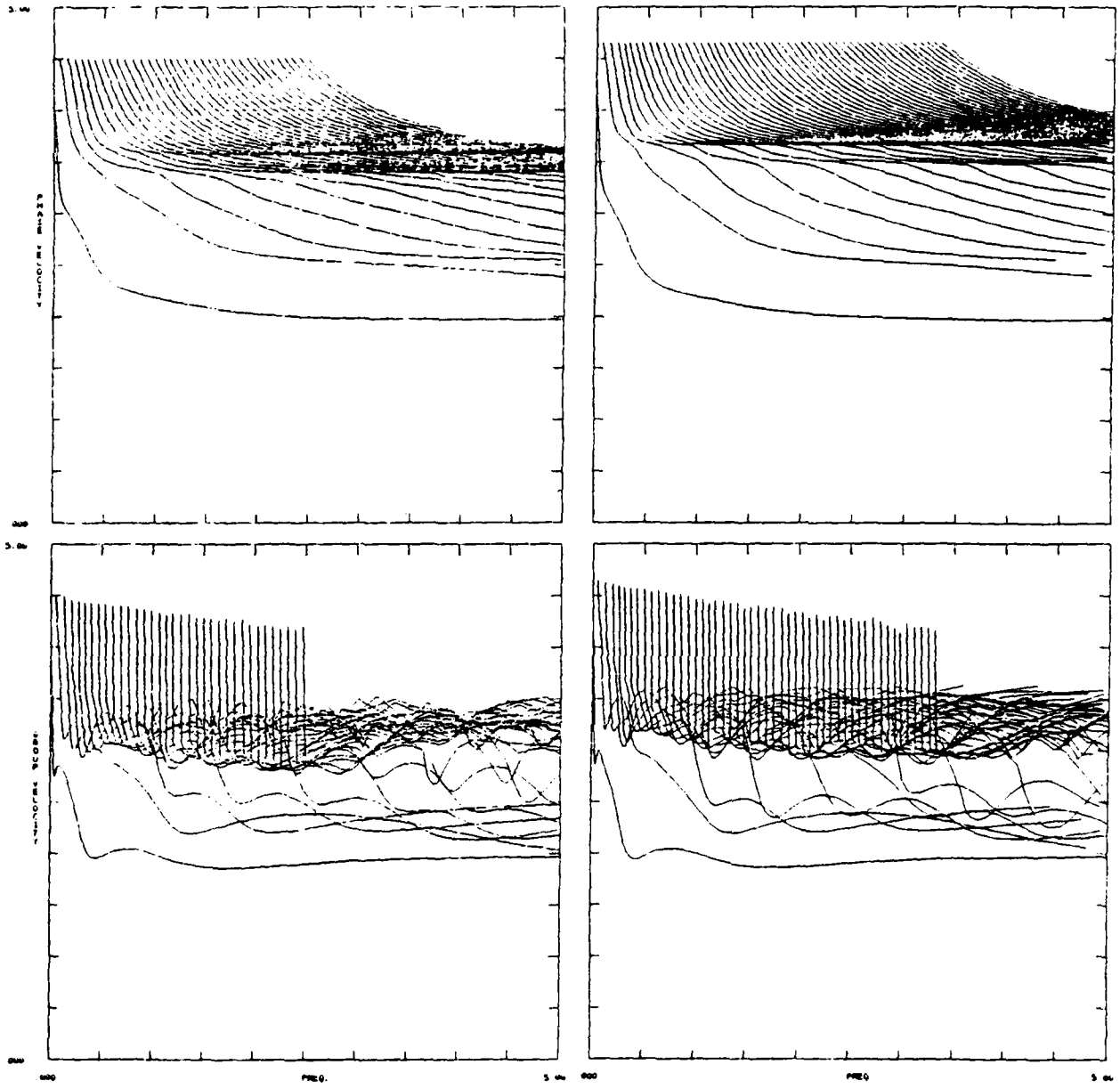

Figure 19. Phase and group velocity dispersion for the central and eastern United States crustal models in Table 8.

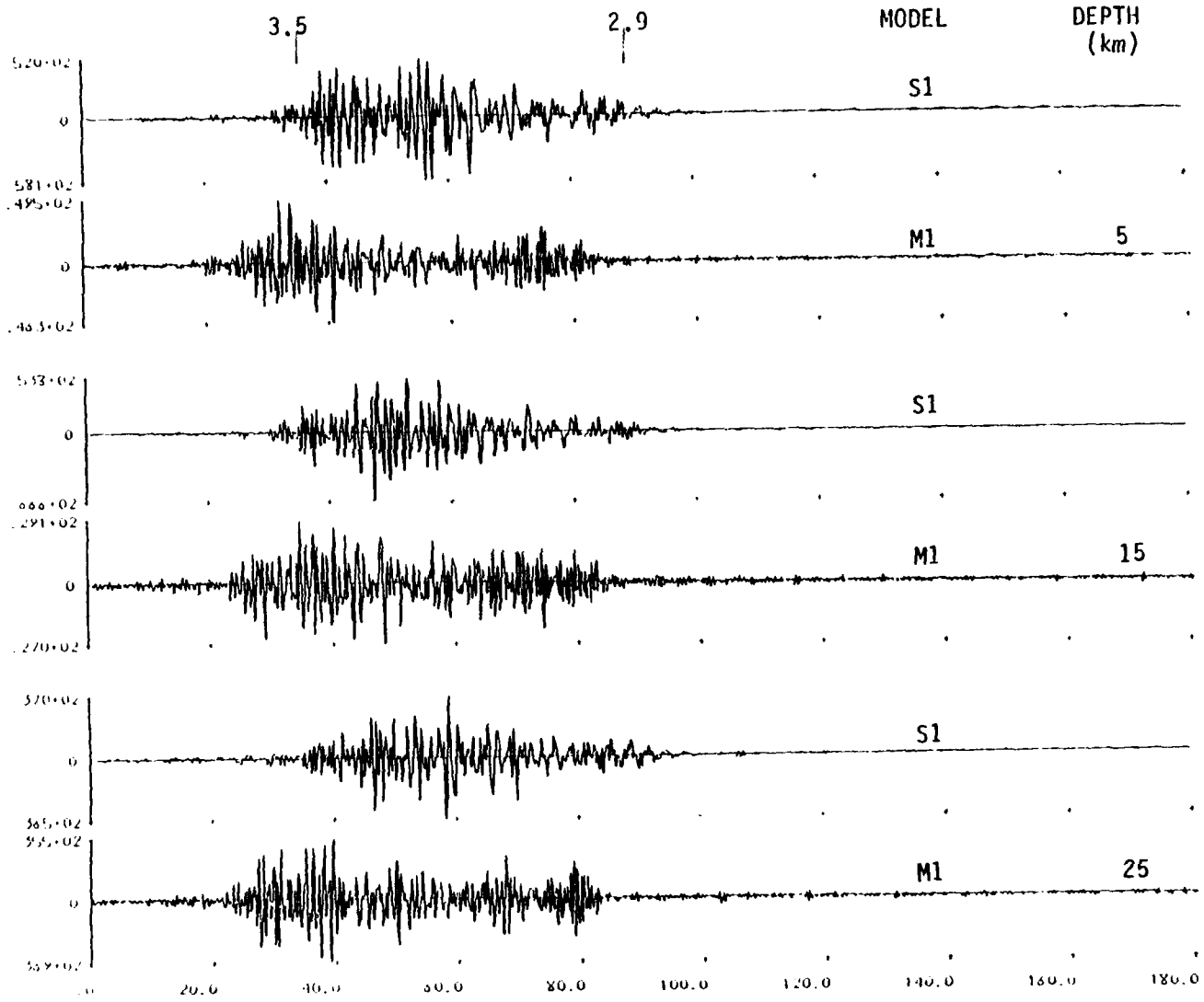

Figure 20. Synthetic seismograms are plotted for three depths in the two crustal models of Table 8. The source is a strike-slip double-couple with $M_0 = 10^{25}$ dyne-cm.

models for the crust in the central and eastern U.S. at the end of this section.

4.4.3 Effect of the Shear Velocity at the Base of the Crust

Another model that is closely related to M1 was discussed in Section 3.3.3. This is the model obtained by McEvilly (1964) to simultaneously fit Love and Rayleigh wave data, rather than Rayleigh wave data which were used to infer M1. For the crust, the only difference is that the 3.67 km/sec layer above the mantle is replaced by a 3.94 km/sec layer. Leaving the Q unchanged from M1, we call the new model M2.

The phase and group velocity dispersion for models M1 and M2 are compared in Figure 21. As was mentioned before, the band of stationary group velocities is between 2.9 and 3.6 km/sec for M1. Increasing the shear velocity at the base of the crust (Model M2) causes this band to move to 3.0 to 3.8 km/sec.

Seismograms for the model M2 are plotted in Figure 22. As expected, the energy is shifted to much earlier group arrival times. Seismograms for the model M2 are plotted in Figure 22. As expected, the energy is shifted to much earlier group arrivals.

The energy distribution displays presented in the previous report (Bache et al., 1980) suggested that nearly all of the energy in the Lg phase is confined to the one or two deepest layers of the crust. This study suggests that there is a direct link between the Lg onset velocity and the shear velocity at the base of the crust. Examination of the synthetic Lg onset times for all crust models used in this study and the previous study suggest an Lg onset velocity between 96 to 98 percent of the shear velocity in the lower crust. The low value (96 percent) was obtained for the Tibetan plateau for which the synthetic Lg is rather emergent and onset time is not well measured.

It appears that when Lg has a sharp onset the velocity at onset may be very useful for inferring the shear velocity of the lower crust over the path of propagation.

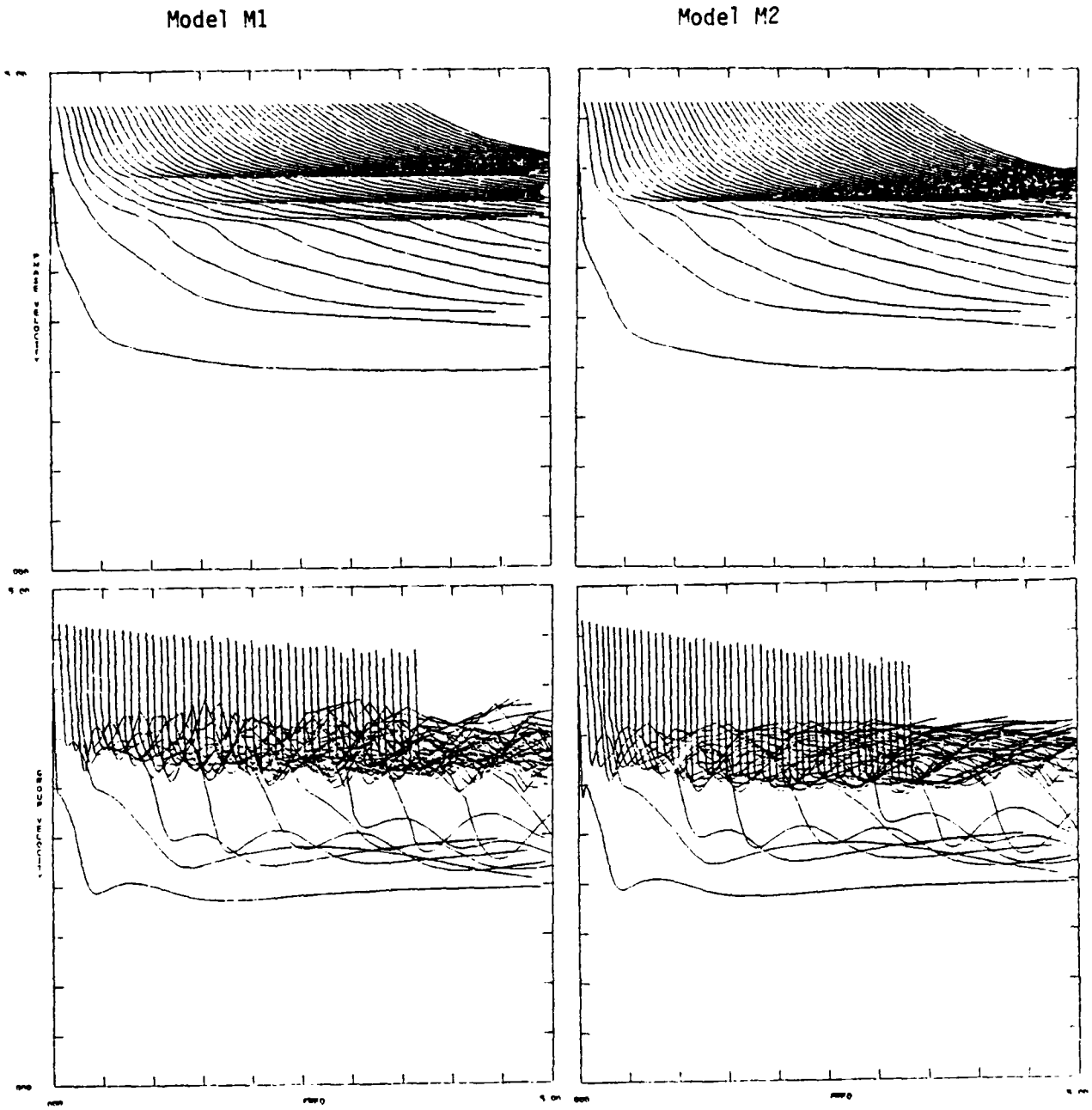

Figure 21. Phase and group velocity dispersion for fifty modes in the models M1 and M2.

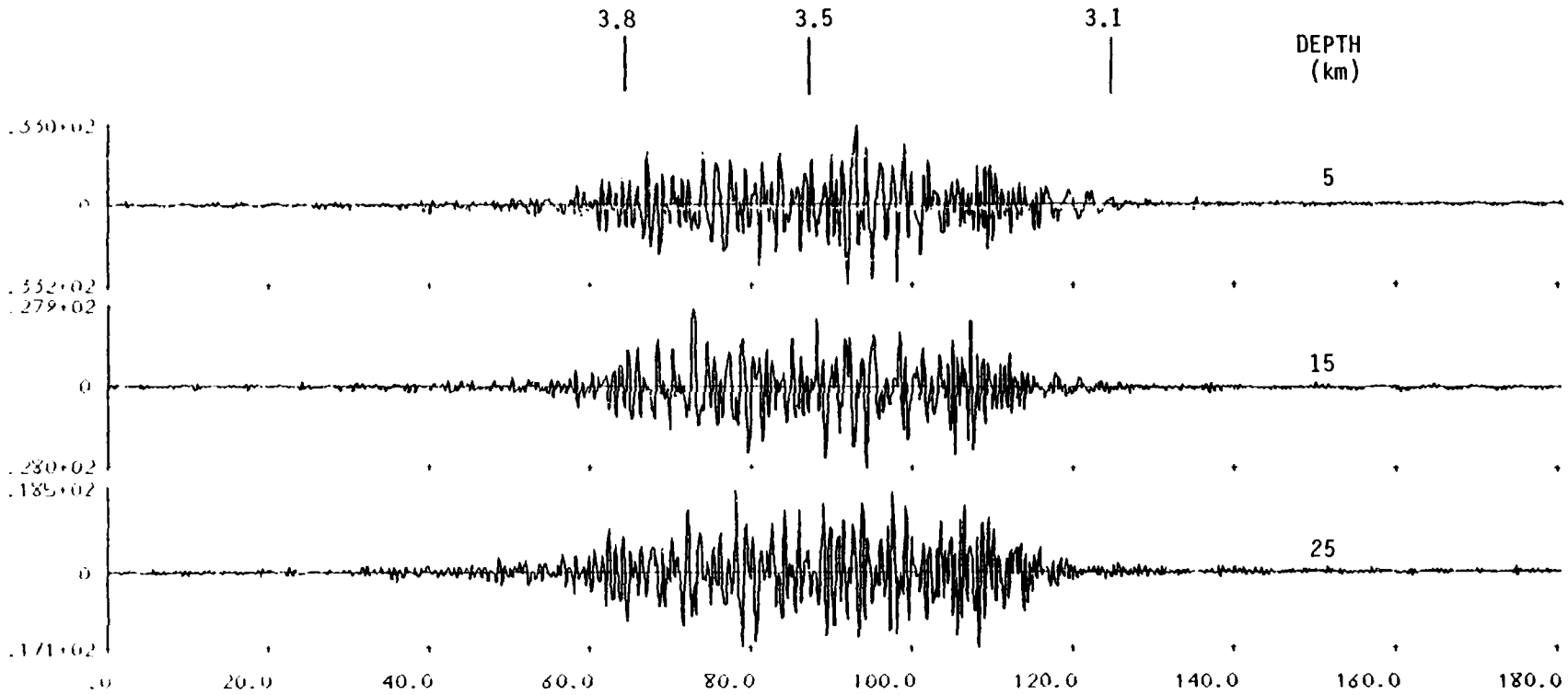

Figure 22. Synthetic seismograms are plotted for the strike-slip double-couple source in the model M2.

4.4.4 Lg in a Central U.S. Model Derived from Body Wave Refraction Data

Our attention has been directed mainly to models derived from observations of surface waves, usually the fundamental mode. We now consider a model suggested by Herrmann and Fischer (1978) for the Central U.S. This model was derived to fit some refraction data from an area near the Illinois-Missouri border. Only arrivals with phase velocities greater than 5.5 km/sec were included, so it is a P wave model. It is interesting to examine the characteristics of Lg in this model.

The "Modified Central U.S." model of Herrmann and Fischer (1978) is listed in Table 9, after altering top 4.1 km to be the same as S1, M1 and M2. The Q model is also consistent with that for these earlier models. The main unique feature of the model in Table 9, which we call C1, is that there is a gradual transition at layer boundaries.

The phase and group velocity dispersion for the model in Table 9 are plotted in Figure 23. Much like M2, the stationary group velocities are clustered at high velocities, in this case in the band between 3.1 and 3.7 km/sec. The synthetic seismograms for this source are plotted in Figure 24. The Lg onset occurs at about 3.75 km/sec.

4.4.5 Amplitudes of the Synthetic Lg for the Central and Eastern U.S.

For each of the four models discussed in this section, we have computed synthetic seismograms with the same source. The Q models are also very much the same for each model; the main differences are in the velocity structure. On each seismogram we measured the Lg amplitude which is taken to be the maximum sustained amplitude within 10 seconds of the 3.5 km/sec group arrival time. These amplitudes are plotted in Figure 25.

4.5 COMPARISON OF SYNTHETIC Lg SEISMOGRAMS IN DIFFERENT CRUSTAL STRUCTURES

We have been computing synthetic Lg seismograms in three distinctly different tectonic regions. In Section 4.2, it was the

TABLE 9

C1 BASE ON THE MODIFIED CENTRAL U.S. MODEL
(HERRMANN AND FISCHER, 1978)

Layer	Depth (km)	Thickness (km)	α (km/sec)	β (km/sec)	ρ (gm/cm^3)	Q
1	0.6	0.6	3.70	2.16	2.10	20
2	2.6	2.0	4.55	2.54	2.20	50
3	4.1	1.5	5.60	3.14	2.65	250
4	7.0	2.9	6.10	3.52	2.56	400
5	8.0	1.0	6.18	3.57	2.59	400
6	9.0	1.0	6.32	3.65	2.65	400
7	18.0	9.0	6.40	3.70	2.68	1400
8	19.0	1.0	6.48	3.74	2.71	1600
9	20.0	1.0	6.62	3.82	2.76	1800
10	38.0	18.0	6.70	3.87	2.79	2000
11	39.0	1.0	7.06	4.08	2.93	1500
12	40.0	1.0	7.79	4.50	3.20	1800
13	∞	∞	8.15	4.71	3.34	2000

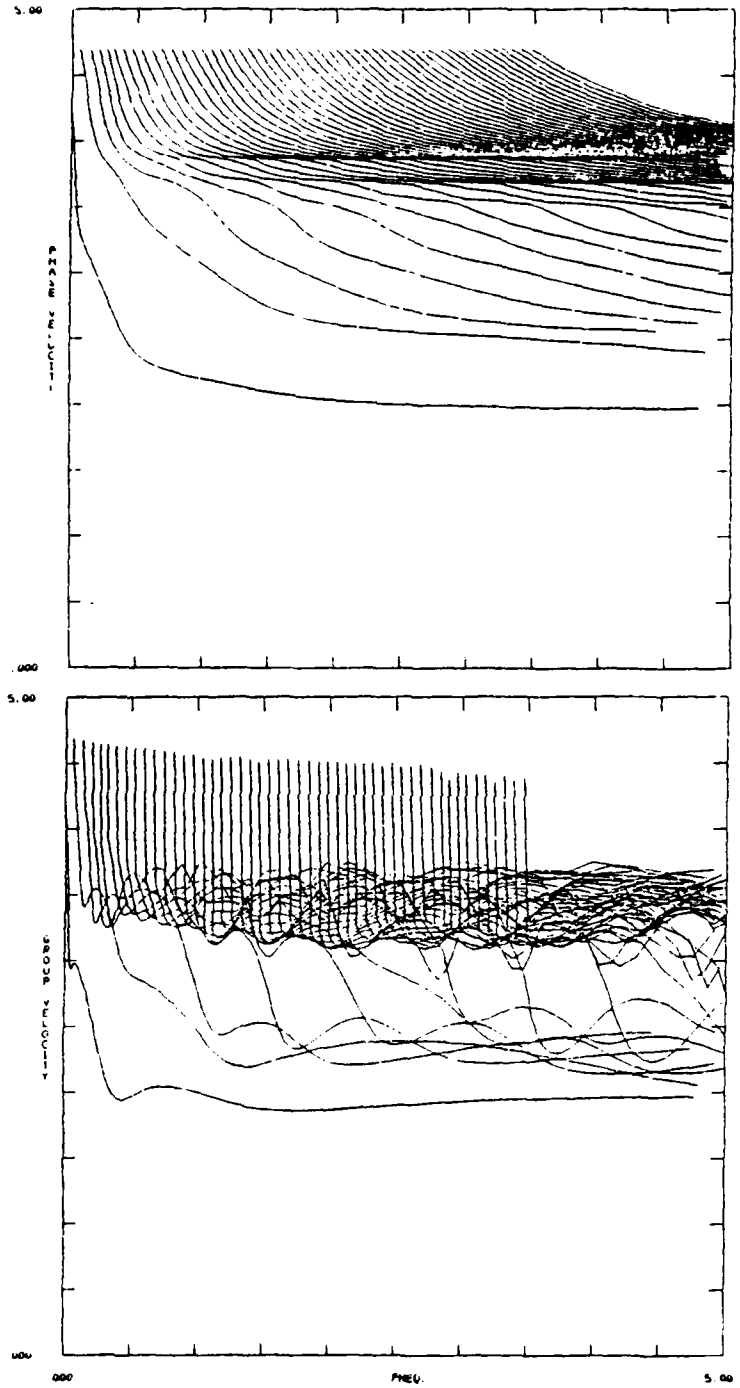

Figure 23. Phase and group velocity dispersion (fifty modes) for the modified central United States model in Table 7.

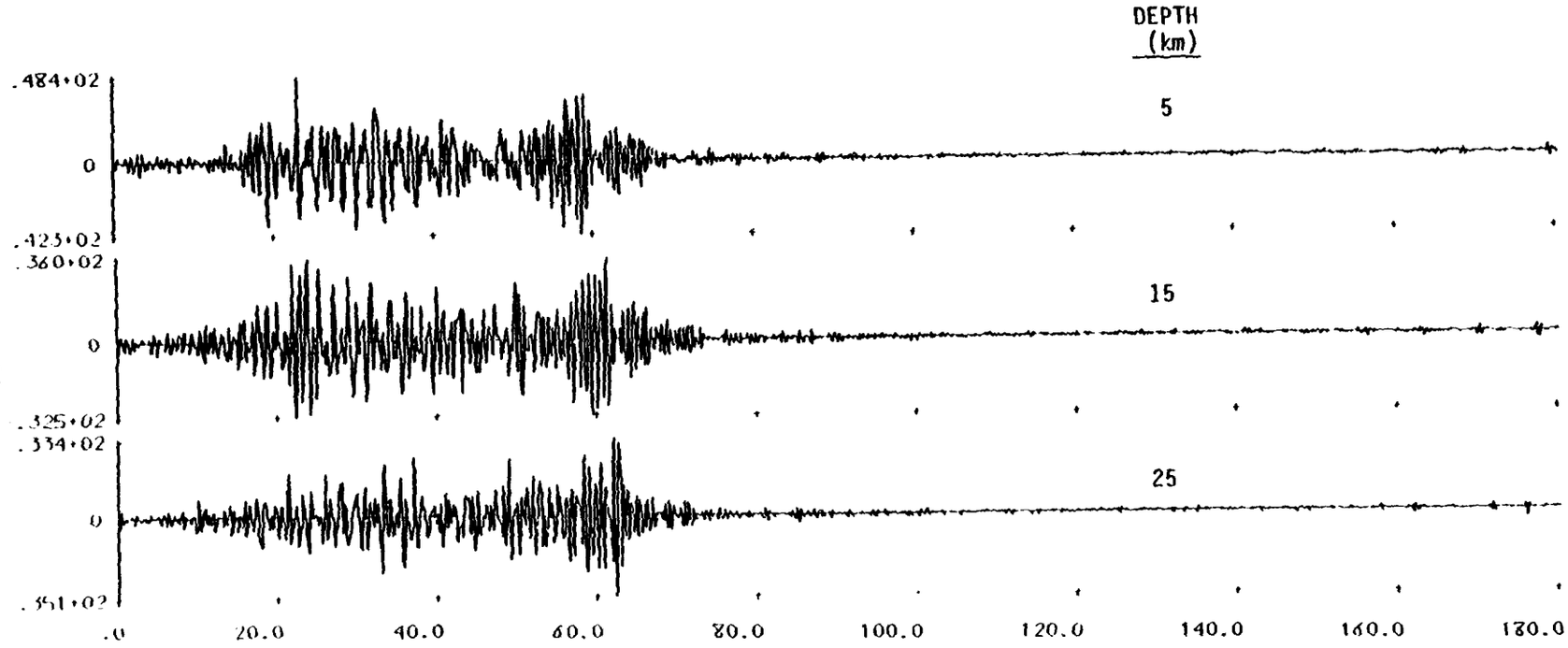

Figure 24. Synthetic seismograms are plotted for three strike-slip double-couple in the model C1.

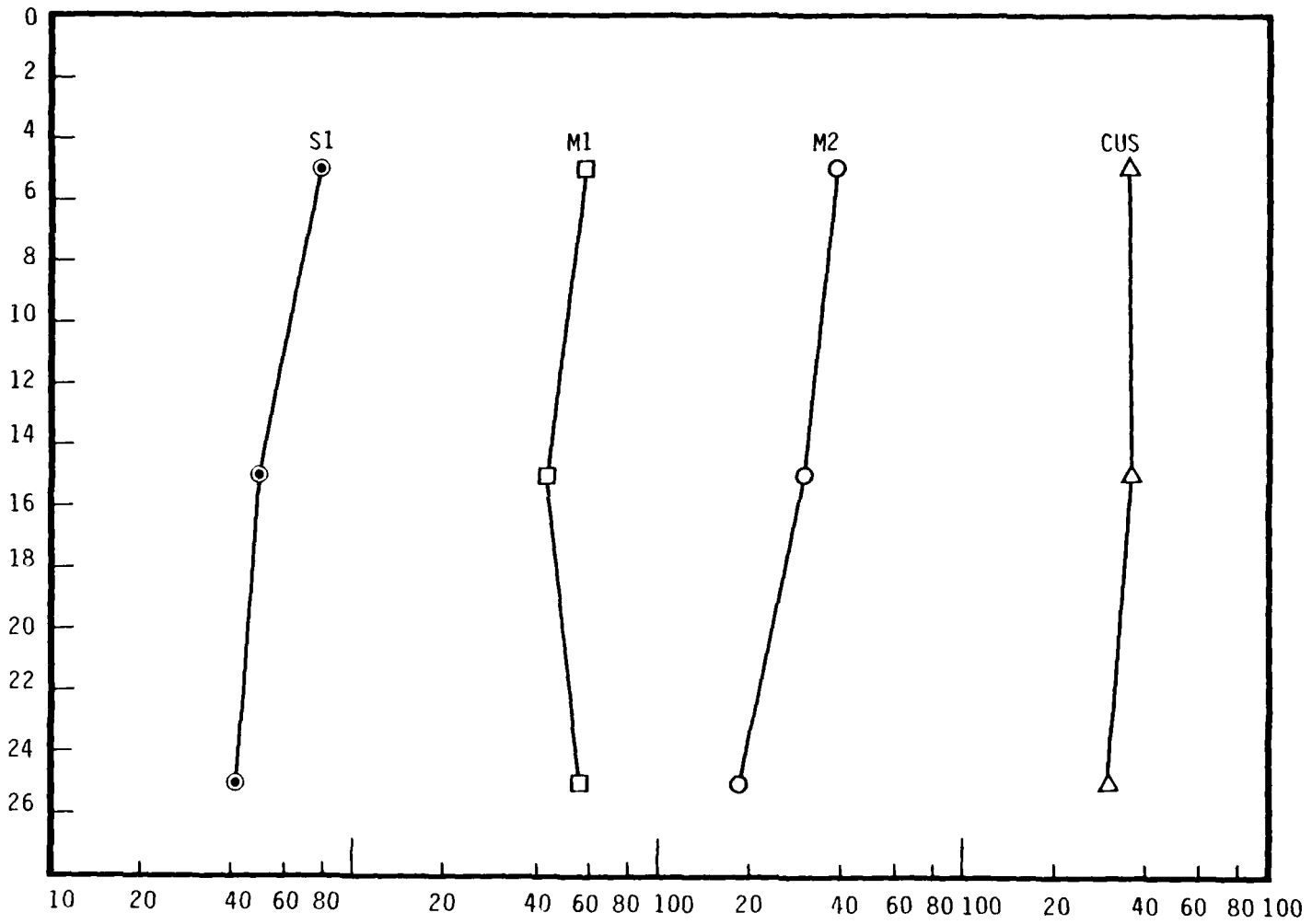

Figure 25. Synthetic Lg amplitudes as a function of source depth for the four crustal models considered.

deep ocean and in Section 4.3 it was the Tibetan Plateau where the crust is very thick. In Section 4.4 we studied several models for the eastern U.S. which represents a stable platform area. In this section we directly compare seismograms for these regions.

The first comparisons are shown in Figure 26. The seismograms were computed for the standard strike-slip double-couple source we have been using, and at two source depths. The oceanic crustal model is very much different from the others in having the energy distributed in a wide group velocity window. These is clearly no waveguide for Lg in the oceanic crust, and this is why it does not propagate there.

The Tibetan Plateau model gives interesting results. For the shallow source it has an Lg phase just as prominent, if not more so, that the stable platform models. However, with a source depth of 5 km, the Lg phase nearly disappears in the Tibetan Plateau model. We need to compare the seismograms at greater ranges to draw firm conclusions about the TP3 model as a propagator of Lg.

In Figure 27, we compare synthetic seismograms at three source depths in five crustal models. These are the Tibetan Plateau Model TP3 and four different models representing the eastern and central U.S. The source is a strike-slip double-couple with a step-time history with moment 10^{25} dyne-cm. The models are described in Sections 4.3 and 4.4.

In summary, Lg fails to propagate in oceanic structure because there is no waveguide for the phase quite like that in continental crusts. For the particular crustal models used for our computations, energy of the multi-mode Rayleigh waves are distributed over a much wider group velocity window than is normally associated with Lg. The large dispersion also results in considerably lower amplitudes in the group velocity window of interest than those in continental crusts. The major structural feature lacking in the oceanic model used is a distinct Moho. There are particular

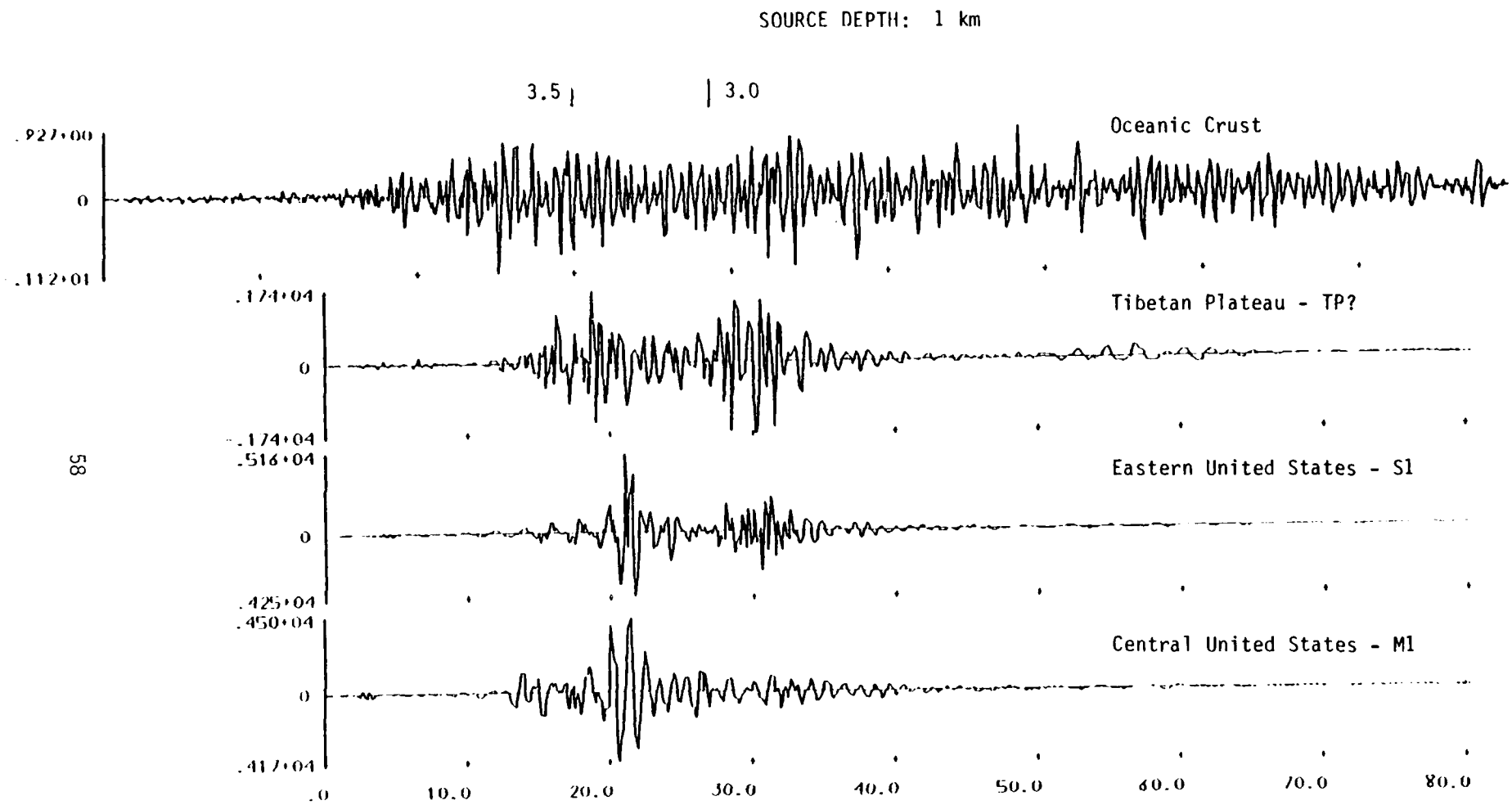

Figure 26. Comparison of synthetic seismograms (R = 200 km) for four crustal models.

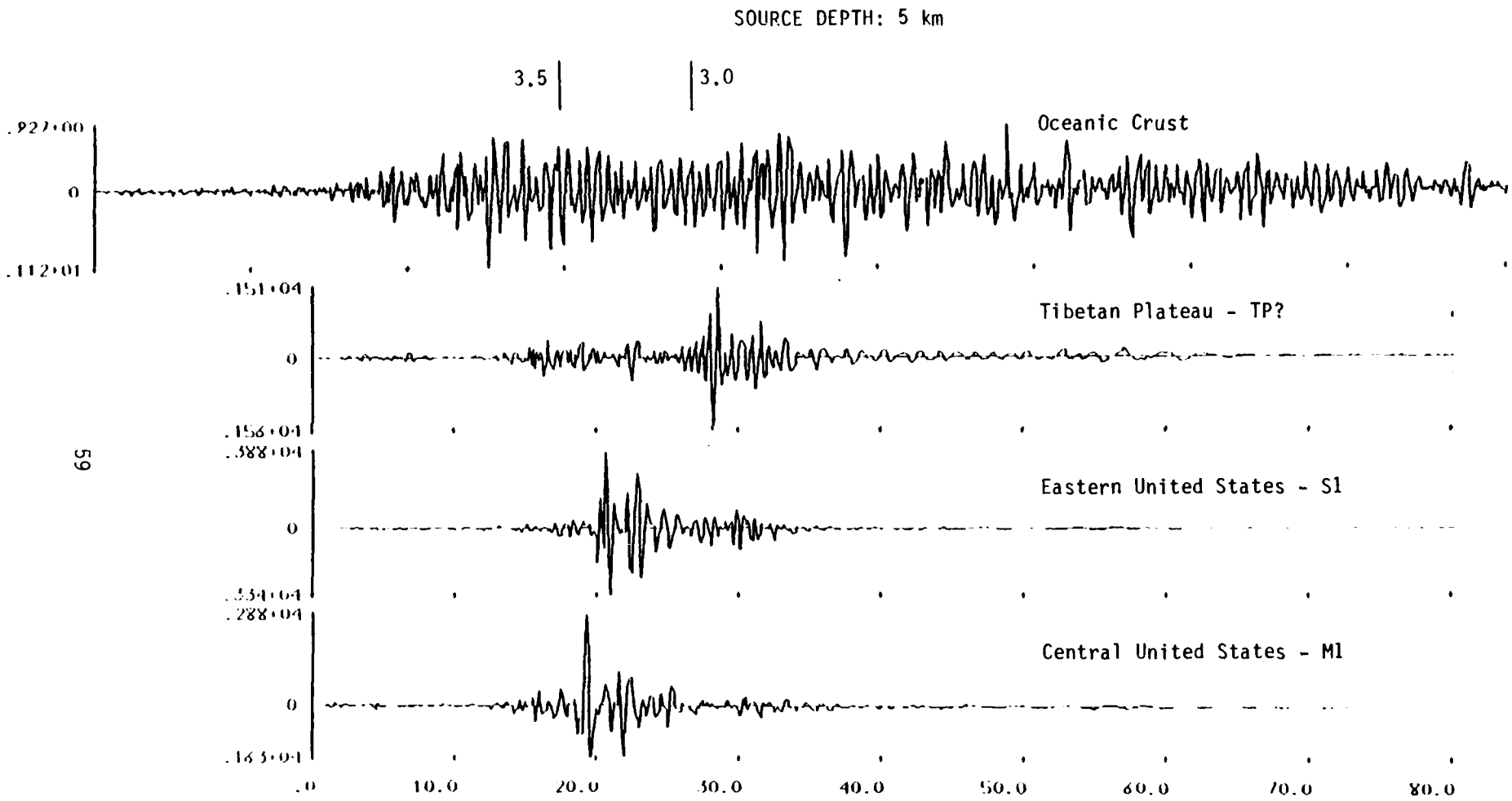

Figure 26. (continued)

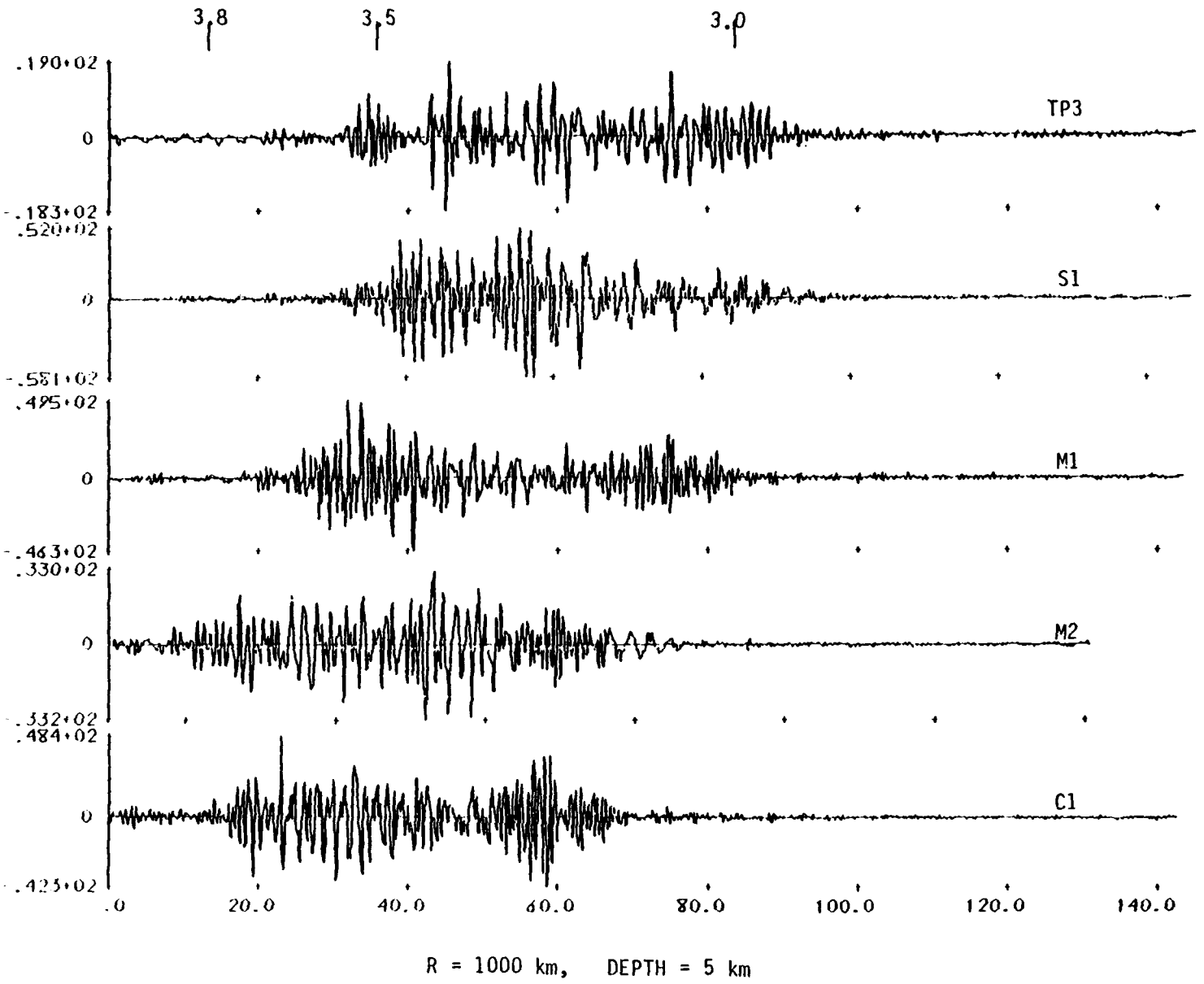

Figure 27. Synthetic seismograms are compared at three source depths in a Tibetan Plateau crustal model (TP3) and four models for the central and eastern United States.

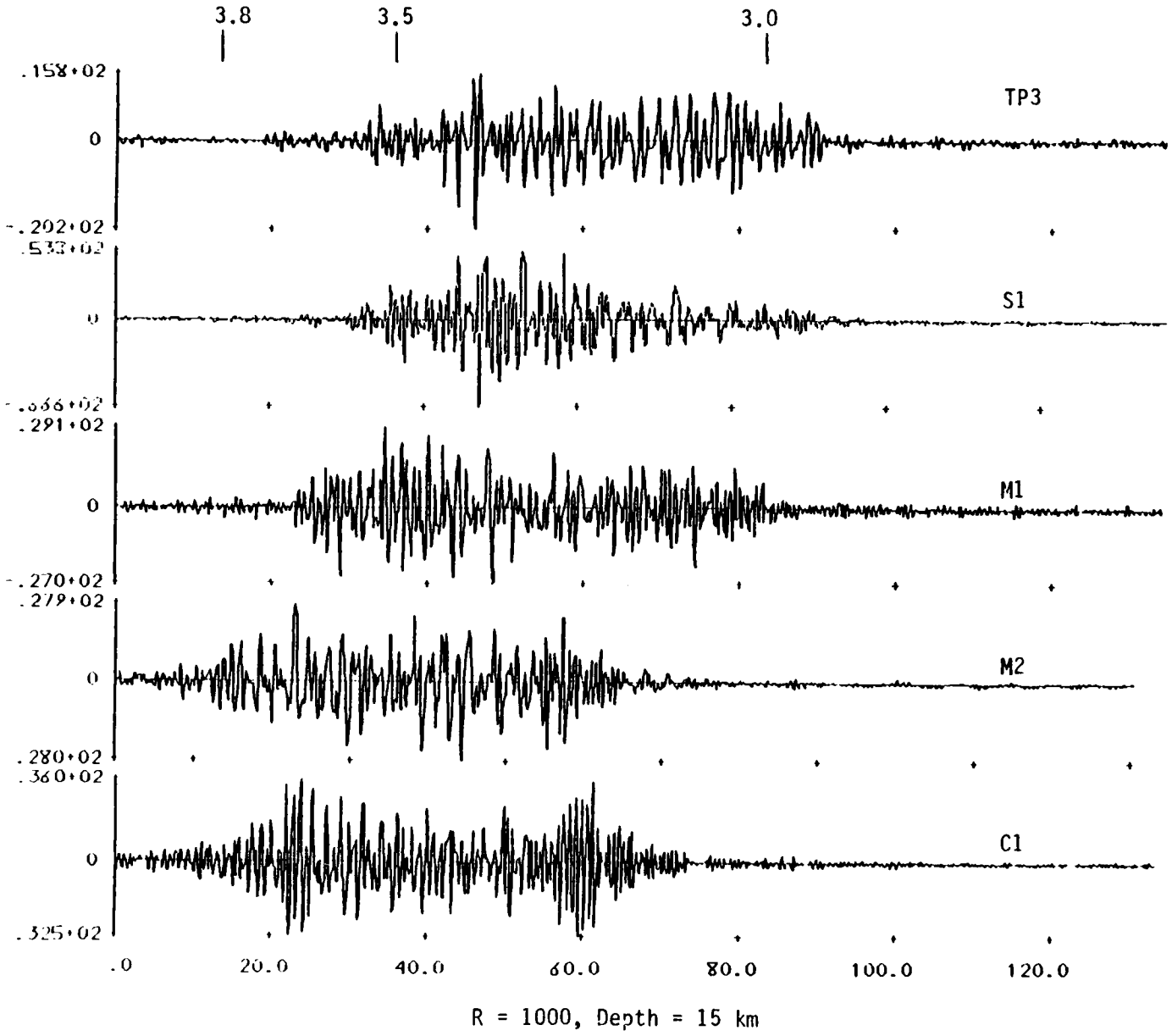

Figure 27. (continued)

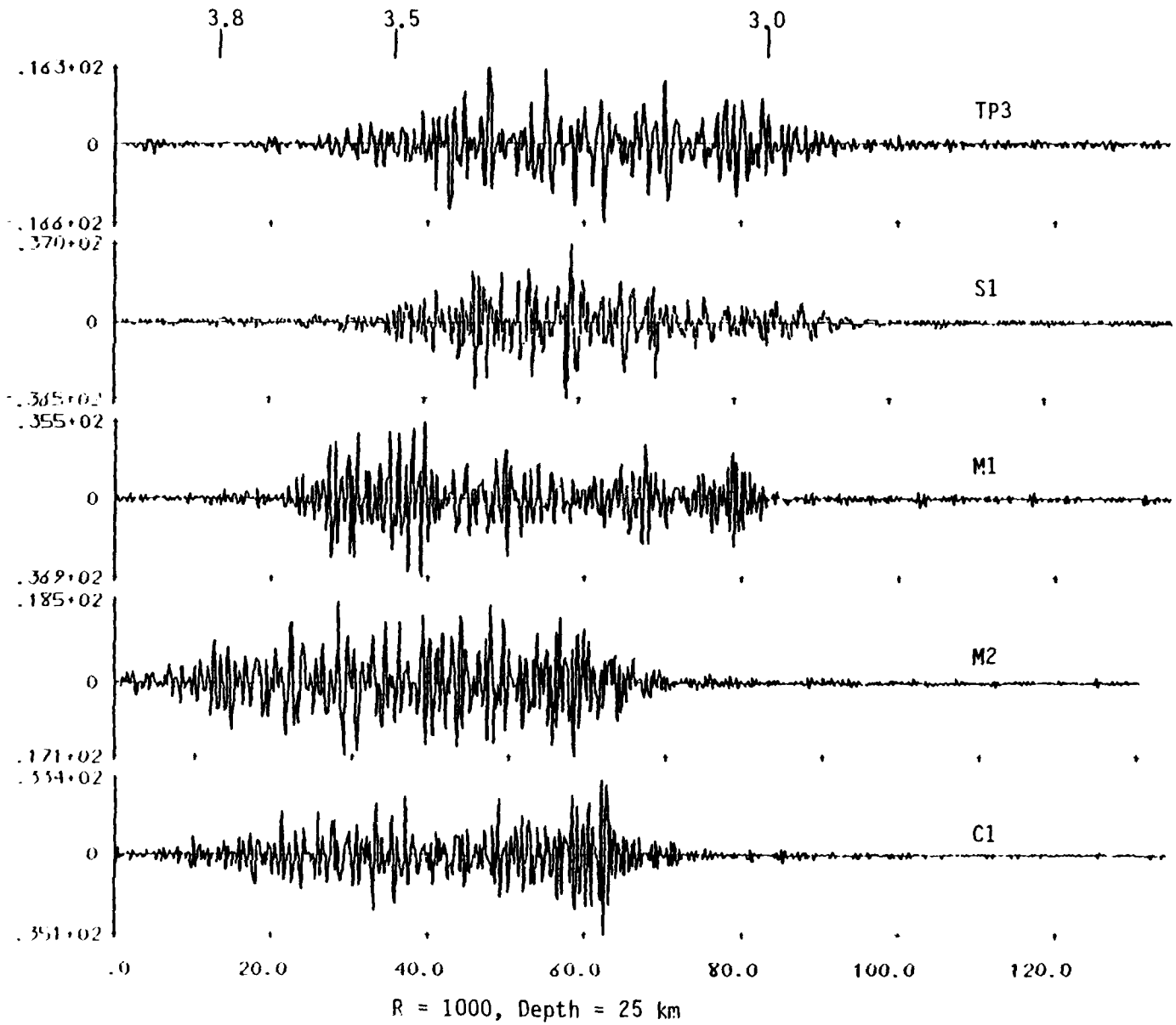

Figure 27. (continued)

locations where a distinct Moho appears to be present (D. V. Helmberger, personal communication). At such places it may be possible to generate an Lg-like phase.

Standard Tibetan Plateau models provide an excellent waveguide for Lg. The reason it does not propagate in this region must be sought elsewhere. One other possible explanation is that the Lg propagates in the region, but is severely attenuated upon passage across the boundary with other regions where attempts to observe Lg are made. Another explanation is that there is an unusual Q structure that attenuates this phase.

For all crustal models considered here in which synthetic Lgs are prominent, the onset group velocity of the phase is about 96-98 percent of the shear velocity at the base of the onset. The close ties between Lg onset velocities and lower crust shear velocities is to be expected given the energy distributions of Lg found in Bache et al, (1980). When one considers what Lg primarily is, namely, critically reflected shear waves guided between the Moho and earth's surface, one can make a more precise statement about the onset time. The onset time will be that of the arrival of the primarily snear wave wide-angle reflection off the Moho. Because of crustal velocity distribution with depth, this time is very nearly that of a snear wave propagating horizontally through the lower crustal layering.

V. DEPENDENCE OF Lg ON SOURCE DEPTH

In our semi-annual report (Bache et al., 1980) we discussed the theoretical dependence of Lg on source depth, using synthetic seismograms in the eastern U.S., crustal model S1 (Table 8). Those results were not entirely satisfactory, because a complete and consistent set of synthetic seismograms was not available to construct amplitude-depth curves. Since that time, we have computed a consistent set and the new results will be presented here.

Synthetic Lg seismograms were computed for a series of source depths in the model S1. The source was a point double-couple at the three fundamental orientation: strike-slip, vertical dip-slip and 45° dip-slip. The source time history was taken to be a step function with a fixed moment of 10^{25} dyne-cm. The WWSSN short period seismometer response was included. Synthetics were computed at a range of 1000 km for all three source orientations. In addition, the calculations were done at 500 km for the strike-slip double-couple.

The synthetic seismograms are shown in Figure 28. The Lg amplitude was measured on each seismogram. This was taken to be the maximum sustained amplitude (at least 3 cycles) within ten seconds of the 3.5 km/sec group arrival time.

The amplitudes are plotted versus source depth in Figure 29. This is basically a cleaner version of a similar plot that was shown in our semi-annual report. The computations are different in that:

(1) More depths are sampled,

(2) All synthetics are computed with the same instrument response,

(3) A more consistent and conventional technique for measuring Lg amplitude has been employed.

While the results are different in detail, the trends are the same as shown in our semi-annual report. The strike-slip and 45°

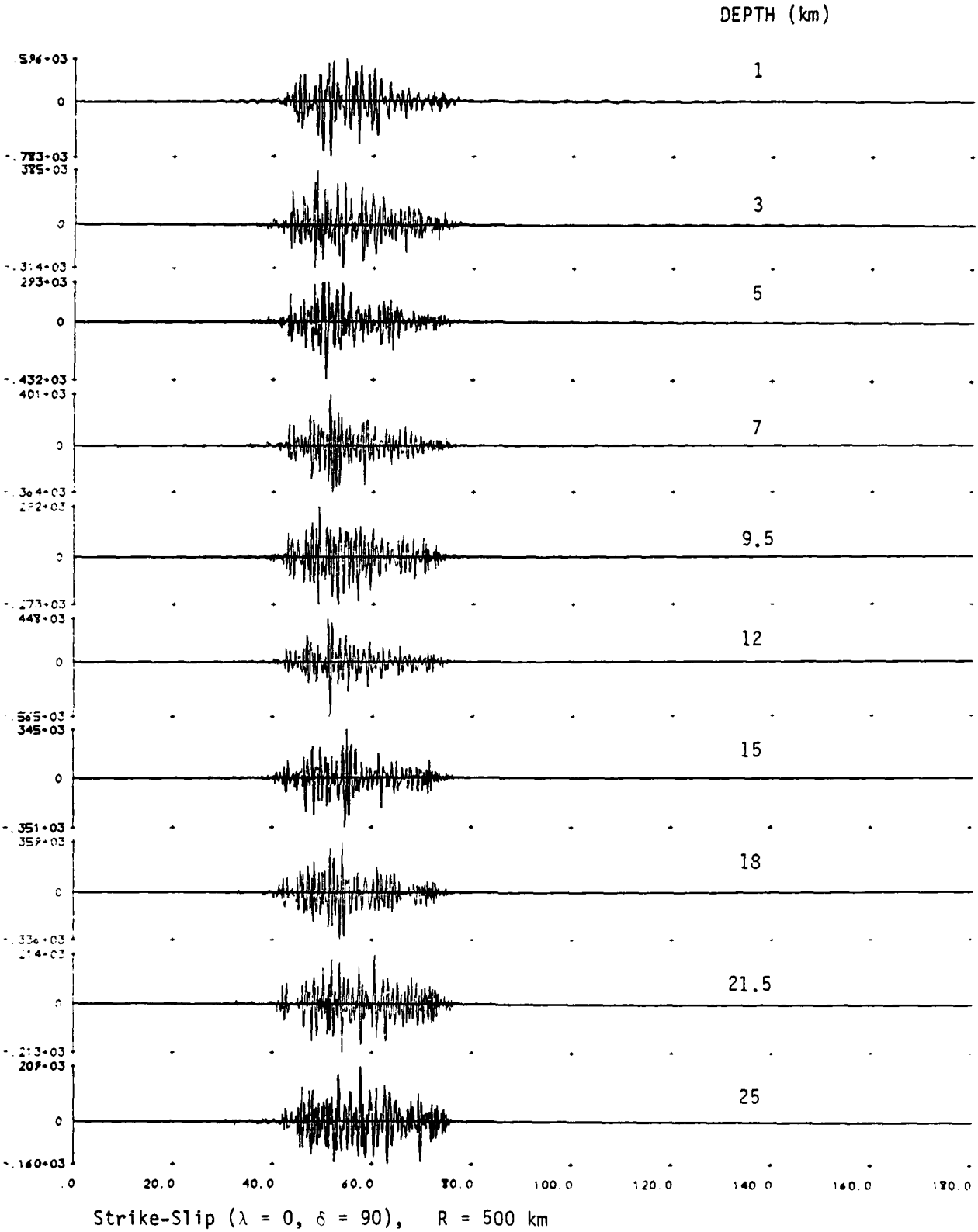

Figure 28. Synthetic seismograms for three double-couple sources at various depths in the model S1.

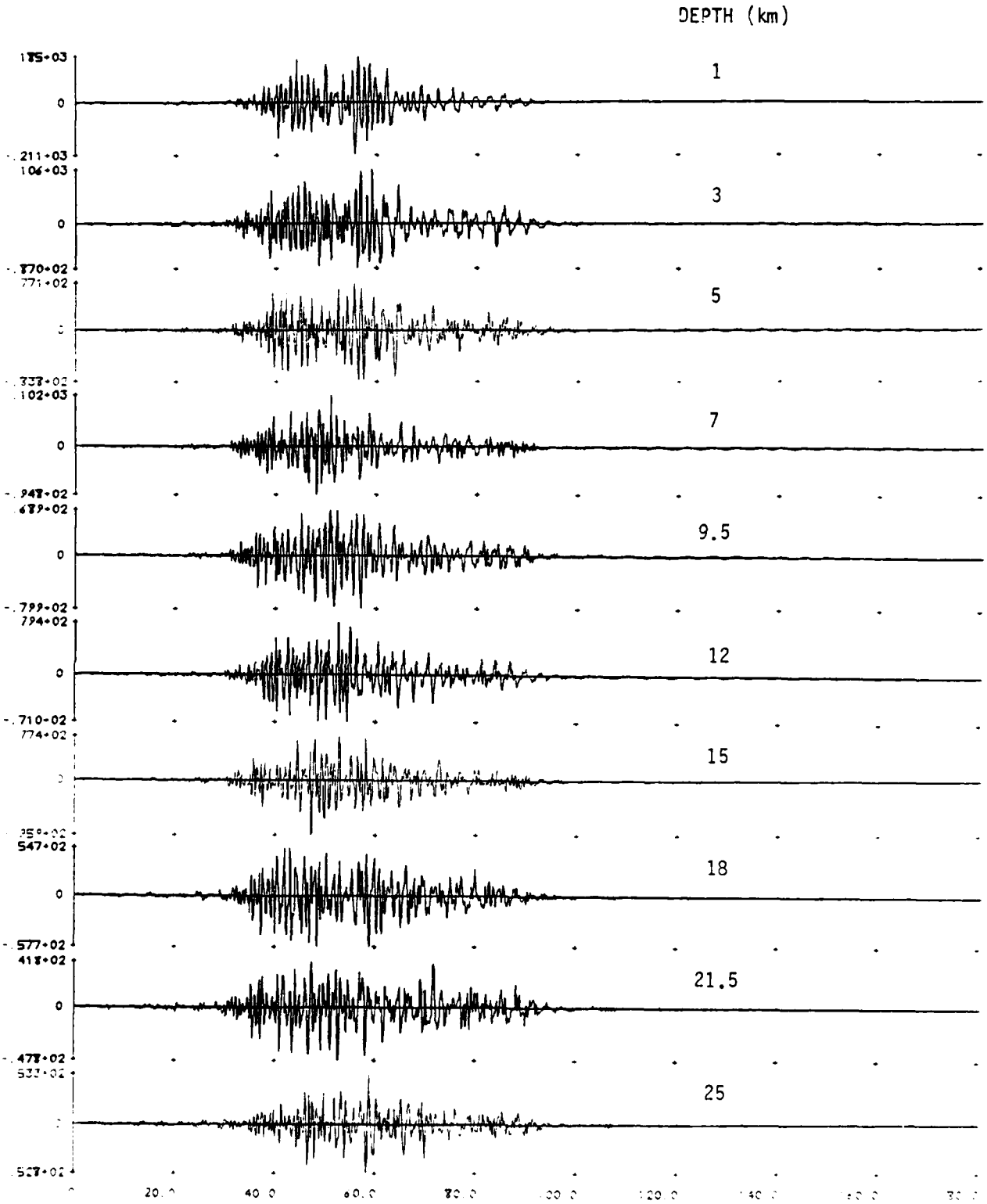

45 degree dip-slip (λ = 90, δ = 45), R = 1000 km

Figure 28. (continued)

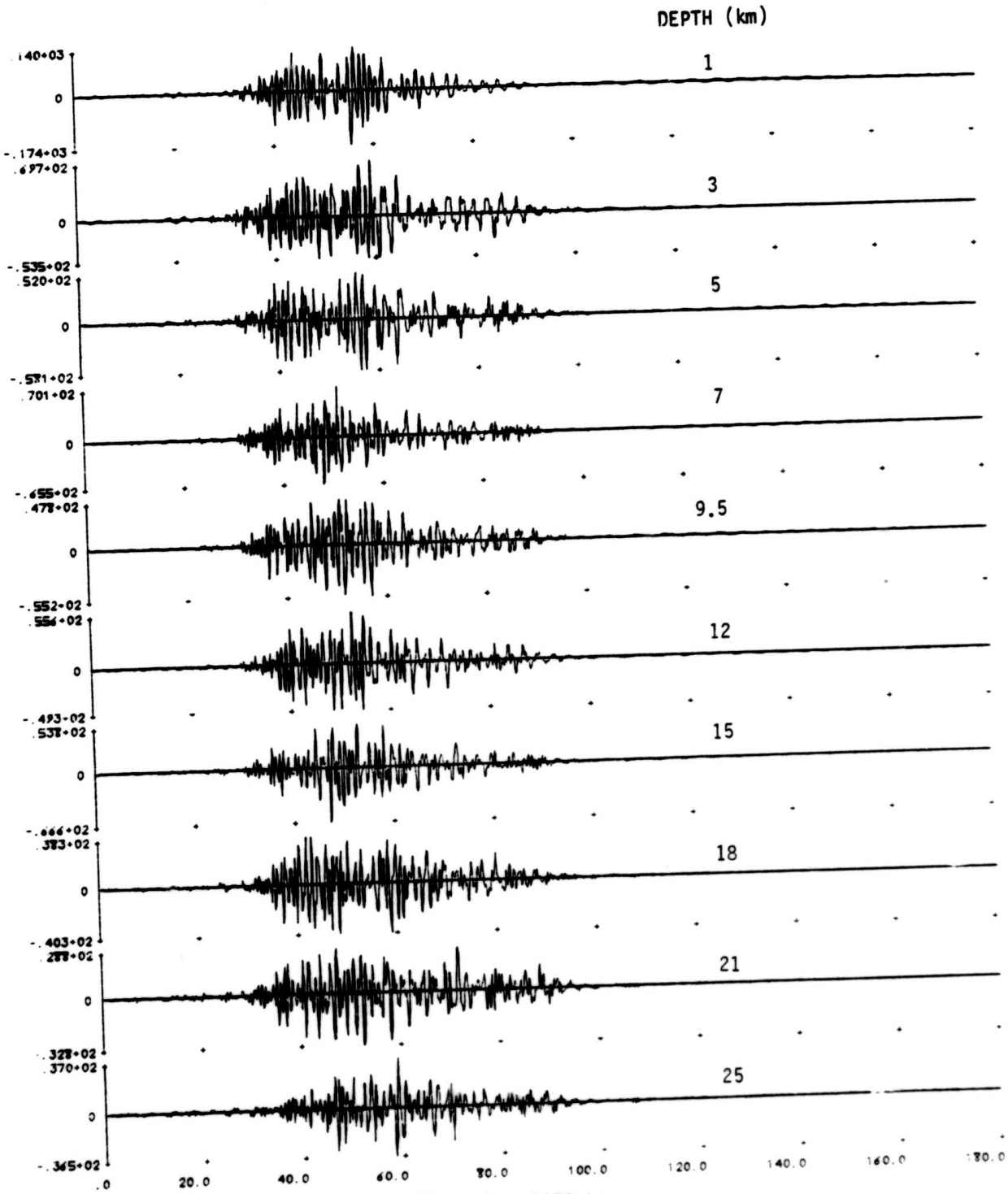

Strike-slip (λ = 0, δ = 90), R = 1000 km

Figure 28. (continued)

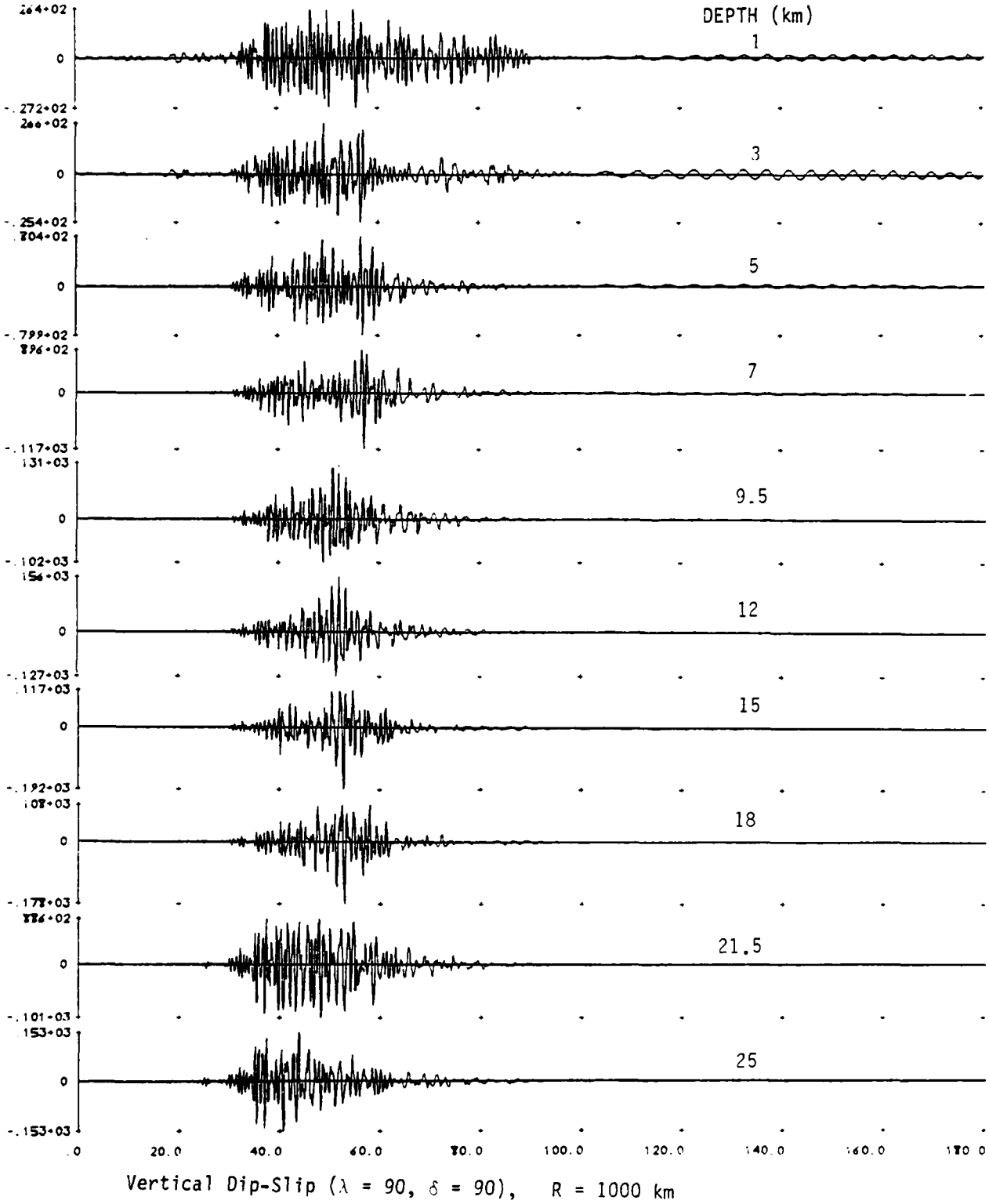

Figure 28. (continued)

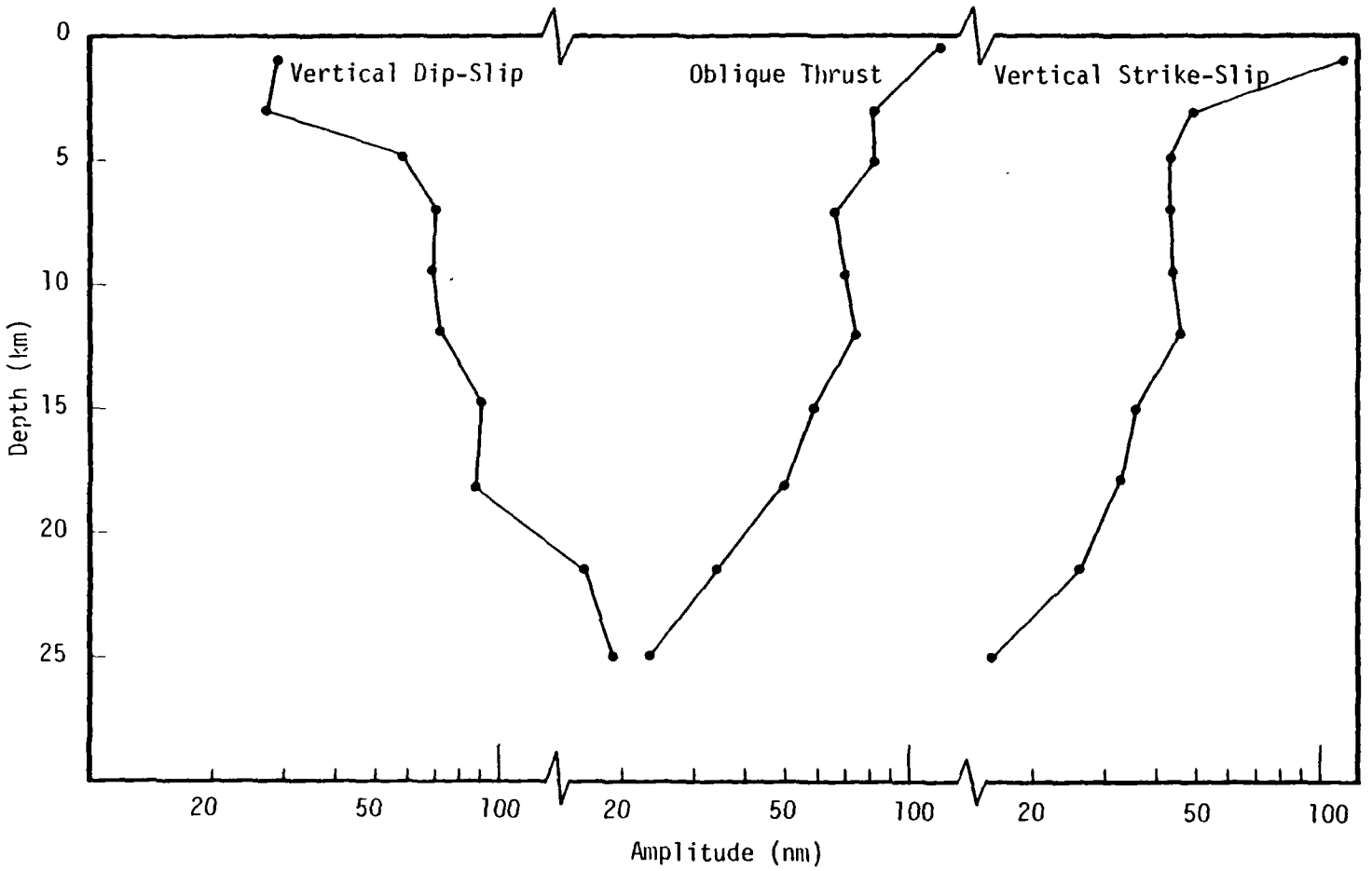

Figure 29. Lg amplitudes as a function of source depth for fixed seismic moment at 1000 km in an EUS crustal model.

dip-slip orientations show a similar decrease of Lg amplitude with depth. Most of the decrease is at the shallow and deep ends of depth interval. Between 3 and 21.5 km depths the decrease is only a factor of two or so. The normal dip-slip fault exhibits the opposite trend, except near the surface.

With this depth sampling, we can see that the proximity to an interface might be making some difference. The somewhat anomalous values at depths of 9.5 and 18 km are probably influenced by their distance from the interfaces.

The range dependence of the depth effect is indicated by comparing the R = 1000 km and R = 500 km cases for the strike-slip orientation. To parameterize this effect, we compute the effective attenuation (γ_{syn}) for each depth, using the procedure introduced by Nuttli (1973) (see Section 3.2). These are:

Depth	γ_{syn}(deg^{-1})
1	0.19
3	0.28
5	0.28
7	0.34
9.5	0.30
12	0.34
15	0.37
18	0.21
21.5	0.26
25	0.41

There are no striking trends in these γ. They have a mean of 0.30 deg^{-1} (0.07 standard deviation). This is close to the value we found for the structure S1 with an explosion source.

The amplitudes in Figure 29 are for a constant M_0 source. The relationship between M_0 and M_s is independent of the elastic properties of the source layer, so the plot is also for a constant M_s source. It may also be of interest to plot the depth dependence for a constant m_b. To show this, it is necessary to scale by the elastic properties of the source layer.

Using geometrical ray theory for a spherical earth with depth dependent velocity, the far-field P-wave amplitudes, ignoring source radiation pattern, can be written (Aki and Richards, 1980, Chapter 9)

$$U_p(r_R, \Delta, t) = \frac{\cos i_R \, \dot{M}_o(t - T)}{4\pi \left[\rho_R \, \rho_s \, \alpha_R \, \alpha_s^5\right]^{1/2} R(\underline{r}_R, \underline{r}_s)}$$

with

$$R(r_R, r_s) = \frac{r_R \, r_s}{\alpha_s} \left| \cos i_R \cos i_s \sin \Delta \left| \frac{\partial \Delta}{\partial P} \right| / P \right|^{1/2}$$

where

M_o = moment
T = travel time
i = takeoff or incident angle from the vertical
r = radius from earth's center
Δ = range (angle)
P = ray parameter

and S, R refer to source and receiver.

The factor depending on source properties is

$$\frac{1}{r_s \left[\rho_s \, \alpha_s^3 \cos i_s\right]^{1/2}} \quad .$$

For crustal source depths and teleseismic distances, r_s and $\cos i_s$ vary by only a few percent so the dominant depth effect is the factor

$$\frac{1}{\left[\rho \, \alpha_s^3\right]^{1/2}} \quad .$$

The computed Lg amplitudes for fixed m_b are shown in Figure 30. Note that much of the depth dependence for vertical

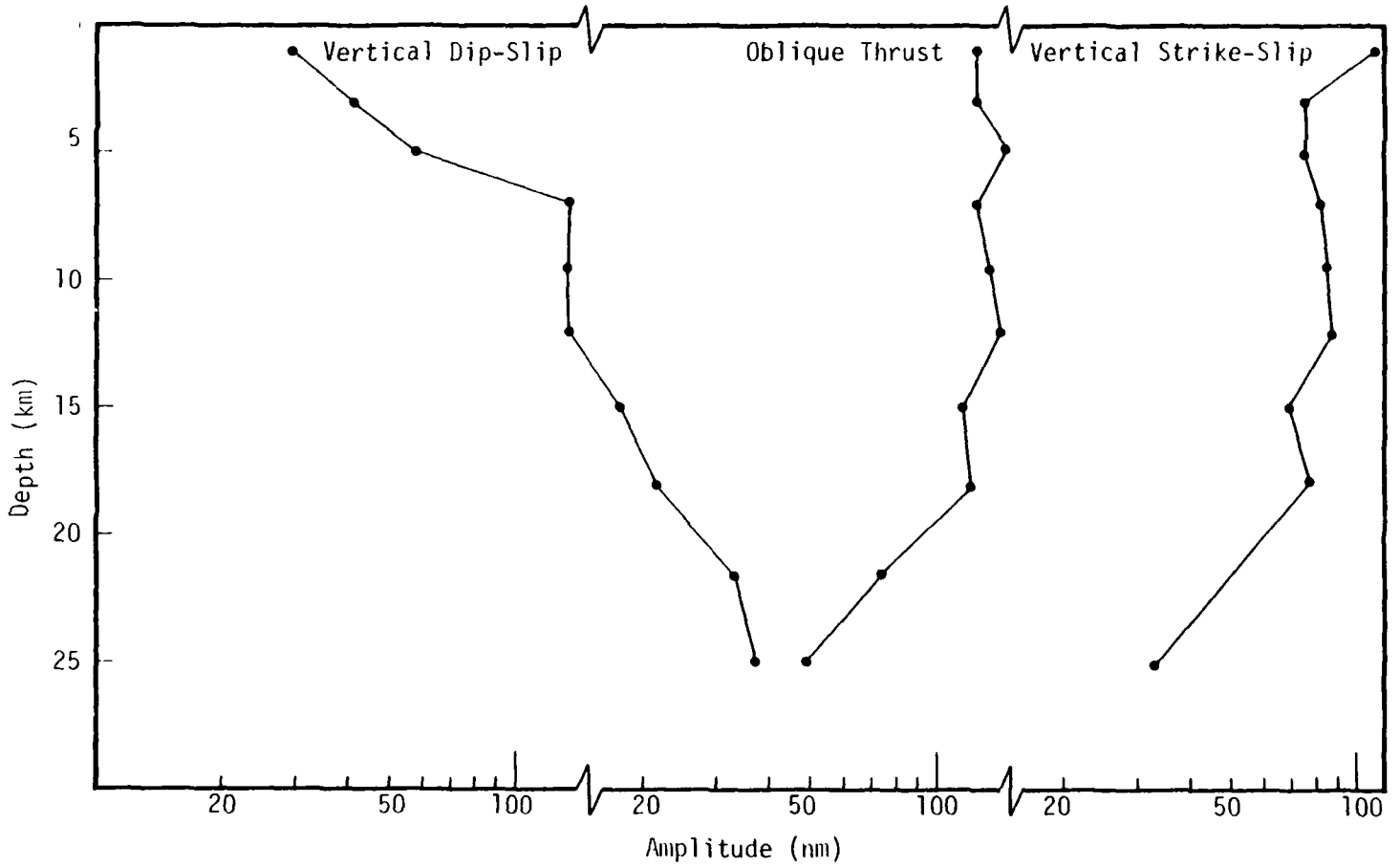

Figure 30. Lg amplitudes as a function of source depth for fixed "m_b" at 1000 km in an EUS crustal model.

strike-slip and oblique thrust sources is compensated for by the depth dependent factor above. For vertical dip-slip sources, on the other hand, the depth effect becomes even more pronounced.

VI. THREE-DIMENSIONAL SOURCE-SIMULATION CAPABILITIES

Some important seismic source phenomena are fundamentally both three-dimensional and nonlinear. Tectonic earthquakes are an example. Buried explosions near nonhorizontal geologic interfaces or near imperfectly-welded rock joints represent another class of three-dimensional sources. One tool for studying the near- and far-field ground motion excited by such sources is three-dimensional finite difference simulation. For this purpose, Systems, Science and Software (S^3) developed the TRES code (Cherry, 1977), a small-strain finite difference code which operates on the S^3 UNIVAC 1100/81. TRES was constructed to optimally exploit the scalar processing capabilities of the UNIVAC.

Because of the large computational requirements of three-dimensional seismic modeling, the TRES algorithm was subsequently reprogrammed (by the Institute for Advanced Computations) to run on the ILLIAC IV parallel-processing computer. This conversion was a multi-man-year effort, because of the unique demands of the ILLIAC. Code development for the ILLIAC proved to be about an order of magnitude more time-consuming than comparable development efforts on the UNIVAC. Once in place, however, the ILLIAC version of TRES, designated I4TRES, executed three-dimensional dynamic simulations, involving up to about one million finite difference nodes, in a few hours of computing time. This code was used by S^3 during FY '79 to develop a shear failure model for earthquakes, and during FY '80 to perform several large-scale earthquake simulations, with the objective of improving the theoretical basis for seismic source identification techniques.

Two tasks under this contract, allocated approximately ten man-weeks each, were directed toward improving this three-dimensional source-modeling capability. Task 1 was to provide support to Technology Development Corporation (TDC), (formerly the Institute for Advanced Computation) in order to modify the I4TRES

code. Task 2 involved converting TRES from the S^3 UNIVAC to the CRAY I computer at the National Center for Atmospheric Research (NCAR), and then comparing the performance of TRES on the UNIVAC, CRAY, and ILLIAC computers. Below, we summarize the work accomplished under these tasks and our conclusions about the three-dimensional modeling capabilities of the CRAY I version of TRES.

6.1 SUMMARY OF TASK 1

Under Task 1, S^3 provided TDC with appropriate algorithms and test problems designed to enable TDC to upgrade the modeling capability of I4TRES. The objectives were:

1. Complete and test the multiple-materials version of TRES which had been under development by TDC.
2. Make it compatible with S^3's nonlinear rupture model.
3. Allow for general free-surface interactions, including outcropping thrust faulting.

The S^3 algorithms and test problems are documented in Appendixes A and B.

As of the begining of January, 1981, Objective 1 had been successfully met as evidenced by the results of two key test problems discussed below. Objective 2 was successfully met in March, 1981. Completion of Objective 3 has not been successfully demonstrated.

I4TRES was drastically reformulated by TDC to accommodate material heterogeneity. Test Problem I, described in Appendix B, was intended to verify that the revised code correctly modeled faulting in a homogeneous, elastic halfspace. In particular, we wanted to verify that the revised difference equations reduce to the correct boundary conditions at the free surface and at the fault plane.

Figure 31 shows free-surface displacement time-histories computed by I4TRES for Problem I. Also shown are two independent solutions, obtained by the Cagniard-de Hoop method (Johnson, 1974) and a quasi-three-dimensional finite element method (Day, 1977), respectively. Comparison of the Cagniard-de Hoop and finite element solutions illustrates the filtering effect associated with discrete methods such as finite element and finite difference: frequencies corresponding to shear-wavelengths shorter than about six zone-dimensions are inaccurately propagated by the numerical methods and have been suppressed by artifical viscosity. Since the zone size used in I4TRES was twice as large as that used in the finite element solution, the filtering effect is even more severe for the I4TRES solution, as expected. However, low-frequency characteristics are preserved in the I4TRES solution, and demonstrate that the code is working satisfactorily for this test case.

Test Problem II was designed to verify that the revised I4TRES correctly models wave propagation in a non-homogeneous halfspace. Even for the case where the halfspace consists of a few discrete, horizontal, elastic layers, only a few complete solutions, valid in the near field, are available in the literature. Problem II treats a problem for which we have a published solution obtained by the quasi-three-dimensional finite element method (Day, 1977). Again, the three-dimensional I4TRES solution and quasi-three-dimensional finite element solution must be compared in light of the fact that the zone size of the I4TRES calculation was twice that of the finite element calculation. Thus, the I4TRES solution should be essentially a low-pass filtered version of the finite element solution. Figure 32 shows that this is the case.

Test Problem III was designed to ensure that the nonlinear rupture model operates correctly in conjunction with the multiple-material version of I4TRES. Successful completion of this test problem was verified by comparing the new numerical results to numerical results obtained for the same problem with an earlier

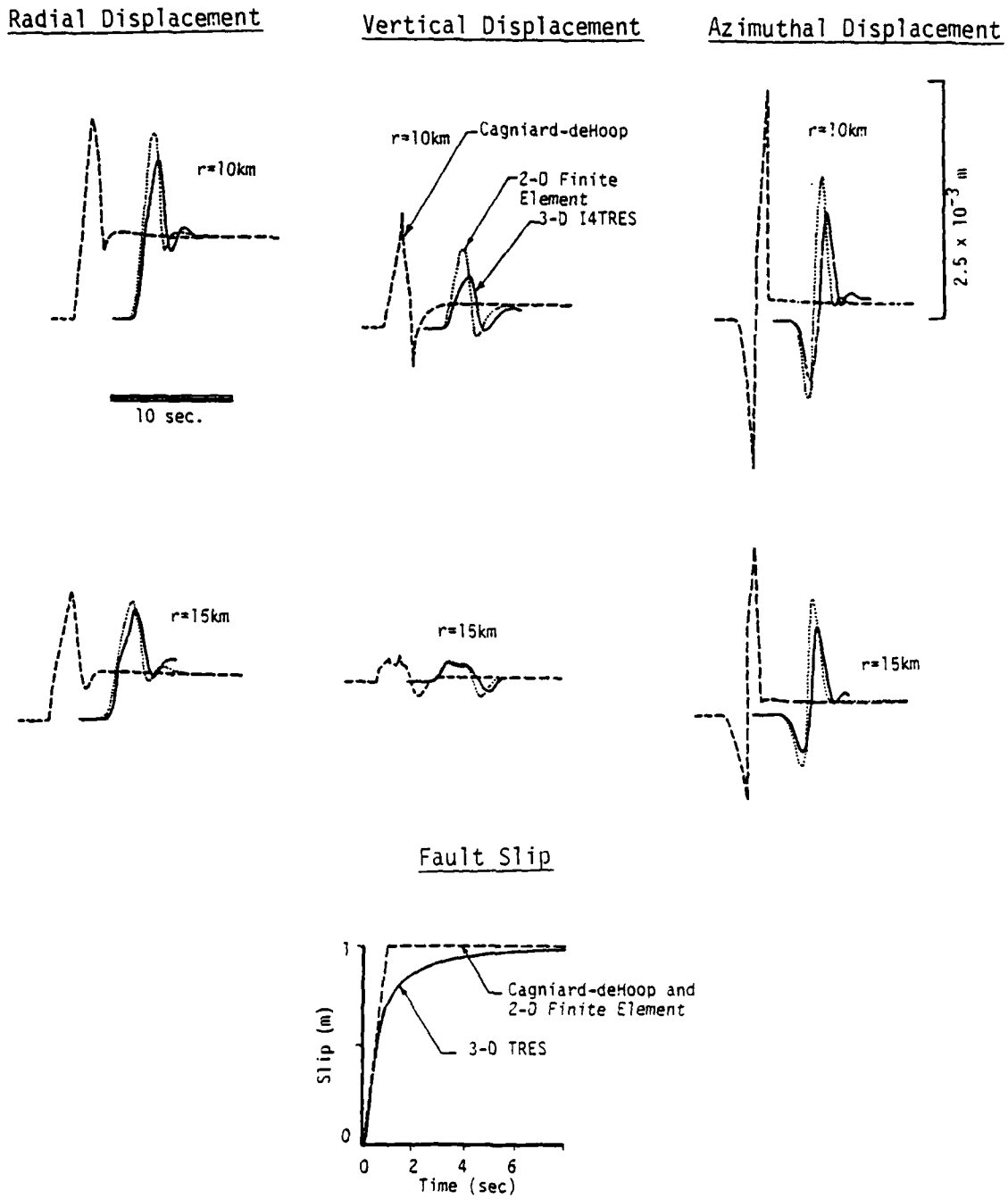

Figure 31. Free surface displacement waveforms for Test Problem I, computed with I4TRES (the ILLIAC IV version of the TRES code); displacements computed by two alternate methods are shown for comparison. The slip functions shown were applied to a 1 km^2 fault area, centered at 5 km depth. Observers are at an azimuth of 22.5° from epicentral distance.

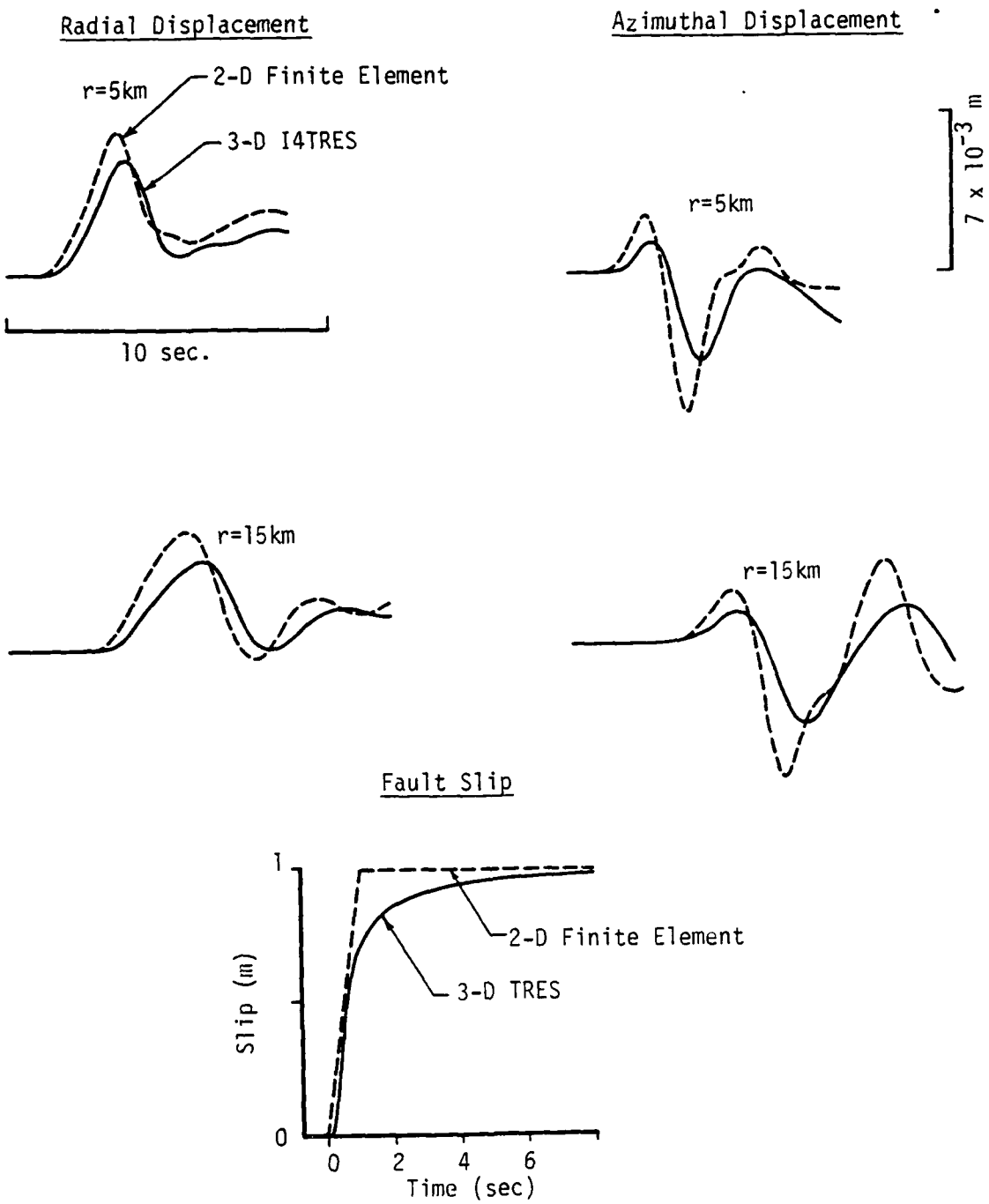

Figure 32. Free surface displacements for I4TRES Test Problem II, compared to a two-dimensional finite element solution (Day, 1977). Source-receiver configuration is the same as for Figure 31.

version of I4TRES. Discrepancies were found to be insignificant and fully attributable to the (algebraically equivalent) rearrangement of the difference equations in the new version of I4TRES.

In conclusion, the results of Test Problems I, II and III are very satisfactory. The I4TRES code as now configured can accurately treat three-dimensional wave-propagation in a heterogeneous medium, including the stress-relaxation which accompanies fault propagation at a specified rupture velocity. In addition, the S^3 shear failure algorithm given in Appendix A has been successfully integrated into the I4TRES code. The capability to model non-vertical faults has not been demonstrated by successful completion of Test Problem IV.

6.2 SUMMARY OF TASK 2

The objective of Task 2 was to evaluate the performance of the TRES code on the UNIVAC 1100/81, ILLIAC IV, and CRAY I computers. The main accomplishments were:

1. Creation of a version of the TRES code in CRAY FORTRAN (CFT).
2. Partial vectorization of TRES to exploit the vector-processing capabilities of the CRAY I.
3. Comparison of TRES code execution times on the three computers.

Conversion of the vectorization of TRES are briefly discussed in Appendix C. The remainder of this section gives the results of the comparison of TRES runs on the three computers.

It is difficult to make precise comparisons of run times among the three computers. The real objective of such a comparison should be to try to predict the relative performances of the computers for large "production" runs. For this purpose, the most useful form in

which to express the timings would be as, say, CPU-seconds per finite-difference zone per time step. In fact, once this figure is deduced for a moderate-sized test problem, we can predict UNIVAC run-times with reasonable confidence for very large problems simply by assuming that run-time is proportional to the product of the number of zones and the number of time steps in the problem.

However, computing times for the ILLIAC and CRAY machines are distinctly nonlinear in the number of zone-cycles and the form of the nonlinearity is different for each. Furthermore, for both the UNIVAC and CRAY computers, it is essential to correct test problem timings for the fact that only part of the finite difference grid is active during the initial stages of a given calculation.

Because of the above considerations, we determined that a single test problem was inadequate to enable us to predict the relative performance of the computers. Instead, we performed several calculations with various grid configurations. Based on these runs, we compare the expected performance of the three computers for problem sizes of practical interest. Table 10 summarizes the runs used in the analysis.

6.2.1 ILLIAC Computing time

TRES run times on this machine are reasonably well understood as a result of several years experience with large-scale calculations. Let J, K, and L be the number of finite difference zones in the x,y, and z directions so that the total number of zones in the problem is the product JKL. Then the computer time (in seconds) per cycle, T, is approximately:

$$T \approx .094\ L \left\lceil \frac{K}{20} \right\rceil \left\lceil \frac{J}{60} \right\rceil \qquad (1)$$

where the bracket symbol [x] indicates the smallest integer greater than or equal to x. Thus, T is proportional to L and independent of

TABLE 10

TIMING COMPARISON OF TRES ON UNIVAC 1100/81, ILLIAC IV, AND CRAY I

Run No.	Machine	Problem Size				Average Fraction of Zones Active	CPU Time (sec)	Active Zones x Time Steps ÷ CPU - Sec.	$\frac{\text{Zones x Time Steps}^{(1)}}{\text{Fx CPU - Sec.}}$
		J	K	L	Number of Time Steps				
1	ILLIAC	60	30	59	150	1.0	1662.000	9584	9584
2	UNIVAC	60	30	59	3	1.0	575.000	554	739
3	CRAY	60	30	59	14	1.0	178.000	8353	11137
4	CRAY	60	30	59	3	1.0	33.000	9655	12873
5	UNIVAC	21	3	21	25	1.0	70.500	469	625
6	CRAY	21	3	21	25	1.0	6.265	5280	7040
7	CRAY	80	5	159	50	0.22	88.000	7950	10600
8	CRAY	80	5	159	71	0.30	178.000	7611	10147

(1) F is the average fraction of the grid estimated to be active during a typical production run.

$$F = \begin{cases} 0.75 & \text{for UNIVAC and CRAY} \\ 1.0 & \text{for ILLIAC} \end{cases}$$

J up to J = 60. For very small problems ($k \leq 20$), T is also independent of K; while for very large problems ($k \gg 20$), T is practically proportional to K. This J and K dependence renders the ILLIAC relatively much more efficient for very large problems. Combined hardware/software restrictions limit ILLIAC problem size to J = 80, K = 80, L = 160.

6.2.2 CRAY Computing Time

Computing time for the CRAY depends linearly on K and L. For J, however, dependence is nonlinear due to the vector processing capabilites of the machine and the partially vectorized configuration of the code. CPU-time divided by J decreases somewhat with J up to J = 64; for larger J, there is first some increase in T/J, then a decrease up to J = 128.

An activity test has been incorporated into TRES so that, for most calculations, T increases in approximate proportion to the time-step number during the first half of the problem (while the wavefield spreads and the entire grid gradually becomes active); then T remains stationary at a maximum value during the second half of the problem (during which the disturbance at the external grid boundaries propagates back into the central region of the grid). Thus, for a typical problem, 3/4 of the grid will be active during tne average time-step. The effects of the activity test must be accounted for both in interpreting the test-problem performance and in extrapolating to large-scale problems. After compensating for this grid-activity effect, we find approximately

$$T \approx c(J)KLJ \tag{2}$$

where

$$c(60) \approx .00012$$
$$c(21) \approx .00019$$
$$c(80) \approx .00013$$

6.2.3 UNIVAC Computing Time

For this machine, there is no preferred index; that is, we expect approximate proportionality of T to JKL. The grid activity effect is the same as described for the CRAY. After correcting for activity, we find approximately

$$T \approx cJKL \tag{3}$$

where

$$c \approx .0019$$

6.2.4 Summary

To compare ILLIAC times to those of the other two machines, we should account for the benefits of limited grid activity during early timesteps. In Figure 33, we plot JKL/T, the number of zones times the number of timesteps per CPU-second. Values of JKL/T implied by Equations 2 and 3 for the UNIVAC and CRAY, respectively, have been multiplied by 4/3 since, as we have said, the average number of active zones during a large calculation is usually about 3/4 JKL.

The figure indicates that the CRAY is somewhat faster than the ILLIAC for most TRES problems, sometimes by as much as a factor of two. For certain optimal configurations, however, the ILLIAC can probably beat the CRAY by as much as 15 percent or so.

In special cases where the average active fraction of the grid is nearly 1, the ILLIAC and CRAY will give quite similar times for most configurations; on the other hand, for special cases in which the fractional activity is less than 3/4, the advantage of the CRAY will be proportionally greater than suggested by Figure 33.

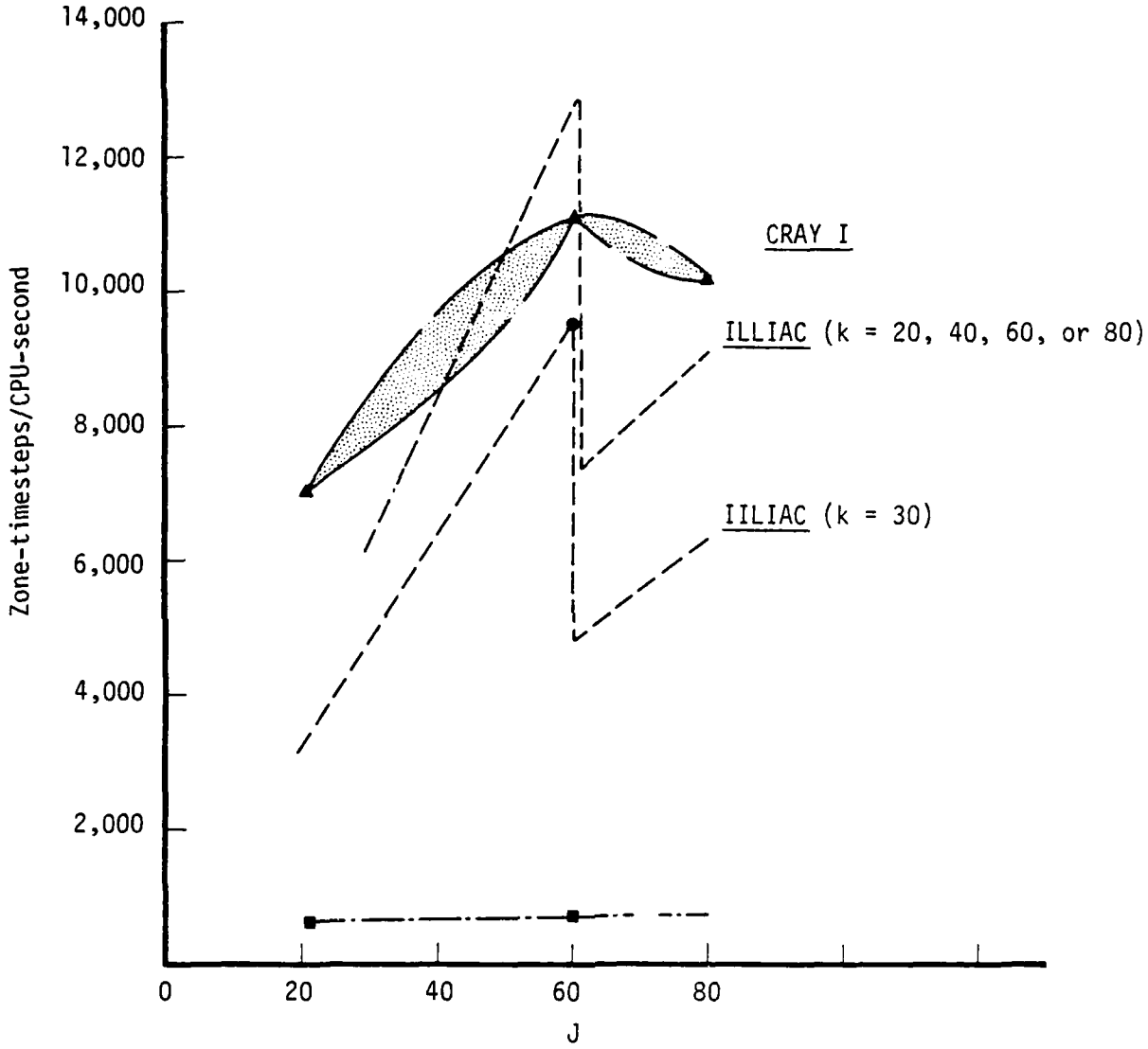

Figure 33. Speed of execution of TRES, in zone-cycles per CPU-second. The horizontal axis, J, is the problem size (number of finite difference zones) in the X direction. Data points are given by solid circle, squares, and triangles. Curves represent interpolation and extrapolation of the data as described in the text.

For large problems, say J greater than 40, the CRAY currently runs TRES approximately 15 times as fast as does the UNIVAC.

At this point, we should emphasize once again that the TRES code has been only partially vectorized to exploit the CRAY'S capabilites. We estimate that a substantial effort to fully vectorize TRES would yield another factor of four or greater improvement in speed on the CRAY.

VII. SIMULATION OF THE VERTICAL GROUND ACCELERATIONS IN THE 1971 SAN FERNANDO, CALIFORNIA, EARTHQUAKE

7.1 INTRODUCTION

In this section we summarize an effort to simulate the near-field ground response in the 1971 San Fernando, California, earthquake. A computer program for the simulation of the ground acceleration provided by S^3 has been used by the Mission Research Corporation (MRC) to estimate the level of acoustic disturbances expected for that event. Simulated ionospheric disturbances can be compared to those of underground tests to determine the potential of ionospheric monitoring techniques as a possible discriminant.

S^3's part in this overall effort was to provide an efficient ground motion simulator to MRC for obtaining reasonable estimates of the near-field motion. Here, we describe the methods used in computer algorithms provided to W. Wortman of MRC, S. Warshaw of LLL, and J. Bannister of Sandia Laboratories. In Section 7.2, the mechanism of the San Fernando earthquake is briefly reviewed, and the sections following thereafter discuss the implementation of our algorithm. Our final model for the source includes three distinct events which are represented by three circular cracks situated on the rupture surface. The choice of the source parameters of the discrete sources is guided by short period teleseismic observations and the observed near-field velocities at Pacoima Dam.

7.2 PAST STUDIES OF THE SAN FERNANDO FAULTING MECHANISM

The 1971 San Fernando earthquake is probably the most studied earthquake in history. The location and moderate size resulted in numerous teleseismic and strong-motion data of reasonable quality. Over the past decade numerous studies of the teleseismic and near-field data have been made using both short and long period information. For the present application, the intermediate frequencies are of interest. The acoustic pressure signatures are most closely reflected by the characteristics of near-field ground

velocity (W. Wortman, personal communication), which, at Pacoima Dam, falls into the frequency range of about 0.5 to 3.0 Hz. For this frequency range, studies of near-field velocity and short period teleseismic data are most informative. Most notable studies of this variety are Hanks (1974), Boore and Zoback (1974), Bache and Barker (1978), Bouchon (1978), and Cherry, et al. (1976).

From all of these studies, there are a few fundamental observations about the faulting mechanism which can be identified:

1. The faulting process was quite complicated. This was first noted by Hanks (1974), who noted the presence of several strong arrivals on both the short period teleseismic body-wave data and the near-field accelerations.

2. There was an unusually high stress release in the vicinity of the hypocenter. Estimates generally range from 200 to 500 bars. Consistent findings in this regard were found by Hanks (1974), Bache and Barker (1978) and Bouchon (1978).

3. The rupture surface was kinked. This was apparent when the fault-plane solution for the initiation was found not to project from the hypocenter to the location of surface breakage.

4. There appears to be large static slip at both the hypocentral region and at shallow depths near the surface breakage (Alewine, 1974; Heaton and Helmberger, 1978).

5. There is some source of significant high frequency radiation initiated at, or near, the surface breakage.

Any reasonable source model for the event must include most, or all, of the above mentioned features. Features 1 - 3, and 5 are very important to determining the characteristics of the near-field radiation in the frequency range of interest.

Our interpretation of the results of previous studies suggests a multiple source mechanism consisting of three discrete events. The ground velocities infered from the recorded accelerograms at Pacoima Dam indicate three distinct disturbances in the intermediate frequency band (Figure 34). The largest velocities are primarily associated with the first phase beginning about 2.5 seconds into the record on all three components. On the component S74W, two other strong phases are quite obvious at 6 and 8 seconds. These secondary arrivals are present on the other two components, but are less obvious.

The source of the first two disturbances can be found in the model proposed by Bache and Barker (1978). Their model, which was constrained primarily from teleseismic data and partially by the Pacoima Dam vertical records, consists of two primary areas of stress release (Figure 35). The dominant radiation initiates from the hypocentral region with a large stress drop. A second suggested region of concentrated energy release is located just above the kink in the fault. The arrival times at Pacoima Dam from this part of the Bache and Barker model is quite consistent with the second burst of energy observed 6 seconds into the record.

The third source of energy has largely gone unexplained. This disturbance produced the large accelerations (over 1 g) observed on both horizontal components, which at the time were the largest ground accelerations ever recorded. The traditional hypothesis concerning the source of this radiation is that it results from Rayleigh waves generated by a surface breakout of the rupture. The physics of such a process is not well understood, and quantitative verification of this hypothesis has not been made. We feel that some treatment of this disturbance is necessary, but do not feel that the traditional explanation is necessarily a good one. First, the amplitude of the vertical motion is quite small relative to the horizontal. The ground velocity on S74W is roughly three times that of the vertical and S16E roughly twice the vertical. This does not appear consistent with Rayleigh wave motion in what is essentially a

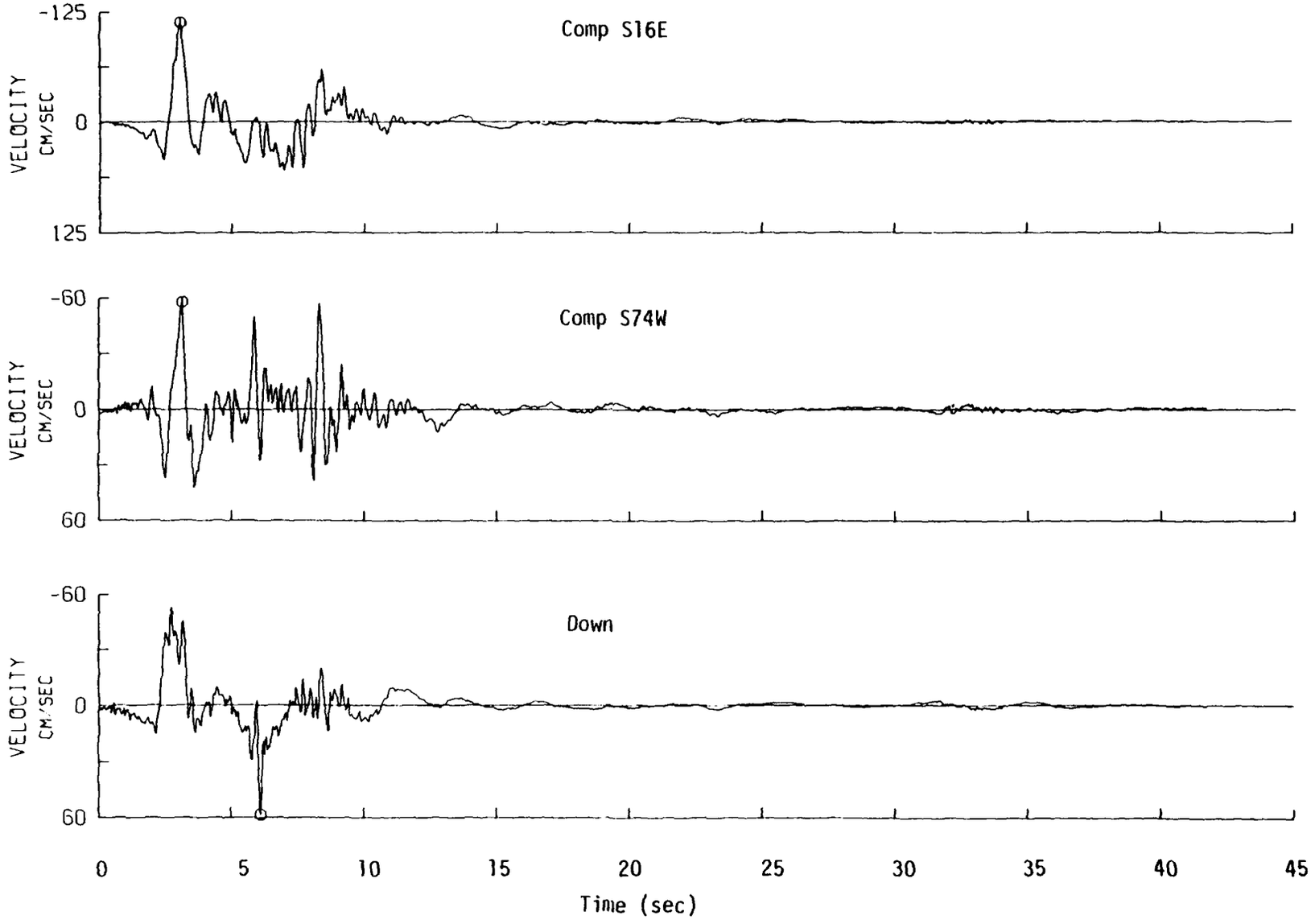

Figure 34. Processed ground velocity observed at Pacoima Dam (from EERL, 1973).

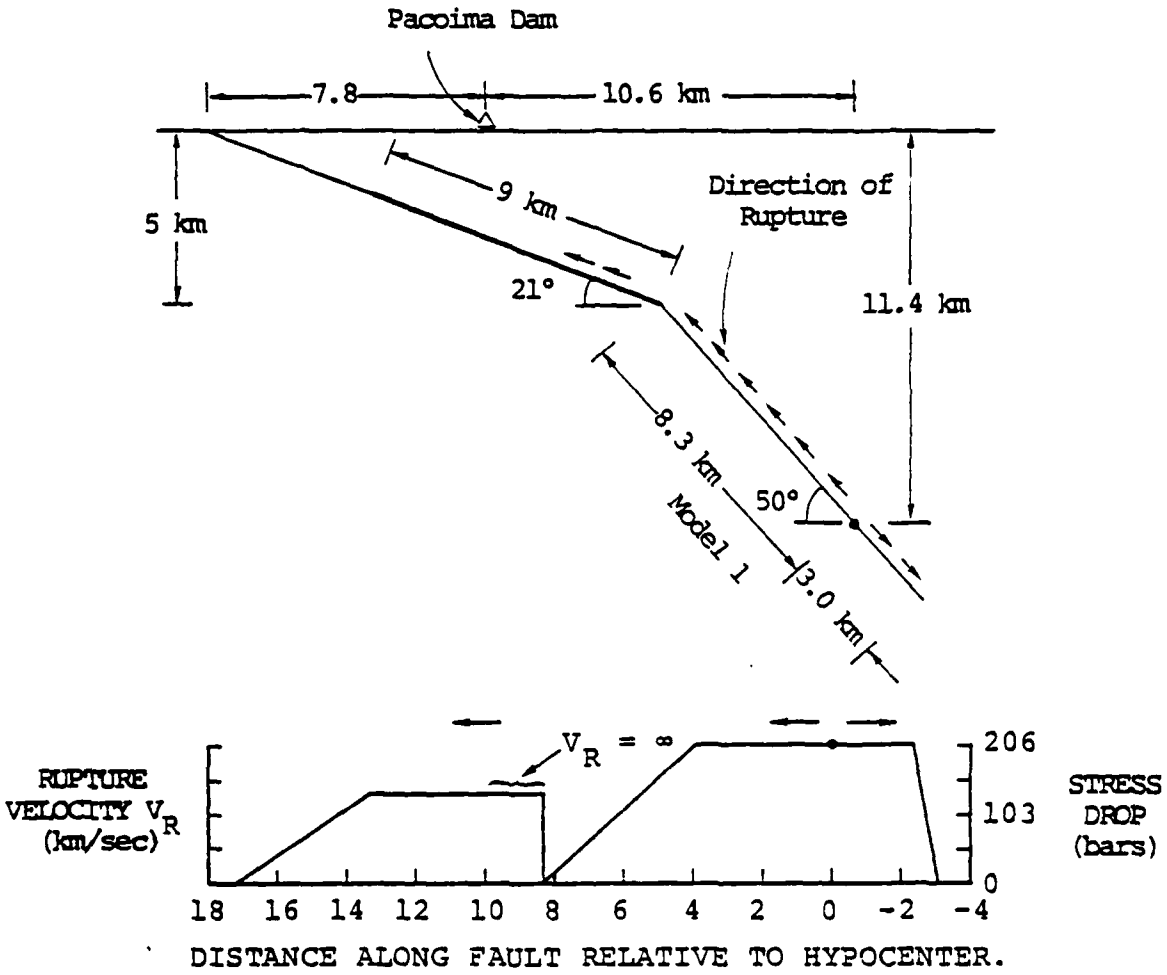

Figure 35. Source model for the San Fernando earthquake from Bache and Barker (1978).

homogeneous half-space. Second, static observations (Alewine, 1974) and modeling of the near-field displacements (Heaton and Helmberger, 1978) indicate large slip ($\sim$4m) at depths of a few km which is twice that at the surface. Given these two observations, we suggest that a more likely source of the radiation was a shallow stress concentration nearly beneath Pacoima Dam. Shear waves radiating from below would produce relative horizontal to vertical motion more consistent with the observations. The center of this disturbance could also correspond to the location at maximum slip at shallow depths.

7.3 REPRESENTATION OF DISCRETE SOURCES OF RADIATION

In this section, we describe the source representation employed for the discrete sources of radiation. We will use a modification of a method used by Day et al., (1980) which used an approximation to the far-field radiation from an expanding circular shear crack which stops gradually.

Several closed-form analytic approximations to the slip history of a circular shear crack with uniform stress-drop are available. These are generally motivated by the early analytical solution of Kostrov (1974) and numerical simulations, like Madariaga (1976), which include the stopping of rupture. Boatwright (1980) provides a summary of available analytic expressions. Even though simple expressions for the slip history on the fault exist, simple representations of the geometrical far-field radiation, in general, do not. The exception is the model of Sato and Hirasawa (1973).

The Sato and Hirasawa model (which we will call the S & H model) is simply an expanding, constant rupture velocity, circular crack for which slip everywhere on the crack terminates instantaneously when the rupture reaches a prescribed radius. Their model is not a rigorous dynamic solution, as shown by the numerical solution of Madariaga (1976). His calculations revealed that termination of slip actually occurs only when healing phases

propagate inward from the fault edge at the P and S velocities of the medium. The advantage of the S & H model is that its geometrical far-field radiation can be obtained analytically in closed form. Given the geometry shown in Figure 36, the geometrical far-field acceleration can be written

$$\ddot{U}_r = \frac{(\beta/\alpha)^3}{4\pi\beta r} \sin 2\theta \cos \phi \, \ddot{I}_\alpha$$

$$\ddot{U}_\theta = \frac{1}{4\pi\beta r} \cos 2\theta \cos \phi \, \ddot{I}_\beta \tag{7.1}$$

$$\ddot{U}_\phi = \frac{-1}{4\pi\beta r} \cos \theta \sin \phi \, \ddot{I}_\beta$$

with

$$\begin{aligned}
\ddot{I}_c = {} & \frac{4\pi\dot{D}_o V^2}{(1 - K^2)^2} \left[H(t) - H(t - \frac{L}{V}(1 - K)) \right] \\
& - \frac{\pi\dot{D}_o V^2}{K(1 + K)^2} \left[H\left(t - \frac{L}{V}(1 - K)\right) - H\left(t - \frac{L}{V}(1 + K)\right) \right] \\
& - \frac{\pi\dot{D}_o VL}{K(1 - K)} \, \delta\left(t - \frac{L}{V}(1 - K)\right) \\
& + \frac{\pi\dot{D}_o VL}{K(1 + K)} \, \delta\left(t - \frac{L}{V}(1 + K)\right)
\end{aligned} \tag{7.2}$$

where

$\dot{D}_o$ = slip velocity at center of crack

V = rupture velocity

L = fault radius

K = $V/C \sin \theta$

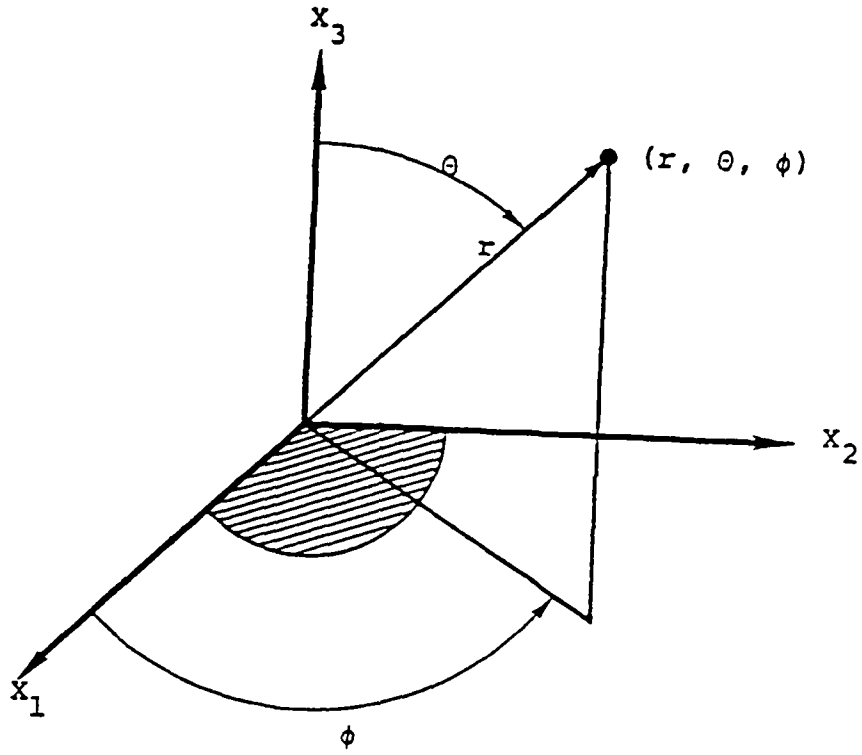

Figure 36. Coordinate system conventions used. Shaded area represents the fault surface.

t = reduced time

α, β = compressional and shear velocities, repectively in the source region

c = α or β

$H(t)$ = Heaviside step function

$\delta(t)$ = delta function

The time domain behavior is shown in Figure 37. Acceleration initiates as a step which continues until the arrival of the stopping phase from the edge of the fault nearest the observer. From that time until the time of arrival of the stopping phase from the farthest edge of the fault, the acceleration is constant.

There are several noteworthy characteristics of the accelerations. The high frequency content is clearly dominated by the stopping phases, which are (mathematically) delta functions. These cause the far-field displacement spectrum to decay as ω^{-2} at high frequencies. The amplitudes of the first stopping phase and the step initiating the motion contain terms of $K(1 - K)^{-1}$ and $(1 - K^2)^{-2}$ respectively. These terms make the amplitudes of the early parts of the motion rather strong functions of the rupture velocity and the azimuth of the observer from the fault normal. For example, with a rupture velocity of 0.9β, where β is the shear speed of the medium, the amplitudes of the initiation phase in the plane of the fault and at the fault normal differ by more than a factor of 27. For a given slip velocity, changing the rupture velocity from 0.8β to 0.9β causes the initiation phase to increase by a factor 4.5 in the plane of the fault, but only by 1.1 at the fault normal.

The delta-function dependence in the stopping phase will, of course, be smoothed by an attenuating medium, but even with reasonable values for the intrinsic attentuation Q^{-1}, it appears that the predicted stopping phases are much too strong to be consistent with near-field observations. The amplitude of the phase

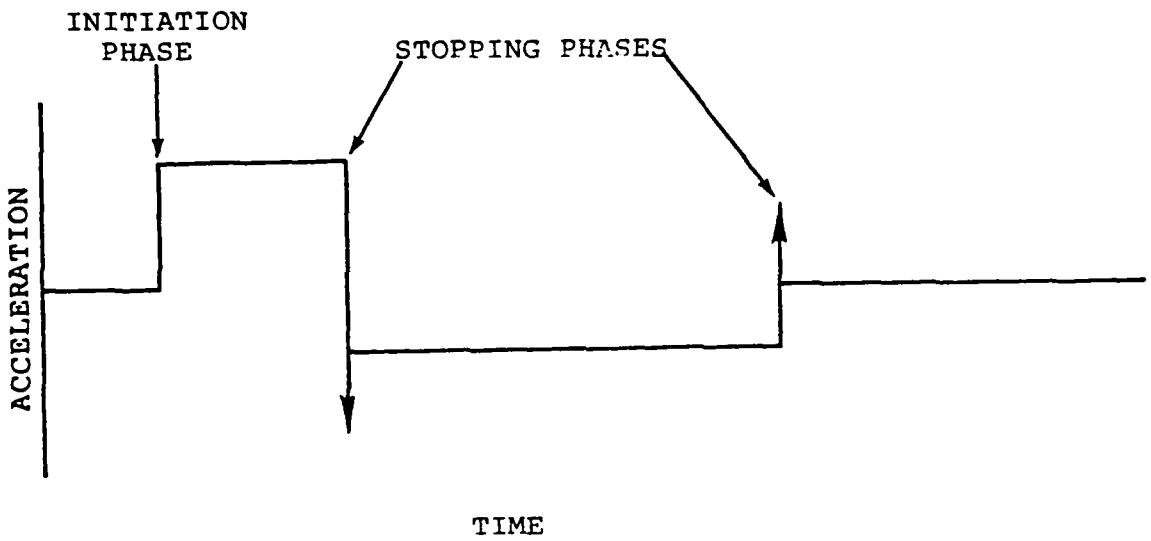

Figure 37. Typical shape of the Sato and Hirasawa model geometrical far-field acceleration. Arrows represent delta functions.

can be roughly estimated, given linear attentuation, using the asymptotic formulas of Kjartansson (1979). He suggests the peak time domain amplitude of a causal, attenuated pulse to be roughly CQ/R times the strength of the input delta function, where C is the signal velocity and R is the distance traveled. For example, Hanks (1974) suggested that the initiation event for the 1971 San Fernando, California, earthquake had a stress drop of 350 to 1400 bars over a fault radius of 3 to 6 kilometers. We can estimate the relative peak amplitudes of the initiation and stopping phases observed at Pacoima dam, R = 15 kilometers and very near the plane of the fault. Figure 38 shows the values predicted by the S & H model for a 400 bar stress drop and 5 kilometer fault radius, for a Q of 100. Except when the rupture velocity is near the shear velocity, the stopping phase is estimated to be considerably larger than the initiation phase. Only relatively slow rupture velocities can predict reasonable values. Since the absolute values depend on many poorly constrained parameters, the relative values are the most meaningful. If actual recordings are examined (Figure 39), the step-like feature is evident on all three components of motion about 2.5 seconds into the record. After approximately 0.6 seconds, there is a sudden downward phase indicating some kind of stopping, but the peak amplitudes are, at best, comparable to the initiation phase on the order of 0.5 g. A better evaluation of the model is achieved by using the stopping time (t = 0.6 sec) to constrain the fault radius $L = Vt/(1 - K)$. When this is done, the predicted stopping phase is 7 to 8 times larger than the predicted initiation phase for all rupture velocities between 0.5β and 0.99β.

Clearly, the stopping phases of the S & H model are much too strong, in a linearly attenuating medium, to be reasonable. There are numerous explanations for this inadequacy of the model, and a detailed discussion will not be undertaken. There are two items worth discussing -- the mode of healing and the abruptness with which rupture growth terminates. The S & H solution does not treat healing rigorously. Numerical solutions suggest that the healing of the fault when rupture propagation terminates is not instantaneous,

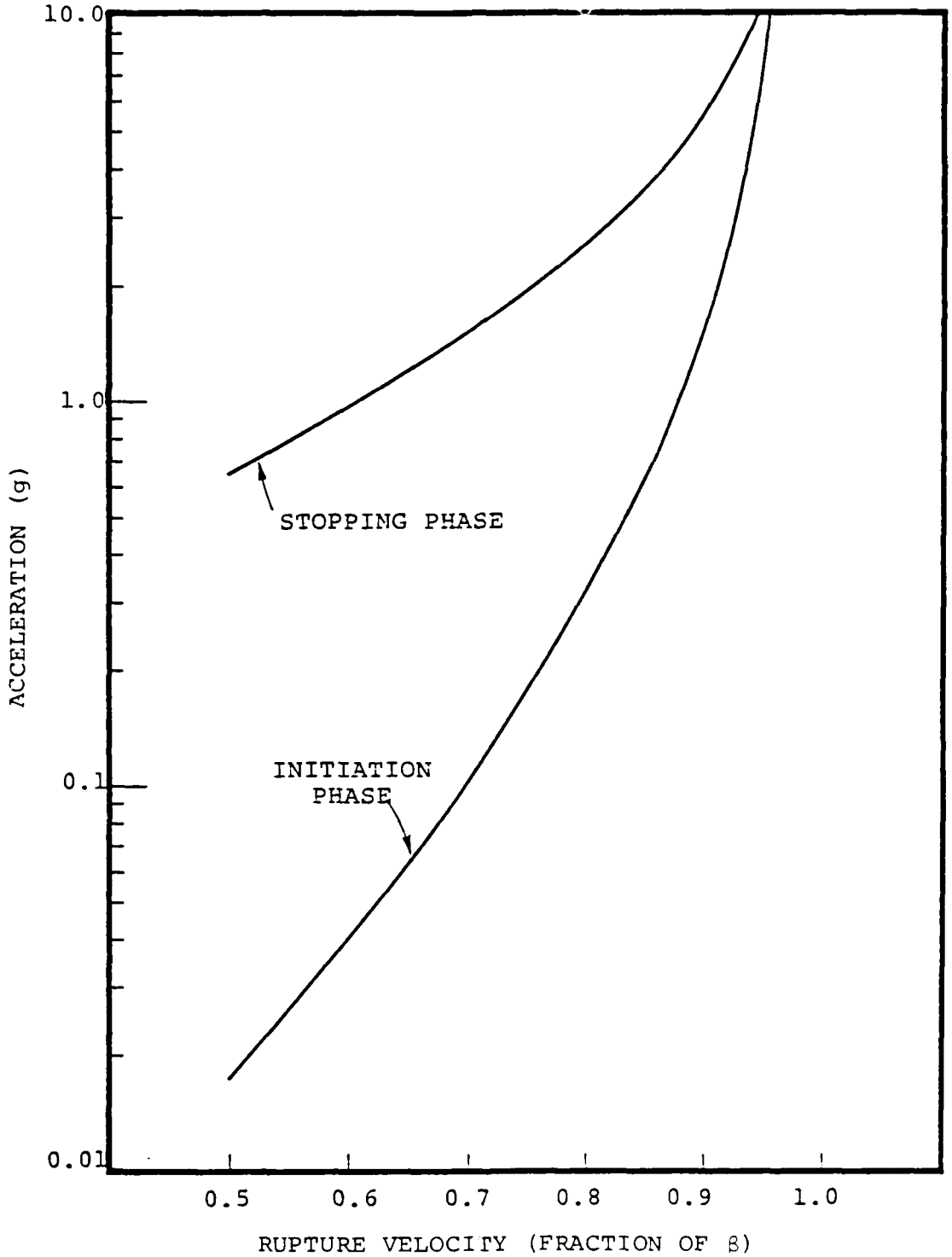

Figure 38. Initiation-phase and stopping-phase amplitude as predicted by the S & H model for a 400 bar stress drop and 5 km fault radius, assuming a Q of 100.

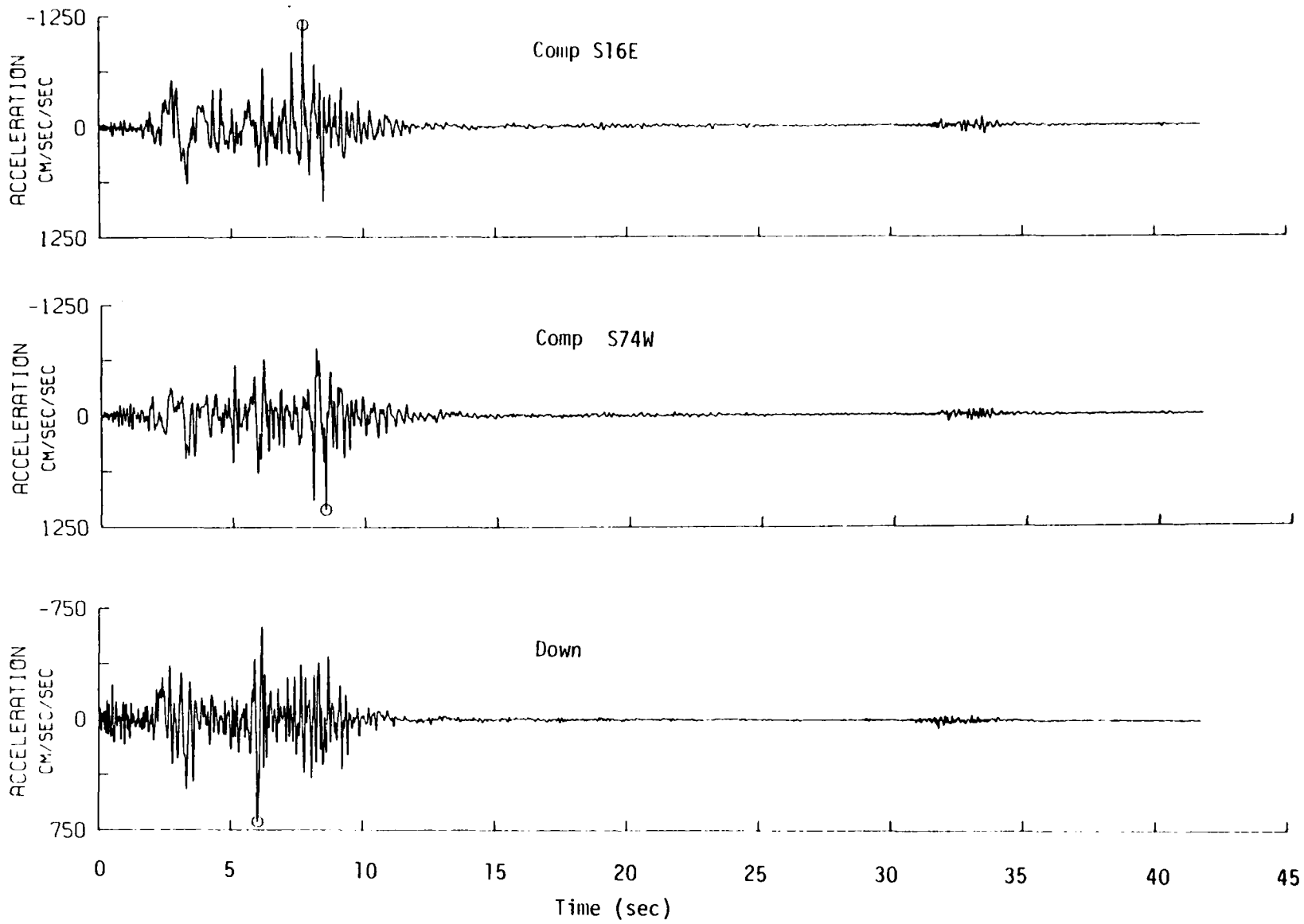

Figure 39. Processed ground acceleration observed at Pacoima Dam (from EERL, 1973).

as assumed by the S & H model, but propagates inward at the seismic signal velocities. The approximate treatment of healing is probably not as influential in controlling peak acceleration as it may at first seem; Madariaga's (1976) numerical solution, which treats healing more rigorously, has an ω^{-2} far-field displacement spectrum indicating that it, too, gives singular acceleration.

Of greater importance is the manner in which rupture growth stops. In the S & H model, rupture stopping is very idealized. The propagating rupture decelerates instantaneously along a smooth, prescribed boundary (a circle). The values of observed peak accelerations suggest that this approximation is unacceptable for predicting the characteristics of high frequency radiation.

Clearly, a decelerating model of rupture is needed. The D-model of Boatwright (1980) would be an appropriate choice, but at present, no simple far-field representation of the motion from this model is available. Although an analytic far-field solution is not essential, it does add considerable flexibility to the calculations and facilitates interpretation of computed waveforms. As an alternative to employing a rigorous numerical solution for a decelerating rupture model, we choose, for simplicity, to alter the form of the far-field radiation from the S & H model to have a deemphasized stopping phase. The most convenient way to do this is to assume that the rupture deceleraties over an annular region of width S. The stopping phase will then be smoothed out over a time related to S.

Boatwright's (1980) D-model provides a convenient parameterization of the effect. He introduces a parameter, which we will call γ (Boatwright's $(\frac{\nu-1}{\nu})^{1/2}$, $\nu > 1$), which controls the time of the stopping process. For a radius L and rupture velocity V, the rupture remains uniform out to a radius γL, at which point the rupture decelerates. The duration of the uniform rupture process is then $\frac{\gamma L}{V}$, and it is assumed that the rupture reaches the boundary at a time $\frac{L}{\gamma V}$. For $\gamma = 1$, this model is identical to the S & H model. For $0 < \gamma < 1$, the stopping radiation will be smoothed.

One could solve directly for the radiation due to Boatwright's D-model, but since the details of the stopping process of such a model is arbitrary anyway, it seems more convenient to instead assume some simple form for the characteristics of the stopping phases which satisfies all gross conservation conditions and qualitatively approximates the actual far-field solution. The far-field radiation from a dislocation type source must conserve the integrals of acceleration and velocity and have an intergral of displacement proportional to seismic moment. As an alternative to the D-model, we simply replace the delta-function stopping phases with steps of duration consistent with the time of deceleration of the D-model as perceived at the observer, and choose amplitudes which conserve the integrals of acceleration, velocity and displacement. An example is shown in Figure 40.

In summary, the Sato and Hirasawa crack approximation appears to be unreasonable when high frequency radiation is of interest. The large stopping phases predicted by the model are, in general, too large to be consistent with observed values of acceleration close to earthquakes. A more acceptable model for the radiation from a stress concentration apparently requires a deemphasis of the high frequency radiation due to the stopping of rupture. Here we choose an alternative representation of the far-field radiation from an isolated release of stress which includes a smoothing of these stopping phases.

The source parameters for the three discrete sources used here are summarized in Table 11. The orientation angles are defined as in Aki and Richards (1980), Chapter 4. The spatial coordinate system used is centered at the epicenter of the first source and positive X and Y is in the north and east directions respectively. The moment-magnitude was determined using the relationships proposed by Hanks and Kanamori (1979).

7.4 FREE SURFACE CORRECTION

For most near-field applications, the interaction of the radiation with the free surface and surficial layering can be quite

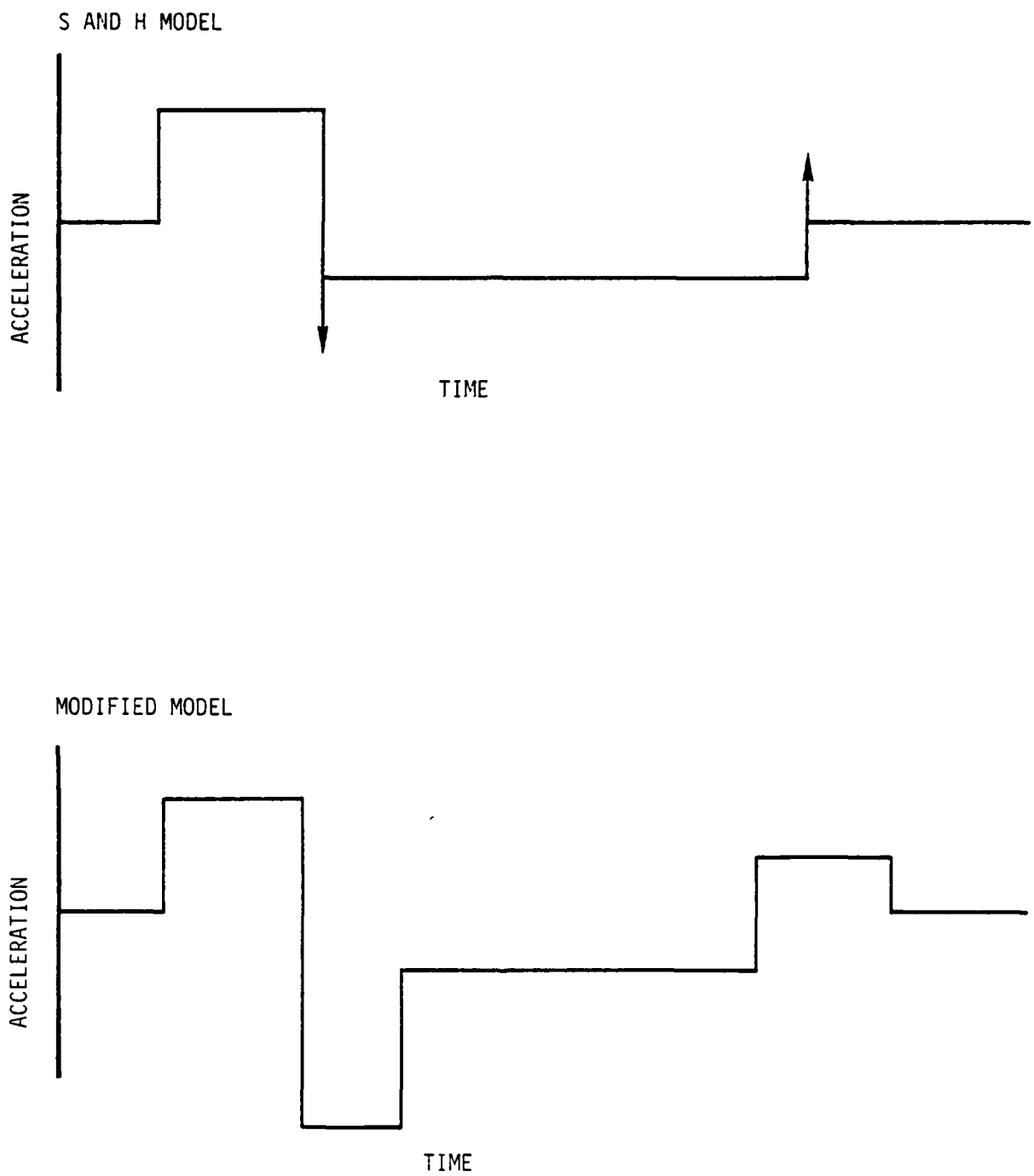

Figure 40. Comparison of typical shapes of far-field acceleration from the Sato and Hirasawa model and the modified model used in this study.

Table 11

SOURCE PARAMETERS

	#1	#2	#3
Fault strike (deg)	-75.0	-75.0	-75.0
Dip angle (deg)	53.0	29.0	29.0
Slip angle (deg)	76.0	90.0	90.0
X-coordinate (km)	0.0	-9.0	-15.5
Y-coordinate (km)	0.0	3.0	4.0
Depth (km)	13.0	6.0	2.5
Fault radius (km)	6.0	3.0	1.0
Fraction of radius for which rupture is uniform	0.4	0.8	0.8
Rupture velocity (km/sec)	2.31	2.31	2.31
Slip velocity (cm/sec)	600.0	200.0	200.0
Initiation time (sec)	0.0	7.4	11.6
Moment magnitude	6.4	5.6	4.6

important to determining the characteristics of the surface ground motion. For the case of the San Fernando earthquake, the medium in the vicinity of the event can be adequately approximated by an elastic half-space, and surficial layering does not appear to be important in the epicentral region. There are a number of exact algorithms for determining the free surface motions from point dislocation sources (Johnson, 1974, for example). These algorithms are not expensive when the response for few source-receiver pairs are of interest. Standard methods for computing the atmospheric coupling must evaluate a surface integral of the ground acceleration for each time desired in the acoustic signal. For this case, use of rigorous free surface responses would be much too costly.

As an alternative to complete free surface calculations, we employ an approximate method first suggested by Knopoff et al., (1957). The total response is approximated by the response of an incident plane wave with incident angle corresponding to the geometrical arrival in the complete response. The correction factor is a complex scale factor which can be obtained analytically. The scale factor is applied such that the output signal is the input signal times the real part of scale factor plus the Hilbert transform of the input signal times the imaginary part of the scale factor. The final response will not include Rayleigh waves or S to P phases refracted along the surface.

An accurate derivation of the method can be found in Anderson (1976) (Knopoff et al., 1957, contains some misprints). Given a P-wave with incident angle i or an S-wave with incident angle j, we define a ray parameter:

$$s = \frac{\sin i}{\alpha} = \frac{\sin j}{\beta} \quad .$$

For incident P-waves, the scale factor is always real and can be expressed as:

$$R_V^P = \frac{2 \cos 2j}{\beta^2 D}$$

$$R_H^P = \frac{2 \sin 2i \cot j}{\alpha^2 D}$$

where

$$D = \frac{2s \cos i \sin 2j}{\alpha} + \frac{\cos^2 2j}{\beta^2} \quad .$$

R_V^P (R_H^P) is the ratio of the predicted vertical (radial) response to the whole space vertical (radial) response.

For incident SH waves, the transverse scale factor is two, independent of incident angle. For SV waves, the scale factor is real for sub-critcal incidence ($\sin j < \beta/\alpha$) and complex for super-critical incidence. For subcritical case,

$$R_V^S = \frac{4s \cos i \cot j}{\alpha D}$$

$$R_H^S = \frac{2 \cos 2j}{\beta^2 D} \quad .$$

For super-critical incidence,

$$R_V^S = \frac{4 \, sb \cot j}{D'} \, e^{(i(p - \frac{\pi}{2})}$$

$$R_H^S = \frac{2 \cos 2j}{\beta^2 D'} \, e^{(i(p + \theta)}$$

where

$$b = \sqrt{s^2 - 1/\alpha^2}$$

$$D' = \left[\left(\frac{\cos 2j}{\beta}\right)^4 + (2sb \sin 2j)^2\right]^{1/2}$$

$$\tan p = \frac{2\beta^2 sb \sin 2j}{\cos^2 2j}$$

and

$$\theta = \begin{cases} 0 & \sin^{-1}\frac{\beta}{\alpha} < j \leq \frac{\pi}{4} \\ \pi & \frac{\pi}{4} < j < \frac{\pi}{2} \end{cases} .$$

The approximation used here can be summarized as a high-frequency, first-motion approximation. It is exact for SH waves and excellent for incident P-waves at all incident angles and for subcritical SV waves. Near the critical angle, it is poor. Beyond critical, it performs quite well at times near the arrival time of the geometrical arrival, but fails at times where a Rayleigh wave or an S-P converted phase is expected. Anderson (1976) shows several comparisons between the response predicted by the method given here and complete half-space and whole space responses.

7.5 DESCRIPTION OF ROUTINES

One master routine, SFVERT, and five slave routines generate approximate vertical accelerations for a simulation of the 1971 San Fernando, California earthquake. The version summarized here returns the acceleration for a given location at a given time. It does not generate a complete time history at each call. The routines are accessed by:

CALL SFVERT (DT, XR, YR, XC, T)

where

DT = Input time increment used only for smoothing the response to prevent aliasing. The value used should be comparable to the time increment of a final seismogram or pressure signature desired.

XR,YR = Input cartesian coordinates of desired receiver in kilometers. The coordinate system is positive to the north and east and centered at the earthquake epicenter.

XC = Ouptut vertical acceleration in cm/sec^2, positive down.

T = Input time of desired response.

Each call of SFVERT initiates the following sequence of operations:

1. The vector pointing from the source to the receiver is rotated from the global coordinate system to a source system.
2. Radiation pattern is computed and a motion vector and far-field time history is obtained.
3. The motion vector is rotated back to the global coordinate system.
4. The free surface correction is computed.
5. The result is convolved with the far-field time history.

Steps (2) through (5) are repeated for P, SV and SH motion. The total source model consists of three individual sources, and all steps are repeated for each individual source.

The routines performing the tasks are:

SFVERT - Master routine, contains source data, generates far-field time histories, applies free surface correction.

SFVERI - Performs coordinate transformations, computes radiation patterns.

FSURF - Computes P and SV free surface correction.

ROTATE - Performs vector rotations.

FSMOO - Smoothing routine.

DETER - Assists in computation of time histories.

The time histories, before the free surface correction is applied, consist of a series of steps in acceleration. They will, in theory, have zero area and double area proportional to seismic moment. In practice, these conditions are not met exactly due to discretization. The noncasual free surface correction also affects the areas in practice.

The source parameters for each crack are specified in a DATA statement in the master routine SFVERT. The individual parameters are as follows:

STRI = Fault strike (degrees).

DIPS = Fault dip (degrees).

SLIPS = Slip angle (degrees).

XS,YS = Cartesian coordinates of the crack epicenter (km)

HS = Source depth (km).

LS = Crack radius (km).

GAMS = See Boatwright's paramter $(\frac{\nu-1}{\nu})^{1/2}$.

DOS = Slip velocity at crack center (cm/sec).

VS = Rupture velocity (km/sec).

TS = Origin time (sec).

Orientation angles defined in the usual way. See Aki and Richards (1980), Chapter 4.

7.6 COMPARISON WITH NEAR-FIELD OBSERVATIONS

In this section we compare the near-field response predicted by the procedures described above with the observed ground motion at Pacoima Dam. The accelerometer at Pacoima Dam is one of over 90 strong motion instruments which triggered during the San Fernando earthquake. It was located only a few kilometers from the rupture surface and at an epicentral distance of about 8 to 14 kilometers, depending on the reference cited (Figure 41). The next nearest recording of the ground motion was located more than 20 kilometers from the epicenter. The motion recorded at Pacoima Dam has been quite controversial. When recorded in 1971, the horizontal accelerations recorded were the largest known to date. The instrument was located on the side of a ridge, and it was one of the first instances where topographic effects were considered as important to the motion recorded. After the event, the instrument was found to be tilted from its preearthquake position (Trifunac and Hudson, 1973). Though debate still occurs as to the credibility of the high frequencies recorded (empirical studies of ground acceleration often ignore the recording), the intermediate frequency content appears reasonable.

For simulation of acoustic radiation, the vertical ground acceleration is needed. The resulting pressure signatures in the linear part of the atmosphere most resemble vertical ground velocity in frequency content. Though the algorithm described in previous sections does generate ground acceleration, the acceleration produced is intended to be reasonable only in the intermediate frequency range (.5 to 3 Hz) which dominates ground velocity (and atmospheric pressures). For this reason the fairest test of our methods is a comparison of the recorded ground velocities at Pacoima Dam, and velocity obtained through integration of the output predicted by our algorithm.

Figure 42 shows the ground velocity at Pacoima Dam with that simulated with our procedures. Given the simplicity of our source and propagation models, the comparison is quite favorable, and most

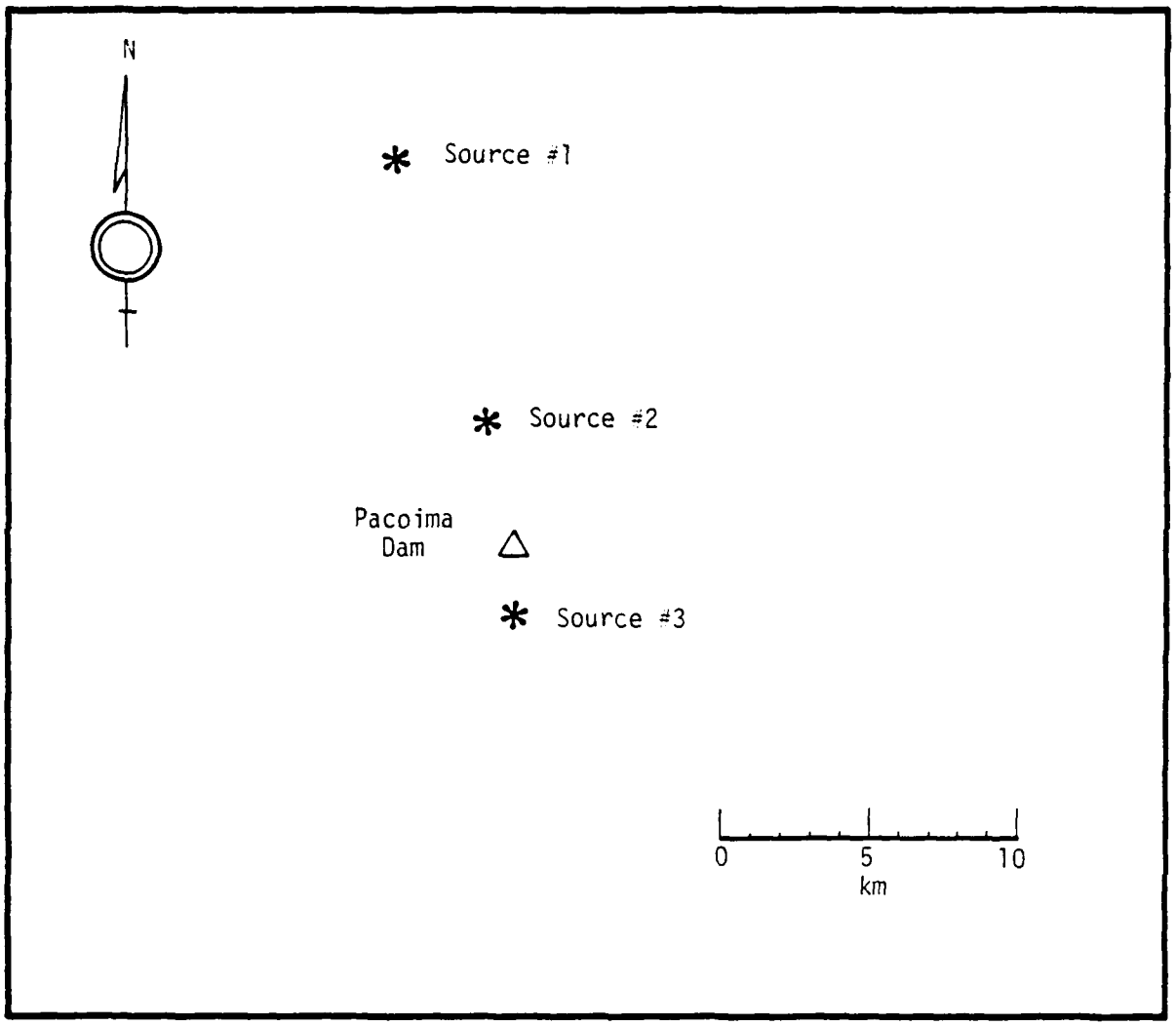

Figure 41. *Location of Pacoima Dam accelerograph site with the epicenters of the three discrete sources.*

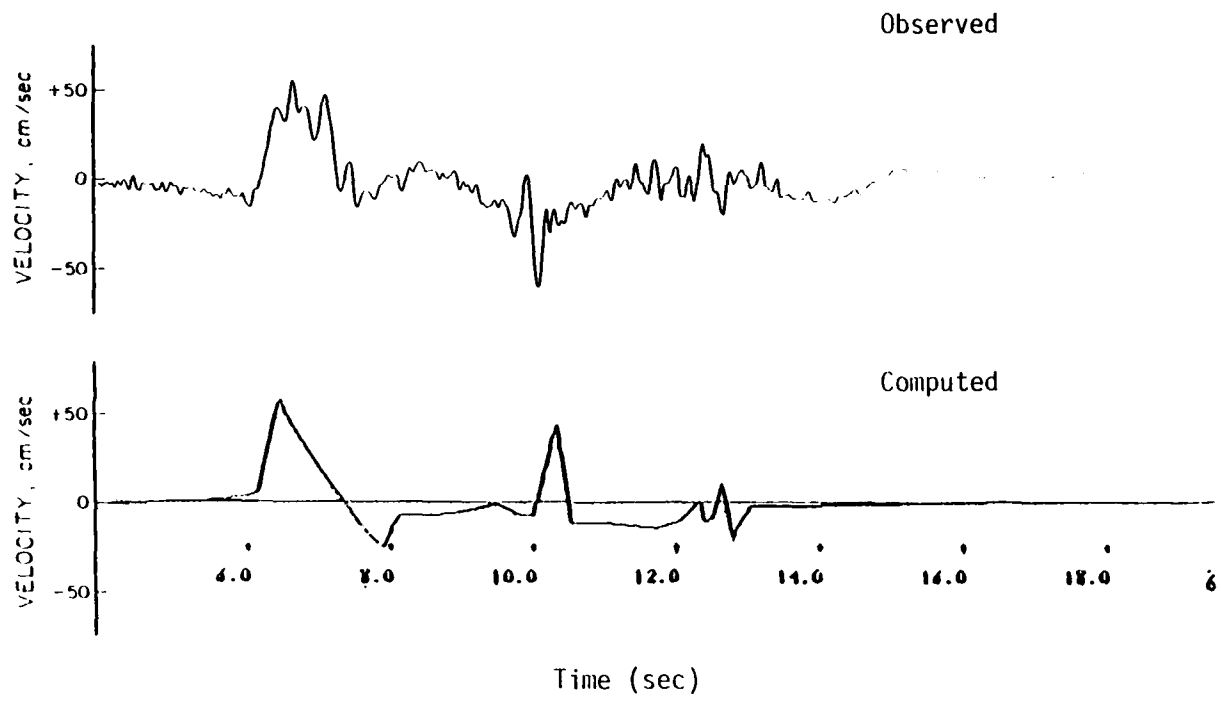

Figure 42. Comparison of observed and computed vertical ground velocities at Pacoima Dam.

previous attempts to model the ground velocity are not much more effective. The major deficiency concerns the response due to the second source of radiation. Our simulation contains approximately the proper amount of energy, but appears to be phase shifted by about 90 degrees. Past modeling efforts have not had success at dealing with this arrival either (see Boore and Zoback, 1974, and Bache and Barker, 1978). Our methods have some restrictions which may be responsible for the discrepancy. Other models of the source of radiation located above the kink of the fault have suggested that the rupture may have been unilateral. Our source model is limited to bidirectional rupture. The incident geometrical arrivals at Pacoima Dam from the source in question is very near the critical angle for incident S-waves. The poor performance of the first surface correction used here near critical incident angles may also contribute to the poor fit.

In summary, we have presented a simple algorithm for the simulation of the near-field ground accelerations from the 1971 San Fernando earthquake which shows reasonable agreement with observed ground motion in the intermediate frequency band. Our intent was not to develop a better model of the earthquake, but to use the results of previous studies and to apply a few carefully chosen approximations to develop an inexpensive tool for providing approximate near-field ground accelerations which can be used for the simulation of the atmospheric disturbances expected for a moderate sized earthquake.

REFERENCES

Aki, K., and P. G. Richards (1980), Quantitative Seismology: Theory and Methods, W. H. Freeman and Company, San Francisco.

Alewine, R. W., III, (1974), "Application of Linear Inversion Theory Toward the Estimation of Seismic Source Parameters," PH.D Thesis, California Institute of Technology.

Alsop, L. E., A. S. Goodman and S. Gregersen (1974), "Reflection and Transmission of Inhomogeneous Waves with Particular Application to Rayleigh Waves," BSSA, 64, pp. 1635-1652.

Anderson, J. G. (1974), "Motions Near a Shallow Rupturing Fault: Evaluation of Effects Due to the Free Surface," Geophys. J., 46, pp. 575-593.

Andrews, D. J. (1976), "Rupture Propagation with Finite Stress in Antiplane Strain," JGR, 81, pp. 3575-3582.

Antonova, L. V., F. F. Antikayev (1978), "Experimental Seismic Studies of the Earth's Interior," Moscow, 1978, Translated from the Russian by Joint Publications Research Service, JPRS L/8237, January 1979.

Apsel, R. J. (1979), "Dynamic Green's Functions for Layered Media and Applications to Boundary-Value Problems," Ph.D Thesis, University of California at San Diego, 380 pages.

Bache, T. C., H. J. Swanger and B. Shkoller (1980), "Synthesis of Lg in Eastern United States Crustal Models," Systems, Science and Software Semi-Annual Technical Report SSS-R-81-4668, September.

Bache, T. C. and T. G. Barker (1978), "The San Fernando Earthquake - A Model Consistent with Near-Field and Far-Field Observations at Long and Short Periods," Systems, Science and Software Final Technical Report submitted to the U.S. Geological survey, SSS-R-79-3552, January.

Boatwright, J. (1980), "A Spectral Theory for Circular Seismic Sources; Simple Estimations of Source Dimension, Dynamic Stress-Drop and Radiated Seismic Energy," BSSA, 70, pp. 1-28.

Bollinger, G. A. (1973), "Seismicity of the Southeastern United States," BSSA, 63, pp. 1785-1808.

Bollinger, G. A. (1979), "Attenuation of the Lg Phase and the Determination of m_b on the Southeastern United States," BSSA, 69, pp. 45-63.

Boore, D. M. and M. D. Zoback (1974), "Two-Dimensional Kinematic Fault Modeling of the Pacoima Dam Strong-Motion Recordings of the February 9, 1971 San Fernando Earthquake," BSSA, 64, pp. 555-570.

Bouchon, M, (1978), "A Dynamic Source Model for the San Fernando Earthquake," BSSA, 68, pp. 1555-1576.

Cherry, J. T. (1977), "User's Manual for the TRES Code," Systems, Science and Software Report SSS-R-77-3128, May.

Cherry, J.T., E. J. Halda and K. G. Hamilton (1976), "A Deterministic Approach to the Prediction of Free Field Ground Motion and Response Spectra from Stick-Slip Earthquakes," Earthquake Engng. and struct. Dyn., 4, pp. 315-332.

Day, S. M. (1977), "Finite Element Analysis of Seismic Scattering Problems," Ph.D. Dissertation, University of California, San Diego.

Day, S. M. (1979), "Three-Dimensional Finite Difference Simulation of Fault Dynamics," Systems, Science and Software Final Report SSS-R-80-4295, December.

Day, S. M., H. E. Read, J. J. Swanger and K. J. Cheverton (1980), "Simulation of Local Site Response to Earthquakes," Systems, Science and Software Final Technical Report submitted to the U.S. Geological Survey, SSS-R-80-4539, June.

Earthquake Engineering Research Laboratory (EERL) (1973), "Strong Motion Earthquake Accelerograms," California Institute of Technology, EERL 73-51.

Gregersen, S. and L. E. Alsop (1974) "Amplitudes of Horizontally Refracted Love Waves," BSSA, 64, pp. 535-553.

Hanks, T. C. (1974), "The Faulting Mechanisms of the San Fernando Earthquake," JGR, 79, pp. 1215-1229.

Hanks, T. C. and H. Kanamori (1979), "A Moment Magnitude Scale," JGR, 84, pp. 2348-2350.

Heaton, T. H. and D. V. Helmberger (1977), "A Study of the Strong Ground Motion of the Borrego Mountain, California, Earthquake," BSSA, 67, pp. 315-330.

Herrmann, R. B. (1969), "The Structure of the Cincinnati Arch as Determined by Short Period Rayleigh Waves," BSSA, 59, pp. 399-407.

Herrmann, R. B. (1977), "Research Study of Earthquake Generated SH Wave in the Near-Field and New-Regional Field," Final Report, Contract DACW39-76-C-0058, Waterways Experiment Station, Vicksburg, Mississippi.

Ida, Y. (1972), "Cohesive Force Across the Tip of a Longitudinal Shear Crack and Griffith's Specific Surface Energy," JGR, 77, pp. 3796-3805.

Johnson, L. R. (1974), "Green's Function for Lamb's Problem," Geophys. J., 37, pp. 99-131.

Kjartansson, E. (1979), "Constant Q - Wave Propagation and Attenuation," JGR, 84, pp. 4737-4748.

Knopoff, L., R. W. Fredricks, A. F. Bangi and L. D. Porter (1957), "Surface Amplitudes of Reflected body Waves," Geophsyics, 22, pp. 842-847.

Knopoff, L., R. G. Mitchel, E. G. Kausel and F. Schwab (1979), "A Search for the Oceanic Lg Phase," Geophys. J., 56, pp. 211-218.

Kostrov, B. V. (1964), "Self-Similar Problems of Propagating Shear Cracks," J. Appl. Math. Mech., 28, pp. 1077-1087.

Madariaga, R. (1976), "Dynamics of an Expanding Circular Fault," BSSA, 66, pp. 639-666.

McEvilly, T. V. (1964), "Central United States Crust-Upper Mantle Structure from Love and Rayleigh Wave Phase Velocity Inversion," BSSA, 54, pp. 1997-2015.

Mitchell, B. J. (1980), "Frequency Dependence of Shear Wave Internal Friction in the Continental Crust of Eastern North America," JGR, 85, pp. 5212-5218.

Nuttli, O. W. (1973), "Seismic Wave Attenuation and Magnitude Relations for Eastern North America," JGR, 78, pp. 876-885.

Ruzaikin, A. I., I. L. Nersesov, V. I. Khalturin and P. Molnar (1977), "Propagation of Lg and Lateral Variations in Crustal Structure in Asia," JGR, 82, pp. 307-316.

Sato, T. and T. Hirasawa (1973), "Body Wave Spectra from Propagating Shear Cracks," J. Phys. Earth, 21, pp. 415-431.

Street, R. L. (1976), "Scaling Northeastern United States/Southeastern Canadian Earthquakes by Their Lg Waves," BSSA, 66, pp. 1525-1537.

Swanger, H. J. and D. M. Boore (1978a), "Simulation of Strong-Motion Displacements Using Surface-Wave Modal Superposition," BSSA, 68, pp. 907-922.

Trifunac, M. D. and D. E. Hudson (1973), "Analysis of Pacoima Dam Accelergoram," in San Fernando California, Earthquake of February 9, 1971, Vol. III., U. S. Department of Commerce.

APPENDIX A

RUPTURE MODEL FOR MULTI-MATERIALS VERSION OF 14TRES

APPENDIX A. RUPTURE MODEL FOR MULTI-MATERIALS VERSION OF I4TRES

This appendix describes the algorithm modifications required to incorporate the two-degree-of-freedom, slip-weakening rupture model (Day, 1979) into the I4TRES code. The notation basically follows that of the Advanced Computing Laboratory document ACL-80-035. Modifications are confined to the fault plane equations.

On the slip plane, we permit motion in the u component, and form u and u' by analogy with v and v':

```
ū(JNODE,KNODE,LSLIP) =
1/2[u⁺(JNODE,KNODE,LSLIP)+u⁻(JNODE,KNODE,LSLIP)]
u'(JNODE,KNODE,LSLIP) =
1/2[u+(JNODE,KNODE,LSLIP) -u⁻(JNODE,KNODE,LSLIP)],
```

with similar definitions for $\dot{\bar{u}}$, $\ddot{\bar{u}}$, $\dot{u}'$, and $\ddot{u}'$. Likewise, we form $\overline{HGACCX}$ and HGACCX' by analogy with $\overline{HGACC}$ and HGACC':

```
For JNODE = JSLMN..JSLMX (JSEGMN≤JSLMN,JSEGMX≥JSLMX)
(HGACCX = ) HGACC(JNODE,1) = ζx(JNODE)*ζy(KNODE)*.5*
    *{MINV(JNODE-1/2,KNODE-1/2,LNODE-1/2)*
       *[δz(LNODE-1/2)*TQX2(JNODE-1/2,KNODE-1/2,LNODE-1/2)+δz(LNODE-1/2)
       *TQX3(JNODE-1/2,KNODE-1/2,LNODE-1/2)]
    +MINV(JNODE+1/2,KNODE-1/2,LNODE-1/2)*
       *[-δz(LNODE-1/2)*TQX2(JNODE+1/2,KNODE-1/2,LNODE-1/2)+δz(LNODE-1/2)
       *TQX3(JNODE+1/2,KNODE-1/2,LNODE-1/2)]
    +MINV(JNODE-1/2,KNODE+1/2,LNODE-1/2)*
       *[δz(LNODE-1/2)*TQX2(JNODE-1/2,KNODE+1/2,LNODE-1/2)-δz(LNODE-1/2)
       *TQX3(JNODE-1/2,KNODE+1/2,LNODE-1/2)]
    +MINV(JNODE+1/2,kNODE+1/2,LNODE-1/2)*
       *[-δz(LNODE-1/2)*TQX2(JNODE+1/2,KNODE+1/2,LNODE-1/2)-δz(LNODE-1/2)
       *TQX3(JNODE+1/2,KNODE+1/2,LNODE-1/2)]
```

```
+MINV(JNODE-1/2,KNODE-1/2,LNODE+1/2)*[2*ζz(LNODE)*TQX1(JNODE-1/2, KNODE-1/2)
   -δz(LNODE+1/2)*TQX2(JNODE-1/2,KNODE-1/2,LNODE+1/2)-δz(LNODE+1/2)
   *TQX3(JNODE-1/2,KNODE-1/2,LNODE+1/2)]
+MINV(JNODE+1/2,KNODE-1/2,LNODE+1/2)*[-2*ζz(LNODE)*TQX1(JNODE+1/2,
KNODE-1/2)
   +δz(LNODE+1/2)*TQX2(JNODE+1/2,KNODE-1/2,LNODE+1/2)-δz(LNODE+1/2)
   *TQX3(JNODE+1/2,KNODE-1/2,LNODE+1/2)]
+MINV(JNODE-1/2,KNODE+1/2,LNODE+1/2)*[-2*ζz(LNODE)*TQX1(JNODE-1/2,
KNODE+1/2)
   -δz(LNODE+1/2)*TQX2(JNODE-1/2,KNODE+1/2,LNODE+1/2)+δz(LNODE+1/2)
   *TQX3(JNODE-1/2,KNODE+1/2,LNODE+1/2)]
+MINV(JNODE+1/2,KNODE+1/2,LNODE+1/2)*[2*ζz(LNODE)*TQX1(JNODE+1/2, KNODE+1/2)
   +δz(LNODE+1/2)*TQX2(JNODE+1/2,KNODE+1/2,LNODE+1/2)+δz(LNODE+1/2)
   *TQX3(JNODE+1/2,KNODE+1/2,LNODE+1/2)]}.
```

Similarly,

```
HGACCX'(JNODE) = ζx(JNODE)*ζy(KNODE) * .5*
   *{MINV(JNODE-1/2,KNODE-1/2,LNODE-1/2)*
      *[-δz(LNODE-1/2)*TQX2(JNODE-1/2,KNODE-1/2,LNODE-1/2)-δz(LNODE-1/2)
      *TQX3(JNODE-1/2,KNODE-1/2,LNODE-1/2)]
   +MINV(JNODE+1/2,KNODE-1/2,LNODE-1/2)*
      *[δz(LNODE-1/2)*TQX2(JNODE+1/2,KNODE-1/2,LNODE-1/2)-δz(LNODE-1/2)
      *TQX3(JNODE-1/2,KNODE-1/2,LNODE-1/2)]
   +MINV(JNODE-1/2,KNODE+1/2,LNODE-1/2)*
      *[-δz(LNODE-1/2)*TQX2(JNODE-1/2,KNODE+1/2,LNODE-1/2)+δz(LNODE-1/2)
      *TQX3(JNODE-1/2,KNODE+1/2,LNODE-1/2)]
   +MINV(JNODE+1/2,KNODE+1/2,LNODE-1/2)*
      *[δz(LNODE-1/2)*TQX2(JNODE+1/2,KNODE+1/2,LNODE-1/2)+δz(LNODE-1/2)
      *TQX3(JNODE+1/2,KNODE+1/2,LNODE-1/2)]
   +MINV(JNODE-1/2,KNODE-1/2,LNODE+1/2)*[2*ζz(LNODE)*TQXID(JNODE-1/2,
   KNODE-1/2)
      -δz(LNODE+1/2)*TQX2(JNODE-1/2,KNODE-1/2,LNODE+1/2)-δz(LNODE+1/2)
      *TQX3(JNODE-1/2,KNODE-1/2,LNODE+1/2)]
```

```
+MINV(JNODE+1/2,KNODE-1/2,LNODE+1/2)*[-2*ζz(LNODE)*TQXID(JNODE+1/2,
KNODE-1/2)
   +δz(LNODE+1/2)*TQX2(JNODE+1/2,KNODE-1/2,LNODE+1/2)-δz(LNODE+1/2)
   *TQX3(JNODE+1/2,KNODE-1/2,LNODE+1/2)]
+MINV(JNODE-1/2,KNODE+1/2,LNODE+1/2)*[-2*ζz(LNODE)*TQXID(JNODE-1/2,
KNODE+1/2)
   -δz(LNODE+1/2)*TQX2(JNODE-1/2,KNODE+1/2,LNODE+1/2)+δz(LNODE+1/2)
   *TQX3(JNODE-1/2,KNODE+1/2,LNODE+1/2)]
+MINV(JNODE+1/2,KNODE+1/2,LNODE+1/2)*[2*ζz(LNODE)*TQXID(JNODE+1/2,
KNODE+1/2)
   +δz(LNODE+1/2)*TQX2(JNODE+1/2,KNODE+1/2,LNODE+1/2)+δz(LNODE+1/2)
   *TQX3(JNODE+1/2,KNODE+1/2,LNODE+1/2)]}.
```

In the above, TQX1 and TQXID are defined by

```
TQX1(JCELL,KCELL) = ρ(JCELL,KCELL,LCELL)*βR(JCELL,KCELL,LCELL)
   *δz(LCELL)/[ζz(LCELL+1/2)*δx(KCELL)]*HG1(JCELL,1)
TQXID(JCELL,KCELL) = ρ(JCELL,KCELL,LCELL)*βR(JCELL,KCELL,LCELL)
   *δz(LCELL)/[ζz(LCELL-1/2)*δx(KCELL)]*HG1X'(JCELL),
```

with

```
HG1(JCELL,1) = -ü(JCELL-1/2,KCELL-1/2,LCELL-1/2)+ü(JCELL+1/2,KCELL-1/2,LCELL-1/2)
               +ü(JCELL-1/2,KCELL+1/2,LCELL-1/2)-ü(JCELL+1/2,KCELL+1/2,LCELL-1/2)
HG1X'(JCELL)= -u̇'(JCELL-1/2,KCELL-1/2,LCELL-1/2)+u̇'(JCELL+1/2,KCELL-1/2,LCELL-1/2)
              +u̇'(JCELL-1/2,KCELL+1/2,LCELL-1/2)-u̇(JCELL+1/2,KCELL+1/2,LCELL-1/2).
```

Off the slip plane, TQXID(JCELL,KCELL) = 0.

Next we form the <u>acceleration</u> terms XSTART and YSTART:

```
XSTART(JNODE) = 0.5*δz(LNODE-1/2)*ζy(KNODE)*{-MXINV(JNODE,KNODE-1/2,LNODE-1/2)
   *[σxx(JNODE+1/2,KNODE-1/2,LNODE-1/2)-σxx(JNODE-1/2,KNODE-1/2,LNODE-1/2)]
   -MXINV(JNODE,KNODE+1/2,LNODE-1/2)
```

$$*[\sigma_{xx}(JNODE+1/2,KNODE+1/2,LNODE-1/2)-\sigma_{xx}(JNODE-1/2,KNODE+1/2,LNODE-1/2)]\}$$

$$+.5*\delta z(LNODE+1/2,)*\zeta_y(KNODE)*\{MXINV(JNODE,KNODE-1/2,LNODE+1/2)$$

$$*[\sigma_{xx}(JNODE+1/2,KNODE-1/2,LNODE+1/2)-\sigma_{xx}(JNODE-1/2,KNODE-1/2,LNODE+1/2)]$$

$$+MXINV(JNODE,KNODE+1/2,LNODE+1/2)$$

$$*[\sigma_{xx}(JNODE+1/2,KNODE+1/2,LNODE+1/2)-\sigma_{xx}(JNODE-1/2,KNODE+1/2,LNODE+1/2)]\}$$

$$+.5*\delta z(LNODE-1/2)*\zeta_x(JNODE)*\{-MYINV(JNODE-1/2,LNODE-1/2)$$

$$*[\sigma_{xy}(JNODE-1/2,KNODE+1/2,LNODE-1/2)-\sigma_{xy}(JNODE-1/2,KNODE-1/2,LNODE-1/2)]$$

$$-MYINV(JNODE+1/2,LNODE-1/2)$$

$$*[\sigma_{xy}(JNODE+1/2),KNODE+1/2,LNODE-1/2)-\sigma_{xy}(JNODE+1/2,KNODE-1/2,LNODE-1/2)]\}$$

$$+.5*\delta z(LNODE+1/2)*\zeta_x(JNODE)*\{MYINV(JNODE-1/2,LNODE+1/2)$$

$$*[\sigma_{xy}(JNODE-1/2,KNODE+1/2,LNODE+1/2)-\sigma_{xy}(JNODE-1/2,KNODE-1/2,LNODE+1/2)]$$

$$+MYINV(JNODE+1/2,LNODE+1/2)$$

$$*[\sigma_{xy}(JNODE+1/2,KNODE+1/2,LNODE+1/2)-\sigma_{xy}(JNODE+1/2,KNODE-1/2,LNODE+1/2)]\}$$

$$+.5*\zeta_x(JNODE)*\zeta_y(KNODE)*\sum_{L=LNODE-1/2}^{LNODE+1/2}\sum_{K=KNODE-1/2}^{KNODE+1/2}\sum_{J=JNODE-1/2}^{JNODE+1/2}$$

$$[MINV(J,K,L)*(\sigma_{xz}(J,K,L)+\gamma_{xz}(JNODE))]$$

$$+HGACCX'(JNODE).$$

$$YSTART(JNODE) = .5*\delta z(LNODE-1/2)*\zeta_y(KNODE)*\{-MXINV(JNODE,KNODE-1/2,LNODE-1/2)$$

$$*[\sigma_{xy}(JNODE+1/2,KNODE-1/2,LNODE-1/2)-\sigma_{xy}(JNODE-1/2,KNODE-1/2,LNODE-1/2)]$$

$$-MXINV(JNODE,KNODE+1/2,LNODE-1/2)$$

$$*[\sigma_{xy}(JNODE+1/2,KNODE+1/2,LNODE-1/2)-\sigma_{xy}(JNODE-1/2,KNODE+1/2,LNODE-1/2)]\}$$

$$+.5*\delta z(LNODE+1/2)*\zeta_y(KNODE)*\{MXINV(JNODE,KNODE-1/2,LNODE+1/2)$$

$$*[\sigma_{xy}(JNODE+1/2,KNODE-1/2,LNODE+1/2)-\sigma_{xy}(JNODE-1/2,KNODE-1/2,LNODE+1/2)]$$

$$+MXINV(JNODE,KNODE+1/2,LNODE+1/2)$$

$$*[\sigma_{xy}(JNODE+1/2,KNODE+1/2,LNODE+1/2)-\sigma_{xy}(JNODE-1/2,KNODE+1/2,LNODE+1/2)]\}$$

$$+.5*\delta z(LNODE-1/2)*\zeta_x(JNODE)*\{-MYINV(JNODE-1/2,LNODE-1/2)$$

$$*[\sigma_{yy}(JNODE-1/2,KNODE+1/2,LNODE-1/2)-\sigma_{yy}(JNODE-1/2,KNODE-1/2,LNODE-1/2)]$$

$$-MYINV(JNODE+1/2,LNODE-1/2)$$

$$*[\sigma_{yy}(JNODE+1/2,KNODE+1/2,LNODE-1/2)-\sigma_{yy}(JNODE+1/2,KNODE-1/2,LNODE-1/2)]\}$$

$$+.5*\delta z(LNODE+1/2)*\zeta_x(JNODE)*\{MYINV(JNODE-1/2,LNODE+1/2)$$

$$*[\sigma_{yy}(JNODE-1/2,KNODE+1/2,LNODE+1/2)-\sigma_{yy}(JNODE-1/2,KNODE-1/2,LNODE+1/2)]$$

$$+MYINV(JNODE+1/2,LNODE+1/2)$$

$$*[\sigma_{yy}(JNODE+1/2,KNODE+1/2,LNODE+1/2)-\sigma_{yy}(JNODE+1/2,KNODE-1/2,LNODE+1/2)]$$

$$+.5*\zeta_x(JNODE)*\zeta_y(KNODE)*\sum_{L=LNODE-1/2}^{LNODE+1/2}\sum_{K=KNODE-1/2}^{KNODE+1/2}\sum_{J=JNODE-1/2}^{JNODE+1/2}$$

$$[MINV(J,K,L)*\left(\sigma_{yz}(J,K,L) + \gamma_{yz}(JNODE)\right)]$$

$$+HGACC'(JNODE),$$

in which γ_{yz} and γ_{xz} are components of shear prestress.

Finally, we form a quantity A at each slip plane node, defined by

$$A(JNODE) = .5*\zeta_x(JNODE)*\zeta_y(KNODE)*\sum_{L=LNODE-1/2}^{LNODE+1/2}\sum_{K=KNODE-1/2}^{KNODE+1/2}\sum_{J=JNODE-1/2}^{JNODE+1/2}[MINV(J,K,L)]$$

The following input parameters are required for the rupture model: SFRAC, SMAX, SMIN, RUPV, RCRIT.

Then, at each node on the slip surface, at time TTIME, we determine the nodal quantities, SIGXZS, SIGYZS, YZBFR, YZSTAR, ISL (omitting the subscripts "JNODE, KNODE") according to the following algorithm:

$$D = \min\left\{\frac{[(u')^2 + (v')^2]^{1/2}}{SFRAC}, 1.0\right\}$$

$$STRF = (1. - D)*SMAX + D*SMIN$$

$$R = \text{distance of node from focus}$$

$$\dot{s} = \begin{cases}[(\dot{u}')^2 + (\dot{v}')^2]^{1/2} & \text{if } [(\dot{u}')^2 + (\dot{v}')^2] > 0\\ (XSTART^2 + YSTART^2)^{1/2} & \text{if } [(\dot{u}')^2 + (\dot{v}')^2] = 0\end{cases}$$

$$GX = \begin{cases}\dot{u}'/\dot{s} & \text{if } [(\dot{u}')^2 + (\dot{v}')^2] > 0\\ XSTART/\dot{s} & \text{if } [(\dot{u}')^2 + (\dot{v}')^2] = 0\end{cases}$$

$$GY = \begin{cases} \dot{v}'/\dot{s} & \text{if } [(\dot{u}')^2 + (\dot{v}')^2] > 0 \\ YSTART/\dot{s} & \text{if } [(\dot{u}')^2 + (\dot{v}')^2] = 0 \end{cases}$$

$$TR = R/RUPV$$

$$YZBFR = (XSTART^2 + YSTART^2)^{1/2} \Big/ A$$

$$ISL = 1$$

If (TR . GT . TTIME . OR . R . GT . RCRIT) go to 10

$$F = \min[(TTIME-TR) \Big/ (10. * \delta t) \ , \quad 1.0]$$

$$STRF\ 2 = (1. - F)*YZBFR + F*SMIN$$

IF (STRF2. LT. STRF) STRF = STRF2

$$ISL = 2$$

10 continue

$$B = .5* \delta t*STRF*A$$

$$CX = \dot{u}' + \delta t*XSTART - GX*B$$

$$CY = \dot{v}' + \delta t*YSTART - GY*B$$

$$C = (CX^2 + CY^2)^{1/2}$$

$$CX = CX/C$$

$$CY = CY/C$$

If (C . GT . B) go to 20

$$YZSTAR = [(\dot{v}'/\delta t + YSTART)^2 + (\dot{u}'/\delta t + XSTART)^2]^{1/2} \Big/ A$$

$$ISL = -ISL$$

$$SIGXZS = (\dot{u}'/\delta t + XSTART)/A$$

$$SIGYZS = (\dot{v}'/\delta t + YSTART)/A$$

Go to 220

20 $YZSTAR = .5*STRF*[(GX + CX)^2 + (GY + CY)^2]^{1/2}$

$$SIGXZS = .5*STRF*(GX + CX)$$

$$SIGYZS = .5*STRF*(GY + CY)$$

220 continue

Finally, we form the mean and differential accelerations. The differential accelerations are determined by

$$\ddot{u}' = XSTART - A * SIGXZS$$

$$\ddot{v}' = YSTART - A * SIGYZS,$$

and the mean accelerations are determined by

$$(\ddot{\bar{u}}=)\ddot{u}(JNODE,1)= .5*\delta z(LNODE-1/2)*\zeta_y(KNODE)*\{MXINV(JNODE,KNODE-1/2,LNODE-1/2)$$
$$*[\sigma_{xx}(JNODE+1/2,KNODE-1/2,LNODE-1/2)-\sigma_{xx}(JNODE-1/2,KNODE-1/2,LNODE-1/2)]$$
$$+MXINV(JNODE,KNODE+1/2,LNODE-1/2)$$
$$*[\sigma_{xx}(JNODE+1/2,KNODE+1/2,LNODE-1/2)-\sigma_{xx}(JNODE-1/2,KNODE+1/2,LNODE-1/2]\}$$
$$+.5*\delta z(LNODE+1/2)*\zeta_y(KNODE)*\{MXINV(JNODE,KNODE-1/2,LNODE+1/2)$$
$$*[\sigma_{xx}(JNODE+1/2,KNODE-1/2,LNODE+1/2)-\sigma_{xx}(JNODE-1/2,KNODE-1/2,LNODE+1/2)]$$
$$+MXINV(JNODE,KNODE+1/2,LNODE+1/2)$$
$$*[\sigma_{xx}(JNODE+1/2,KNODE+1/2,LNODE+1/2)-\sigma_{xx}(JNODE-1/2,KNODE+1/2,LNODE+1/2)]\}$$
$$+.5*\delta y(LNODE-1/2)*\zeta_x(JNODE)*\{MYINV(JNODE-1/2,LNODE-1/2)$$
$$*[\sigma_{xy}(JNODE-1/2,KNODE+1/2,LNODE-1/2)-\sigma_{xy}(JNODE-1/2,KNODE-1/2,LNODE-1/2)]$$
$$+MYINV(JNODE+1/2,LNODE-1/2)$$
$$*[\sigma_{xy}(JNODE+1/2,KNODE+1/2,LNODE-1/2)-\sigma_{xy}(JNODE+1/2,KNODE-1/2,LNODE-1/2)]\}$$
$$+.5*\delta z(LNODE+1/2)*\zeta_x(JNODE)*\{MYINV(JNODE-1/2,LNODE+1/2)$$

$$*[\sigma_{xy}(JNODE-1/2,KNODE+1/2,LNODE+1/2)-\sigma_{xy}(JNODE-1/2,KNODE-1/2,LNODE+1/2)]$$
$$+MYINV(JNODE+1/2,LNODE+1/2)$$
$$*[\sigma_{xy}(JNODE+1/2,KNODE+1/2,LNODE+1/2)-\sigma_{xy}(JNODE+1/2,KNODE-1/2,LNODE+1/2)]\}$$
$$+.5\zeta_x(JNODE)*\zeta_y(KNODE)*\sum_{K=KNODE-1/2}^{KNODE+1/2}\sum_{J=JNODE-1/2}^{JNODE+1/2}$$
$$[MINV(J,K,LNODE+1/2)*\sigma_{xz}(J,K,LNODE+1/2)-MINV(J,K,LNODE-1/2)*\sigma_{xz}(J,K,LNODE-1/2)]$$
$$+.5*\zeta_x(JNODE)*\zeta_y(KNODE)*\left(SIGXZS(JNODE)-\gamma_{xz}(JNODE)\right)*\sum_{K=KNODE-1/2}^{KNODE+1/2}\sum_{J=JNODE-1/2}^{JNODE+1/2}[MINV(J,K,LNODE-1/2)-MINV(J,K,LNODE+1/2)]$$
$$+\overline{HGACCX}(JNODE,1),$$

$$(\ddot{\bar{v}}=)\ddot{v}(JNODE,2)=.5\delta z(LNODE-1/2)*\zeta_y(KNODE)*\{MXINV(JNODE,KNODE-1/2,LNODE-1/2)$$
$$*[\sigma_{xy}(JNODE+1/2,KNODE-1/2,LNODE-1/2)-\sigma_{xy}(JNODE-1/2,KNODE-1/2,LNODE-1/2)]$$
$$+MXINV(JNODE,KNODE+1/2,LNODE-1/2)$$
$$*[\sigma_{xy}(JNODE+1/2,KNODE+1/2,LNODE-1/2)-\sigma_{xy}(JNODE-1/2,KNODE+1/2,LNODE-1/2)]\}$$
$$+.5*\delta z(LNODE+1/2)*\zeta_y(KNODE)*\{MXINV(JNODE,KNODE-1/2,LNODE+1/2)$$
$$*[\sigma_{xy}(JNODE+1/2,KNODE-1/2,LNODE+1/2)-\sigma_{xy}(JNODE-1/2,KNODE-1/2,LNODE+1/2)]$$
$$+MXINV(JNODE,KNODE+1/2,LNODE+1/2)$$
$$*[\sigma_{xy}(JNODE+1/2,KNODE+1/2,LNODE+1/2)-\sigma_{xy}(JNODE-1/2,KNODE+1/2,LNODE+1/2)]\}$$
$$+.5*\delta z(LNODE-1/2)*\zeta_x(JNODE)*\{MYINV(JNODE-1/2,LNODE-1/2)$$
$$*[\sigma_{yy}(JNODE-1/2,KNODE+1/2,LNODE-1/2)-\sigma_{yy}(JNODE-1/2,KNODE-1/2,LNODE-1/2)]$$
$$+MYINV(JNODE+1/2,LNODE-1/2)$$
$$*[\sigma_{yy}(JNODE+1/2,KNODE+1/2,LNODE-1/2)-\sigma_{yy}(JNODE+1/2,KNODE-1/2,LNODE-1/2)]\}$$
$$+.5*\delta z(LNODE+1/2)*\zeta_x(JNODE)*\{MYINV(JNODE-1/2,LNODE+1/2)$$
$$*[\sigma_{yy}(JNODE-1/2,KNODE+1/2,LNODE+1/2)-\sigma_{yy}(JNODE-1/2,KNODE-1/2,LNODE+1/2)]$$
$$+MYINV(JNODE+1/2,LNODE+1/2)$$
$$*[\sigma_{yy}(JNODE+1/2,KNODE+1/2,LNODE+1/2)-\sigma_{yy}(JNODE+1/2,KNODE-1/2,LNODE+1/2)]\}$$
$$+.5*\zeta_x(JNODE)*\zeta_y(KNODE*\sum_{K=KNODE-1/2}^{KNODE+1/2}\sum_{J=JNODE-1/2}^{JNODE+1/2}$$

$$[MINV(J,K,LNODE+1/2)*\sigma_{yz}(J,K,LNODE+1/2)-MINV(J,K,LNODE-1/2)*\sigma_{yz}(J,K,LNODE-1/2)]$$

$$+.5*\zeta_x(JNODE)*\zeta_y(KNODE)*\left(SIGYZS(JNODE) - \gamma_{yz}(JNODE)\right) *\sum_{K=KNODE-1/2}^{KNODE+1/2}$$

$$\sum_{J=JNODE-1/2}^{JNODE+1/2}$$

$$[MINV(J,K,LNODE-1/2)-MINV(J,K,LNODE+1/2)]$$
$$+\overline{HGACC}(JNODE,2).$$

APPENDIX B

14TRES TEST PROBLEMS

APPENDIX B
I4TRES TEST PROBLEMS

1. TEST PROBLEM I: BURIED DISLOCATION IN A UNIFORM ELASTIC HALFSPACE

In this problem, we treat a uniform halfspace excited by a one square kilometer fault, centered at a depth of five kilometers. The fault is vertical strike slip and the source time-function is shown in Figure 1. The P and S wave speeds (α and β) and density (ρ) of the halfspace are 6 km/sec, 3.46 km/sec, and 2.7 gm/cm^3, respectively. Free surface displacements computed by I4TRES can be compared to both Cagniard-deHoop and finite element solutions. The I4TRES input is given in Table B.1, and the grid configuration is sketched in Figure B.1.

2. TEST PROBLEM II: BURIED DISLOCATION IN A LAYERED ELASTIC HALFSPACE

The source in this problem is identical to that in Problem I. In this case, however, the uniform halfspace is overlain by two homogeneous layers, each of two kilometers thickness. The I4TRES input is given in Table B.2, the material properties are given in Table B.3, and the grid geometry is sketched in Figure B.2.

3. TEST PROBLEM III: SPONTANEOUS RUPTURE ON A PLANE

In this problem, rupture is forced to nucleate in a circular region of a fault plane. Subsequent rupture is controlled by a slip-weakening failure criterion (Ida, 1972; Andrews, 1976). In this model, a finite frictional strength σ_0 is assigned to the fault plane prior to initiation of sliding. Slip commences when necessary to prevent a stress concentration in excess of σ_0 from occurring. This relative displacement is assumed to weaken the fault plane, as in Figure B.3, until the total slip equals d_0, at

TABLE B.1

INPUT FOR I4TRES TEST PROBLEM I

Grid Limits

JMAXG = 60

KMAXG = 26

LMAXG = 51

JPLMN
JPLMX
KPLMN
KPLMX
LPLMN
LPLMX
} no plastic zones

JSLMN = 6

JSLMX = 6

KSLMN = 1

KSLMX = 1

LSLIP = 26

Zone Sizes

$\Delta x = \Delta y = \Delta z = 1000$ in the region of "uniform zoning", i.e., $j = 1 - 60$, $K = 1 - 16$, $L = 11 - 41$. Outside this region, the zone size increases at 15 percent per zone moving away from the uniform region.

Time Stepping

$\Delta t = 0.08$

Total time steps = 100

TABLE B.1 (CONTINUED)

Material Properties

Damping factor	BETA	=	0.2
Rotational Q factor	BETAR	=	1000
Yield stress	YIELD	=	10^{12}
Bulk modulus	AK	=	5.4×10^{10}
Shear modulus	AM	=	3.24×10^{10}
Density	RHO	=	2700

Source

Prestress	STLD	=	10^8
Sliding friction	SKIN	=	0.9×10^8
Rupture velocity	RUPV	=	10^8
Hypocentral node	JFOCUS	=	6
	KFOCUS	=	1

Boundary Conditions

J = 1	u, v, w all free
K = 1	u, w fixed, v free
L = 1, L = 51, J = 60, K = 26	u, v, w all fixed

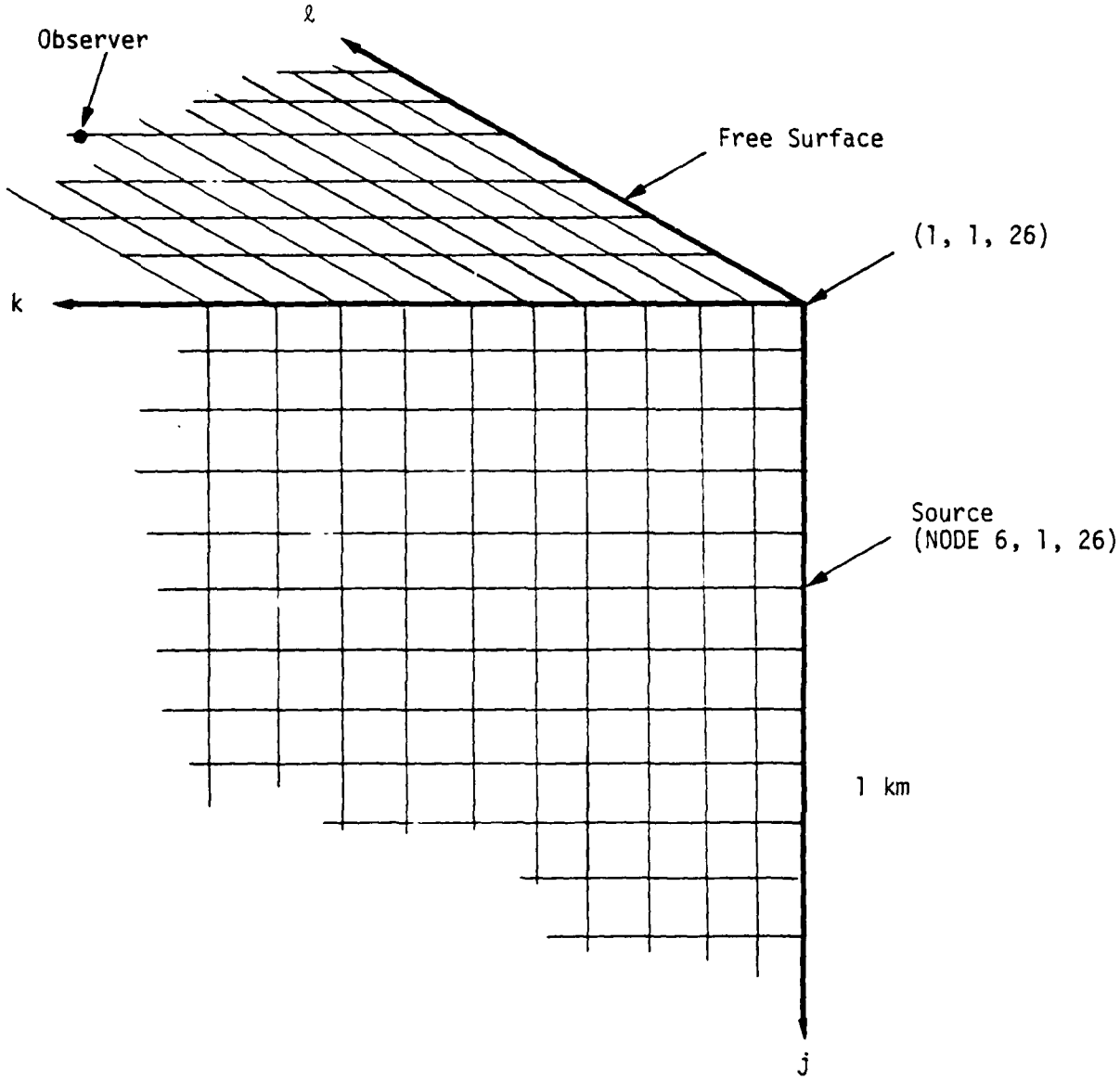

Figure B.1. Sketch of the ℓ = 26 plane for Test Problem I.

TABLE B.2

INPUT FOR I4TRES TEST PROBLEM II.

Grid Limits

JMAXG = 60

KMAXG = 30

LMAXG = 59

JPLMN
JPLMX
KPLMN
KPLMX
LPLMN
LPLMX
} no plastic zones

JSLMN = 6

JSLMX = 6

KSLMN = 1

KSLMX = 1

LSLIP = 30

Zone Sizes

$\Delta x = \Delta y = \Delta z = 1000$ in the region of "uniform zoning," i.e., $j = 1 - 60$, $k = 1 - 16$, $L - 15 - 45$. Outside this region, the zone size increases at 15 percent per zone moving away from the uniform region.

Time Stepping

$\Delta t = 0.08$

Total time steps = 150

TABLE B.2 (CONTINUED)

Materials

Three different materials. For each material, the damping factors and YIELD will be BETA = 0.2, BETAR = 1000, YIELD = 10^{12}. AK, AMU and ARHO are given in Table B.3.

Source

STLD = 10^8

SKIN = 0.9×10^8

RUPV = 10^8

JFOCUS = 6

KFOCUS = 1

Boundary Conditions

On J = 1	u, v, w all free
On K = 1	u, w fixed, v free
On L = 1, L = 59, J = 60, K = 30	u, v, w all fixed

Output

Saved variables are u, v, w, UD, VD, WD, VSL, VDSL.

Nodes at which output is required:

(1, 1, ℓ), ℓ = 30 to 45

(1, k, 30), k = 1 to 16

(1, k, 29 + k), k = 1 to 16

(1, 5, 40)

(1, 7, 44)

$$(6 = j,\ k,\ 30 + \ell) \begin{cases} j = -1 \text{ to } 1 \\ k = 1 \text{ to } 2 \\ \ell = -1 \text{ to } 1 \end{cases}$$

TABLE B.3

LAYER PROPERTIES FOR I4TRES TEST PROBLEM II

Layer	J Limits	K Limits	L Limits	Shear Modulus (AMU)	Bulk Modulus (AK)	Density (ARHO)
1	1 - 3	1 - 30	1 - 59	5.0×10^{9}	8.36×10^{9}	1670
2	3 - 5	1 - 30	1 - 59	1.9×10^{10}	3.17×10^{10}	2280
3	5 - 60	1 - 30	1 - 59	3.09×10^{10}	5.16×10^{10}	2580

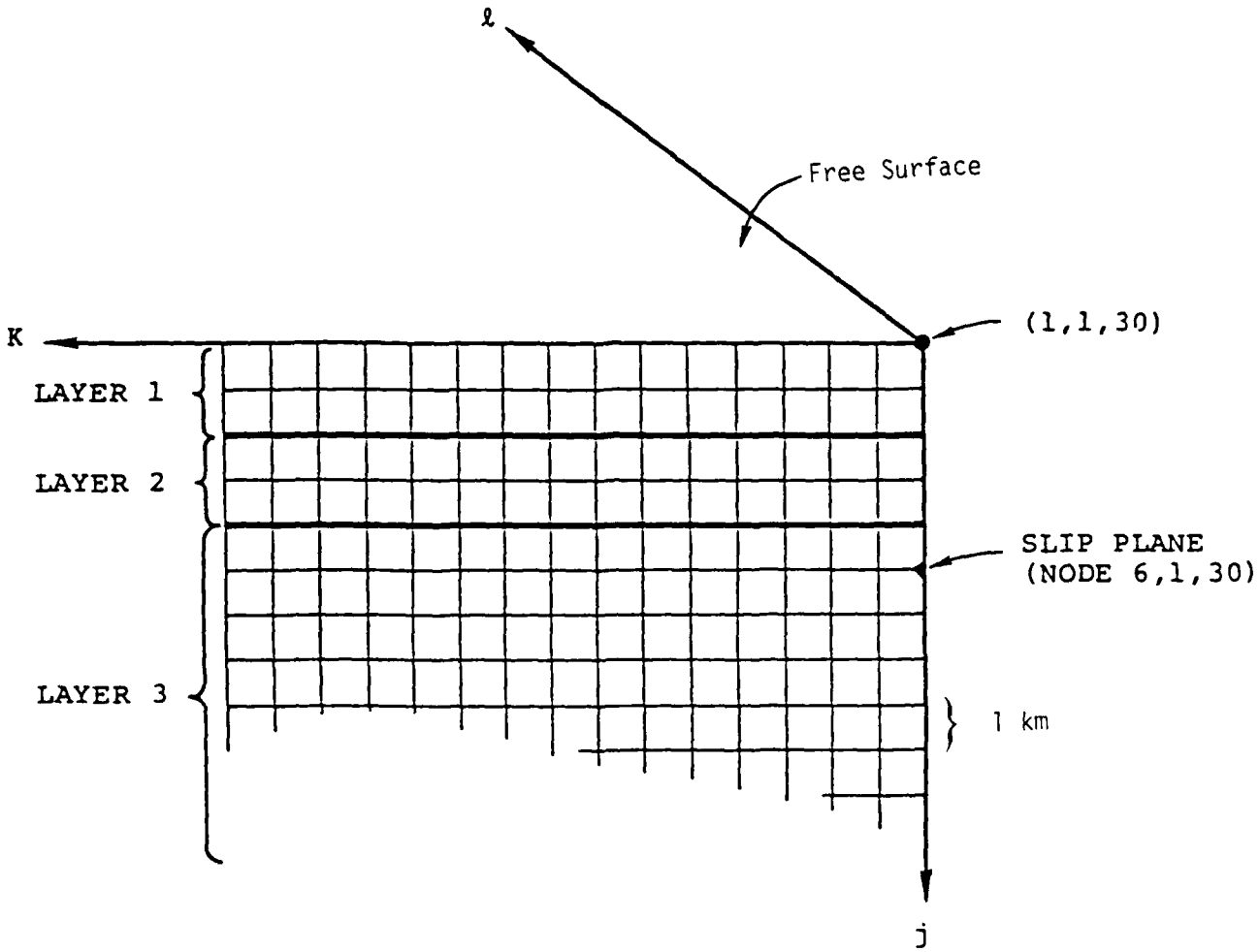

Figure B.2. Sketch of the ℓ = 30 plane for Test Problem II.

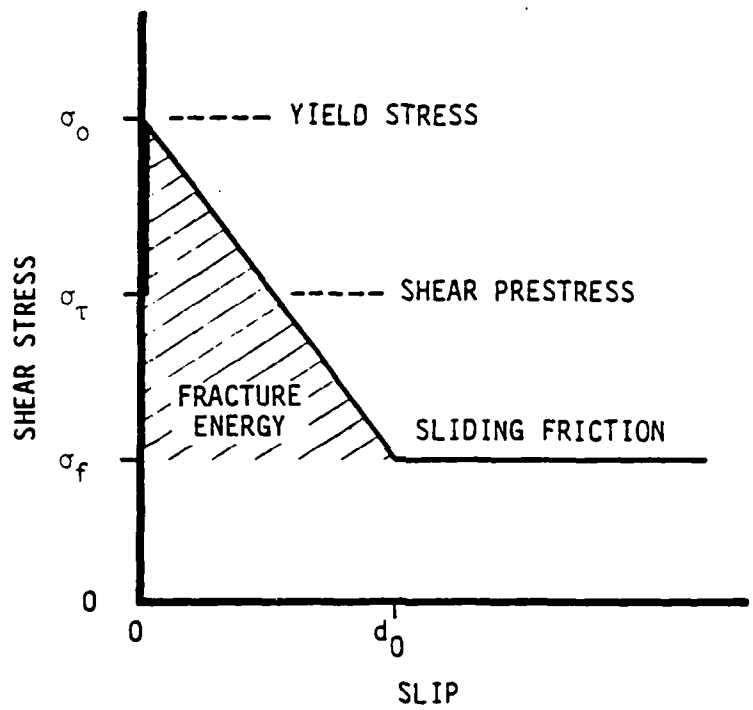

Figure B.3. Slip-weakening failure model (from Andrews, 1976)

which state the fault has lost all cohesion and reaches the kinetic friction level, σ_f.

Table B.4 gives the I4TRES input for this problem. The medium is uniform and there is no free surface. Test problem results can be compared to the numerical solution obtained with the single-material version of I4TRES. These results are reported by Day (1979, Figures 3.13 and 3.14).

4. TEST PROBLEM IV: BURIED THRUST FAULT

In this test case, rupture is confined to a small, buried surface to which a free surface is inclined at 45 degrees. The medium is a uniform, elastic halfspace. The I4tres input is given in Table B.5. Figure B.4 shows the configuration of the inclined free surface.

TABLE B.4

INPUT FOR I4TRES TEST PROBLEM III

Grid Limits

JMAXG = 20

KMAXG = 20

LMAXG = 41

JPLMN
JPLMX
KPLMN
KPLMX
LPLMN
LPLMX

no plastic zones

JSLMN = 1

JSLMX = 10

KSLMN = 1

KSLMX = 10

KSLIP = 21

Zone Sizes

$\Delta x = \Delta y = \Delta z = 150$ in the region of uniform zoning, i.e., $j = 1 - 10$, $k = 1 - 10$, $\ell = 12 - 30$. Outside this region, the zone size increases at 15 percent per zone.

Time Stepping

$\Delta t = 0.0125$

Total time steps = 50

TABLE B.4 (CONTINUED)

Material Properties

BETA	=	0.4
BETAR	=	1500
YIELD	=	10^{12}
AK	=	5.4×10^{10}
AMU	=	3.24×10^{10}
RHO	=	2700

Source

Prestress	STLD	=	10^8
Sliding friction	SMIN	=	0.9×10^8
Strength (σ_o)	SMAX	=	1.02×10^8
Rupture velocity	RUPV	=	1732
Nucleation radius	RCRIT	=	525
1/2 d_o	SFRAC	=	.05
Hypocentral node	JFOCUS	=	1
	KFOCUS	=	1

Boundary Conditions

J = 1	u fixed; v, w free
K = 1	u, w fixed; v free
L = 1, L = 41, J = 20, K = 0	u, v, w all fixed

TABLE B.5

INPUT FOR I4TRES TEST PROBLEM IV

Grid Limits

JMAXG = 60

KMAXG = 39

LMAXG = 39

JPLMN
JPLMX
KPLMN
KPLMX
LPLMN
LPLMX

no plastic zones

JSLMN = 1

JSLMX = 1

KSLMN = 17

KSLMX = 17

LSLIP = 17

Zone Sizes

$\Delta x = \Delta y = \Delta z = 1000$ in the region of uniform zoning, i.e., $j = 1 - 60$, $k = 11 - 29$, $\ell = 11 - 29$. Outside this region, the zone size increases at 15 percent per zone.

Time Stepping

$\Delta t = 0.08$

Total time steps = 100

TABLE B.5 (CONTINUED)

Material Properties

BETA	=	0.2
BETAR	=	1000
YIELD	=	10^{12}
AK	=	5.4×10^{10}
AMU	=	3.24×10^{10}
RHO	=	2700

Source

STLD	=	10^{8}
SKIN	=	0.9×10^{8}
RUPV	=	10^{8}
JFOCUS	=	1
KFOCUS	=	17

Boundary Conditions

On J = 1	u fixed; v, w free
On J = 60, K = 1, K = 39, L = 1, L = 39	u, v, w all fixed

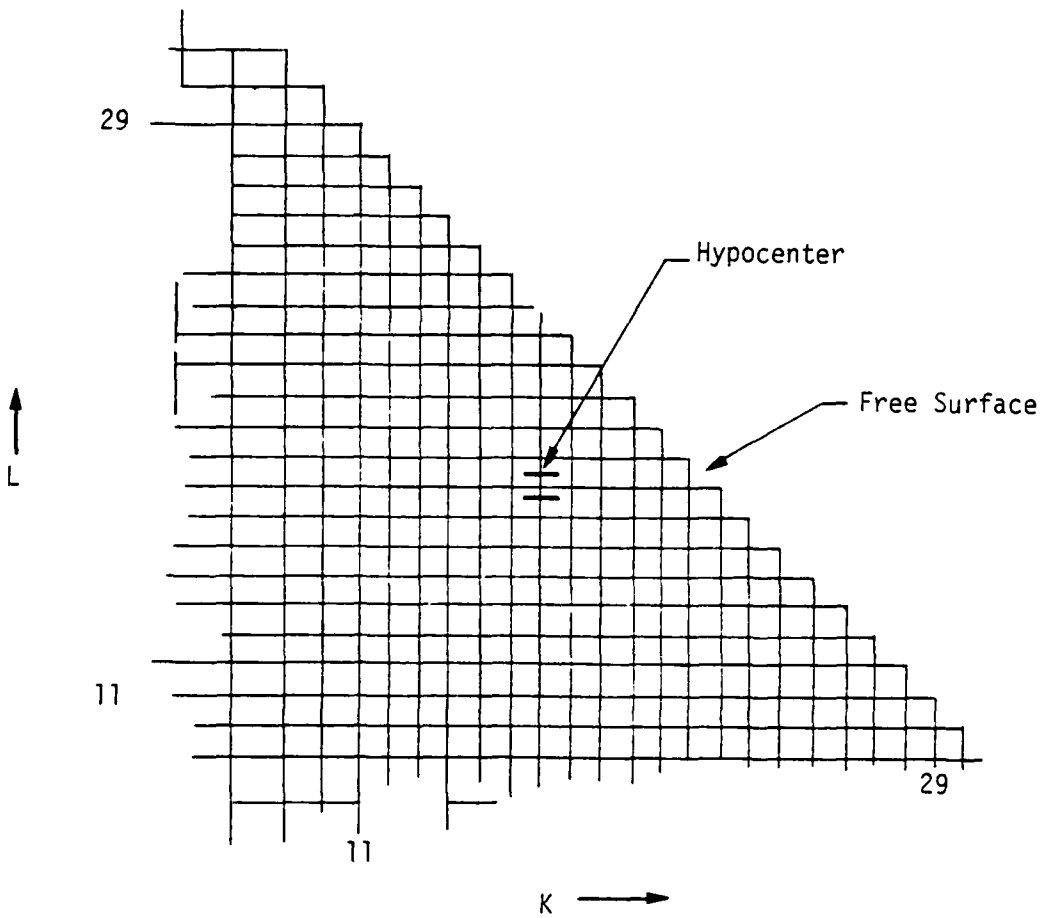

Figure B.4. A cross section of the grid for Test Problem IV, showing the free surface configuration.

APPENDIX C

CONVERSION OF THE TRES TO THE CRAY I, AND PARTIAL VECTORIZATION

APPENDIX C

CONVERSION OF TRES TO THE CRAY I, AND PARTIAL VECTORIZATION

In this appendix we record our experience in converting the TRES code from the UNIVAC 1100/81 computer to the CRAY I computer. This discussion is included in hopes of assisting other prospective CRAY users in estimating the effort involved in code conversion. We emphasize that only a partial vectorization was attempted in view of the available resources (i.e., 2.5 man-months).

We discuss first the initial work involved in getting a working code without vectorization. The original TRES code was written in UNIVAC FORTRAN V, which includes several nonstandard statements such as INCLUDE, DEFINE, RETURN 0, and some special I/O statements. The most time-consuming parts of the initial conversion process were conversion of input/output operations and replacement of INCLUDE statements.

We will start wtih the input/output operations which accounted for most of the difficulties in the conversion process. The standard FORTRAN read and write statements, although convenient to use, do not make efficient use of tapes and disks because the FORTRAN language does not permit parallel processing. Furthermore, a considerable amount of time is used in processing an I/O list because of its generality. To overcome those problems, the UNIVAC came out with nonstandard FORTRAN statements which allow buffering. The UNIVAC 1100/81 uses NTRAN I/O package which provides a tool for reading and/or writing binary information on tape or disk files. It also provides I/O buffering through a call statement in the FORTRAN language: Call NTRAN (UNIT, SEQUENCE OF OPERATION). NTRAN allows one to use 23 different types of operations, including positioning on the disk file. The hardware architecture of the UNIVAC computer put some restrictions on the FORTRAN I/O operations. It always reads and writes a multiple of 28 words. This "MAGIC" number is used to calculate the new position on the disk. We also have found

that the following somewhat unusual situation can occur and is allowed in NTRAN: one can write initially N records (N>1) on the disk, rewind the file, write K new records (K<N) and continue to read remaining records.

The CRAY-1 FORTRAN (CFT) also allows the programmer to use buffering operations, but its repertoire is very limited. Essentially, only five operations are allowed: BUFFER IN, BUFFER OUT, BACK SPACE, BACKFILE AND ENDFILE. To perform FORWARD SPACING, one has to use BUFFER IN instruction. Also, the READ AFTER WRITE combination is not allowed in CFT.

A second cumbersome problem was the replacement of INCLUDE statement, which is used to insert any externally defined set of UNIVAC FORTRAN statements into the program being compiled. The general form of the INCLUDE statement is INCLUDE, n, where n is the name of a procedure created by UNIVAC procedure definition processor (PDP). We had to replace all INCLUDE statements in each subroutine by set of PARAMETER, TYPE, and DIMENSION statements, etc. (Almost 500 cards had to be punched and inserted into the program file). While doing these replacements, we discovered that PARAMETER statement in the two compilers are slightly different. For example, PARAMETER N = 3 on the UNIVAC will have the form of PARAMETER (N = 3) on CRAY-1. Also, we had to change the DEFINE statements used in the PDP elements.

One also can expect some problems working with Hollerith and Alphanumeric data because of differences in the word length (64 bit word on CRAY versus 36 bit word on UNIVAC 1100/81)

Approximately two weeks of intensive effort by a programmer familiar with the CRAY-1 were required to obtain a diagnostic-free listing of the CRAY TRES code. Several more days were required to

identify and correct all potential divisions by zero, a circumstance tolerated by UNIVAC (result equals zero) and exploited in the original TRES code but not tolerated by the CRAY. Thus, the initial FORTRAN conversion phase required about three man-weeks.

Next we discuss the vectorization of the TRES program. We stress that our goal was to convert the existing code and not to fully optimize TRES, which would require rewriting most of the code and is considerally beyond the scope of this task. The first element in this process is to analyze the program to determine where it spends its time and to concentrate on those time-consuming parts. We have found that in our case almost all time was spent inside SUBROUTINE MOTION and some subprograms associated with it (ROTQ, PLSTRN, STRAIN). The original code is overly modular; most of the subroutines are inside the DO loops. We had to change this structure to put the DO loops inside the subroutines. This done, our efforts were directed to vectorization of MOTION, PLSTRN, etc. The partial vectorization was achieved by replacement of IF loops by DO loops, breaking of complicated loops to several short and simple ones, removal of the IF, CALL and some other similar statements from the DO-loops, changing the order of the nest loops, and so forth. The CFT diagnostic is very helpful in this matter, providing much of the needed information about scalar and vector loops.

This limited vectorization phase of the conversion task required an additional three man-weeks for completion. The remainder of the effort on the task was expended in testing and debugging.